The Dynamics of Solar Filament Channels

Jeff Smith

January 2017

Department of Physics

Prifysgol Aberystwyth University

Supervisor - Dr Xing Li

This thesis is submitted to Aberystwyth University for the degree of

Doctor of Philosophy.

DECLARATION

This work has not previously been accepted in substance for any degree and is not concurrently submitted in candidature for any degree.

Signed (candidate)

Date

STATEMENT 1

This thesis is the result of my own investigations, except where otherwise stated. Other sources are acknowledged by footnotes giving explicit references. Bibliographies are appended at the end of each chapter.

Signed (candidate)

Date

STATEMENT 2

I hereby give consent for my thesis, if accepted, to be available for photocopying and inter-library loan, and for the title and summary to be made available to outside organizations.

Signed (candidate)

Date

Summary

This research seeks to expand understanding of the processes which occur in solar filament channels by both modeling and observational methods.

Firstly, a cutting-edge area of Non-Linear Force Free modeling is significantly expanded to allow 3D multi-wavelength models with 45 second cadence; this allows prediction of rapid changes to the structures under study. Three-dimensional multi-wavelength models of a coronal loop system are created, allowing the estimation of some of the temperature distribution in the plasma. The free energy released in an eruption is also estimated.

In the following chapter, wave trains are observed in a solar filament, which I believe to be the first observations of their kind. These are interpreted as two very fast waves propagating across flux tubes in a solar filament, which in turn cause a succession of magneto-acoustic waves in different flux tubes. Following these exciting observations, the chapter attempts to explain the origin in terms of changes in the magnetic field.

Finally, counter-streaming motions are observed and discussed. The ubiquity of fast motions in Extreme Ultra-Violet wavelengths is shown. These are interpreted as waves rather than mass flows and it is thus postulated that many features in other filaments which could be interpreted as mass flows may in fact be waves. Through analysis of the magnetic field, observations of motions propagating in both directions from the same area and observations of the "reversal" of motions in the same flux rope, this chapter also offers possible explanations for the fascinating phenomenon of counter-streaming.

Acknowledgments - Diolch i chi gyd!

I don't think I could have presented this thesis without the help and support of so many people I've met along the way. Diolch i chi gyd - Thank you all so much. There follows a non-exhaustive list of acknowledgments and thanks.

Firstly, I'd like to thank my supervisor Dr Xing Li for his frequent meetings, advice, assistance and discussions. His door has always been open to me and I am grateful for his very practical support in what has been rather a roller-coaster of successes, failures, achievements and emotional turmoil.

Hoffwn diolch hefyd i Dr Huw Morgan, fy ail arolygydd, am ei gymorth, cefnogaeth ac amynedd. Er ei fod yn brysur iawn, mae fe wastad wedi bod yn barod i'm cynorthwyo ac i roi cyngor i mi am unrhyw beth. Diolchaf hefyd i Dr Eleri Pryse (Aberystwyth) ac i Dr Angharad Watkins (Coleg Cymraeg Cenedlaethol) am fy nghynorthwyo gyda'r papur a gyflwynais yng nghyfnodolyn Gwerddon.

I would like to thank my fellow PhD students for their company, assistance and guidance; student networks are very useful in studying for a PhD. I would also like to thank other staff members inside and outside the department for their support.

Hoffwn ddiolch i'm holl ffrindiau am eu cyfeillgarwch a chymorth, a'r holl amseroedd da dw i wedi bod yn digon ffodus i brofi dros y blynyddoedd diwethaf. Mae wedi bod yn pleser mawr, ac mae pawb wedi chwarae ei rhan yn fy nghadw yn fy iawnbwyll (wel, i rai raddau, haha!).

I'd like to also thank my family for their support, and I would also like to thank my doctor, my mentor, my counselor and my teddy bear for their help, medication, comfort and support in the frequently difficult times that have occurred in the course of my PhD writing.

This thesis couldn't have become reality without all the abundant help and support of everyone named above.

Diolch o galon am bopeth - Huge thanks for everything!

I'r rhai

na chaiff ddarllen

y traethawd hwn

xxx

Dechreu Can yngulch y tywyllwch

"Bydd miloedd y pryd hynny u'n rhyfeddy yn o'er ei naws

Wrth weled peth mor hynod yn dyfod ar ei traws,

Ar haul wen fydd yn duo ac Yno Ymguddio oi gwudd,

Daw r ser i apiro un hollol mor siriol yw ei fwydd."

Dafydd Watkin, 1748

[Extract from a poem describing an early observation of an eclipse, which underlines the historical importance of solar observations and the long-standing fascination with the Sun and its behavior. It's worth noting from elsewhere in the manuscript that Watkin appears to have timed the eclipse very precisely as lasting for 3 hours and 9 minutes.]

Contents

List of Figures

List of Tables

List of animations

Animation 1: This animation shows the dynamics of the filament studied in the chapters on wave trains and counter-streaming. The animation is a time-lapse movie with cadence 12s in the 171Å wavelength and shows activity over a period of 20 minutes.

Animation 2: This animation focuses on one part of the filament and shows fast motions studied in the wave trains chapter by means of running ratio, in the 304Å wavelength.

Animation 3: This animation shows the dynamics of a set of coronal loops over the period of one hour, in the 171Å wavelength, over a period of one hour

All the listed animations are included in the accompanying DVD.

Chapter 1

Introduction

1.1 The Sun - an Overview

Of all the features of the universe, the Sun is one of the most important influences on our lives. The Sun provides the necessary conditions to enable life on Earth, provides food for us via photosynthesis, provides light for us to see and even makes us happy. As a result, it is not at all surprising that the Sun has been the subject of fascination, research and even worship throughout human history.

The Sun is a giant ball of plasma, an ionized gas, composed chiefly of several layers as shown in Figure 1.1, each with their own characteristics.

The core is the central section of the Sun, extending from the solar center to approximately 0.25 solar radii. The predominant activity of the core is the process of nuclear fusion, whereby hydrogen atoms fuse to form helium atoms; this produces a huge amount of energy. These reactions are enabled by the sheer mass of the Sun and the resultant heat, pressure and gravitational force. The solar center is estimated to have a temperature of approximately 15,000,000K, and a density of $150\text{g} \cdot \text{cm}^{-3}$. (NASA, 2015)

The radiation zone extends from approximately 0.25 solar radii to approximately 0.7 solar radii, and mainly conducts energy from the core by means of radiation, the most efficient method of energy conduction in a zone of such high density and temperature. Photons transfer energy from particle to particle from the core outwards until such energy leaves the radiation zone. The properties of matter in the radiation zone vary vastly with distance from the core: the temperature drops from approximately 15,000,000K adjacent to the core to approximately 1,500,000K at the end of the radiative zone, whilst the density decreases from

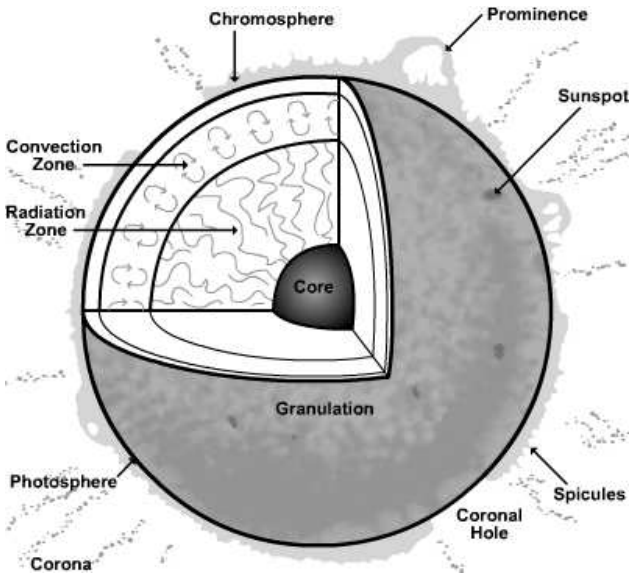

Figure 1.1: Solar layers, image from http://naturalfrequency.com/wiki/sun

$20\text{g} \cdot \text{cm}^{-3}$ to $0.2\text{g} \cdot \text{cm}^{-3}$ (NASA, 2015)

The method of energy conduction changes dramatically once the convection zone is reached. The temperature is below 2,000,000K, which reduces the efficiency of radiation as a method of energy conduction dramatically. As a result, energy is conducted through convection - a mechanism analogous to boiling. Once of the major features of this process is the motions created by the flows of convecting plasma. These motions manifest themselves at the solar surface in a pattern of granules and super-granules which can be seen as analogous to the exterior of a football (Stix, 1989), as shown in Figure 1.2.

It is also worth mentioning that the boundary layer between the radiation zone and the convection zone is known as the tachocline. This layer is responsible for producing the solar dynamo effect, which generates the Sun's magnetic field. The interface of the radiation zone and the conduction zone leads to shear flows which can affect the magnetic field lines dramatically (NASA, 2015).

The photosphere is the layer of the Sun that appears to be outermost when the Sun is viewed in visible light wavelengths (Stix, 1989). The innermost part of the photosphere is the point at which the Sun appears to become opaque from an external viewpoint. Estimates for the thickness of the photosphere vary, but Leroy & Rancoita (2015) cite it as 0.00014 solar radii, and the temperature varies from roughly 7,500K near the convection zone to approximately 4,500K near the next layer (the chromosphere) (Tennessee, 2010). The granulation pattern in the photosphere referred to previously and shown in Figure 1.2, is very distinctive. Each granule is usually in the order of 1000km in diameter and they have an estimated lifetime of approximately 20 minutes. (NASA, 2014)

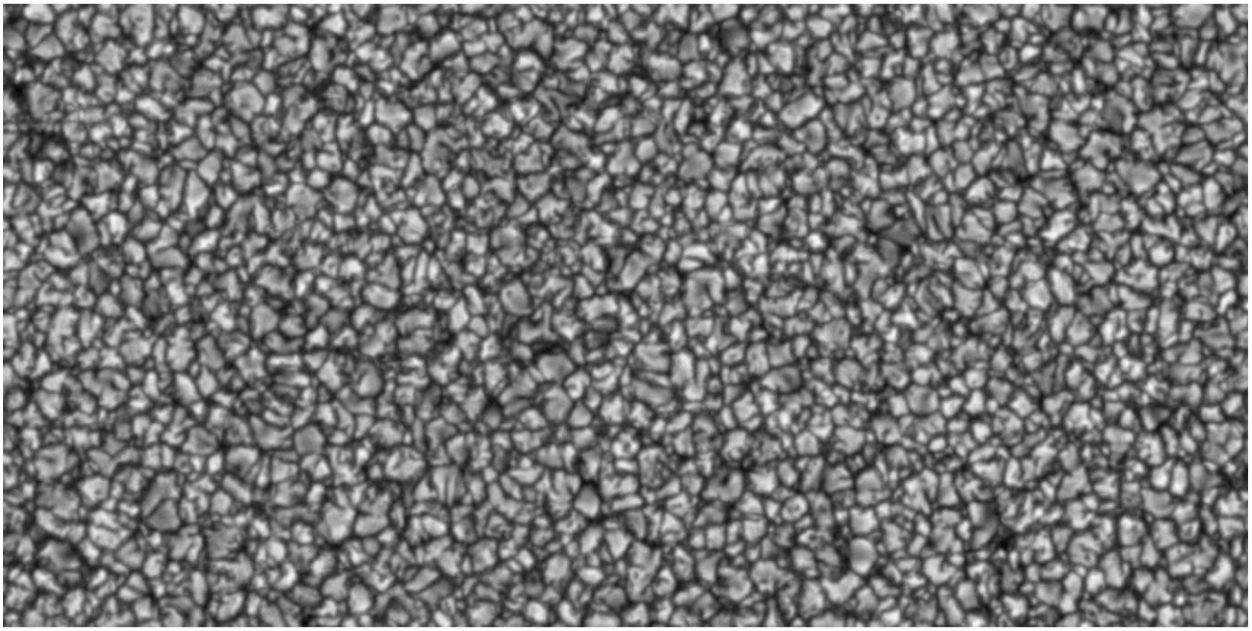

Figure 1.2: A typical granular pattern, from Muller et al. (2011)

The chromosphere is arguably the most interesting layer of the Sun from an astronomical viewpoint, due mainly to the rich variety of large-scale structures hosted by the chromosphere, which will be detailed later in this work, and also the relative clarity of observations, by means of H-α or CaII filters. The chromosphere is unusual in that the temperature rises from roughly 6,000K near the photosphere to roughly 20,000K near the corona. The temperature gradient in the chromosphere is fascinating - at first it decreases to approximately 4000K, then it rises rapidly until reaching the corona (UCAR, 2014). The chromosphere is approximately 2,000Km thick (Stix, 1989), and has a very low density: $10^{-7} - 10^{-14}$g cm^{-3} (Seeds et al., 2016).

The corona can be seen as the atmosphere of the Sun, and is a very active layer. The range of activity - including coronal loops, coronal mass ejections and, arguably, active regions, gives rise to a large variation in coronal temperatures, however usual coronal temperatures are in the order of 1,000,000K - 5,000,000K; more details can be found in Golub & Pasachoff (1997).

Observing the Sun is of course an age-old activity, with recorded observations since more than three millennia. However, human knowledge of the true nature of the Sun was very limited until telescopes were invented approximately 400 years ago. Since then, telescope technology has developed significantly.

There are still a large number of observations made of the Sun using ground-based telescopes, for instance in H-α wavelengths. However, ground-based observations have fundamental disadvantages: for instance the Earth's atmosphere, including clouds, can distort observations. Therefore it has been logical to attempt to establish telescopes in Space. Since the 1960s, technology has moved onwards, and the spatial and temporal

resolution, and amount of data collected by the instruments has increased, allowing closer and more complete observations of solar processes.

This research exclusively uses data from the Solar Dynamics Obseratory (SDO), detailed in the Instrumentation chapter, however two other space telescopes deserve a brief explanation: The Solar Optical Telescope (SOT) on the Hinode spacecraft provides detailed pictures of small areas of the Sun, however the inability to view the entire solar disk is a major disadvantage. The Hi-C mission was a pioneering mission which had produced data with 0.1 arcseconds to each pixel: hence the results were much more detailed than those of the SDO. It also had a temporal cadence of 5.5s, compared to 12s for AIA. However, the flight only lasted for 10 minutes, hence the data is very limited. However, the Hi-C mission led other authors to very fruitful results some of which have been used to aid the research in this thesis.

1.2 Solar Structures

Some of the most fascinating aspects of the Sun are the large structures that form on its surface. These include filaments/prominences, coronal loops and coronal holes. Many other interesting features can also be seen on the solar surface, some of them long-lived and some of them transient. These include spicules, solar flares, plages and coronal mass ejections. Several such features are described below.

1.2.1 Solar Filaments / Prominences

Solar filaments are large horizontal structures, consisting of a large amount of plasma levitated above the solar surface. The quantity of mass thus supported is difficult to determine, however Schwartz et al. (2015) found that the mass is frequently in the order of $10^{11} - 10^{12}$ Kg When viewed on the solar limb, solar filaments are described as solar prominences. An excellent overview is provided by Vial & Engvold (2015).

Structure of Filament - Prominence Systems

The macro-anatomy of a solar filament consists of a filament spine, which is the main body of the filament which runs laterally from one end to the other and is suspended some distance above the solar surface, and the barbs, vertical structures which connect the spine to the photosphere. The barbs can appear as somewhat similar to pillars, or like legs on a caterpillar. The points at which the barbs terminate is the subject of debate. The usual structure of a solar filament is shown in Figure 1.3

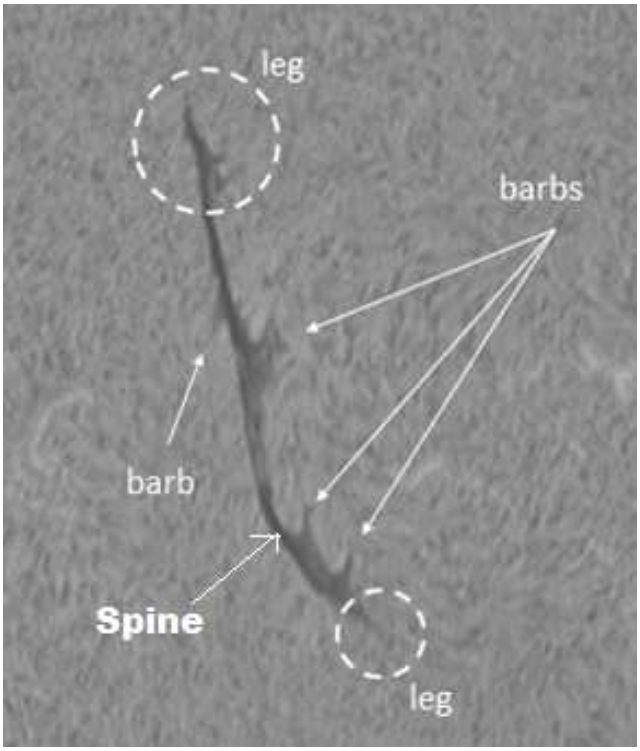

Figure 1.3: The anatomy of a typical solar filament. Image adapted from http://sidc.oma.be/news/219/welcome.html

Observations consistently suggest that a filament consists of many oscillating threads: the minimum observed width of such threads has been controversial and frequently happens to be about the same as the resolution of the instrument used to observe the prominence. Given this, it is widely believed that there may be a multitude of smaller threads that we cannot yet observe with the available technology. By way of examples, using observations from the Hi-C mission, Alexander et al. (2013) suggested that the fundamental width of filament threads may be 0.9 arcseconds, however using the Swedish Space Telescope (SST), Lin et al. (2005a) give the width of the finest threads observed as 0.14 arcseconds (though they cited the average width as 0.3 arcseconds), which as they note is very close to the resolution limit of the SST.

Lin et al. (2005a) observed that the threads generally constitute bundles, although there are lone threads observed. They also used the time slice technique, where the brightness along a certain line is combined into a distance-time plot through the use of multiple images, to obtain an estimated speed of movement of 2-3km s^{-1}. Plasma is observed to be flowing through some threads at velocities of 15 ± 10km s^{-1}, although they conclude that only a small number of threads carry plasma at any one time. Faster speeds have been observed, for instance Wang (1999) observed speeds of $10 - 70$km s^{-1} in a solar prominence, using Extreme Ultra-Violet observations in the 304Å wavelength.

Another suggestion made is that filament barbs may tend to be rooted in intergranular lanes. This idea was expanded by Lin et al. (2005b) in a study of many prominence barbs and their relation to the supergranular network. According to this study, 65% of prominence barbs end at the supergranular boundaries. This is an important discovery, since many had believed that prominence barbs were rooted in parasitic polarities (small areas where the polarity is opposite to the polarity of the surrounding area). A factor against the idea of barbs being rooted in parasitic polarities was the observation of counter-streaming, where a filament hosts flows in both directions. Lin et al. (2003) studied such a filament in H-alpha with the SST and discovered flows of about 8km s^{-1} in both directions. Counter-streaming (where material/energy travels in opposite directions along a filament) was also witnessed in the barbs. This clearly would not happen if the barbs were a consequence of reconnection between the prominence body and some polarity and were hence rooted in that polarity. Chae et al. (2005) confirm the counter-streaming with H-alpha observations from the Big Bear Observatory, and show barbs reaching towards the polarity inversion line (the dividing line between a region of positive magnetic flux and a region of negative magnetic flux) between two polarities, rather than to any particular polarity. A more detailed review of observations of counter-streaming is provided in the Counter-Streaming chapter.

The exact mechanism which provokes filament formation is not entirely clear, but it has frequently been proposed that filament formation is driven by cancellation between bipolar regions within the filament channel (Schmieder et al. (2004),van Ballegooijen & Martens (1989)).

Various studies (e.g. Arregui et al. (2012), Jing et al. (2003), Jing et al. (2006), Vršnak et al. (2007)) have investigated the oscillation of prominence threads, and the reasons for these. An interesting observation in prominences is the apparent presence of dark bubbles (particularly in H-alpha observations), sometimes plumes, which either stay static or appear to rise upwards. Although the means by which a darker (and therefore apparently cooler) bubble could support brighter (and therefore apparently hotter) material and not collapse was something of a mystery for some time. Berger et al. (2011) determined the temperature of one such bubble using a two-filter ratio technique, and found that the temperature of the bubble was at least 250,000K: significantly hotter than the surrounding prominence material. The authors suggest that at such a high temperature, the H-alpha and CaII lines are too ionized to produce a lot of emissions, explaining why these features appear to be dark in H-alpha. These authors also argue that such structures are eventually destroyed by Rayleigh-Taylor (RT) instabilities. Berger et al. (2010) observed with the HINODE telescope that dark turbulent upflows seem to originate from small-scale perturbations stemming from instabilities around the edge of the cavity (a seemingly dark area within the prominence). They observed the plumes rising with constant velocity, before arriving at equilibrium around 10-20Mm above the solar surface. They

also observed turbulence in the plumes during their ascent. Hillier et al. (2011a) noticed that some blobs of plasma are ejected from the top of prominences. They observed these blobs, 1000-2200km in width, being accelerated to Alfvénic velocities and then undergoing ballistic motion. They suggested that these effects may be a result of a tearing mode instability and/or a counterpart to descending knots. Knots are a recurring feature of prominence observations: they often appear as bright structures descending in prominences, though usually at speeds much less than freefall. Chae (2010) observed descending speeds of 10-30km s^{-1}, with small but varying acceleration. Knots are observed to get brighter as they accelerate, but only accelerate for a very short time. They suggest that this may be a result of magnetic reconnection with various field lines, though there are many unanswered questions.

Observations of the oscillations within threads have also been reported widely. For instance, Berger et al. (2008) studied many threads using the SOT, and found oscillation periods of 20-40 minutes and amplitudes of 2-5Mm. They compared the observed 10km s^{-1} speed of the oscillations with the 27km s^{-1} estimated Alfvén speed and concluded that the transverse waves may well be magnetoacoustic, rather than Alfvénic. Review papers by Labrosse et al. (2010) and Arregui et al. (2012) provide an abundance of additional information on solar filaments/prominences and their dynamics.

Modeling Filament-Prominence Systems

The first documented sighting of a prominence (to our knowledge), though not by that name, occurred during a solar eclipse in 1293AD. However, observation did not become common until 1868, when Janssen & Lockyer (Lockyer (1868),Janssen (1869),Janssen (1869a)), discovered that the spectral lines from prominences can be derived from earth-based telescope observations even without the aid of an eclipse. Modeling of prominences began with the Kippenhahn and Schlüter model in 1957 (Kippenhahn, 1957). This was the first model to balance gravitational and magnetic forces, producing dipped magnetic field lines. Although the model contained various simplifications: movement in one dimension only and a constant temperature throughout, the results tallied fairly well with observations of prominences. In the following years, various authors made modifications to the model to add more variables and more detail. For instance Anzer & Poland (1979) used a model that incorporated temperature variations and radiative transfer, through using known equations governing the behavior of H-alpha, concerning emissions occurring when hydrogen atoms change orbits. In the late 1970s models incorporated magnetostatic modeling (involving the magnetic field, plasma density and gravity) to invoke balancing between thermal conduction, radiative loss and wave heating, for instance Milne et al. (1979) who found that prominence structures cannot form when either the plasma beta (the ratio of the plasma pressure to the magnetic pressure) or the magnetic field shear (differential twisting of the magnetic

field lines) is too high. They speculated that this implies a minimum height for such structures and may also contribute to eruptions. Low (1982) created a model with multiple vertical threads hung by different magnetic fields and found that a high temperature can allow more mass to accumulate and a dip angle of $\frac{\pi}{4}$ to be optimal for mass collection. A major advance was made when Low & Petrie (2005) put a series of layers from Kippenhahn - Schlüter models on top of each other, each with their own temperatures, sag angles and dip positions. This model allows shearing without damage to the configuration. The model also gives better estimates of filament widths and lengths compared with observations. Another advantage of the Low and Petrie model over previous 1-dimensional (1D) is that it is 2-dimensional (2D). Although considering extra dimensions is computationally expensive, it is highly desirable since it enables a clearer understanding of prominences. 3D simulations have been understandably few, due to the scale of the computational task; however some authors have undertaken 3D simulations in an attempt to gain a fuller picture of filament dynamics. For instance, Demoulin et al. (1989) used a 3D model and also considered supergranulation in the Sun: they suggested that filament barbs and the lowest points of prominences are located at the center of supergranules, where the transverse field is weaker (assuming that the original Kippenhahn - Schlüter model is appropriate). They also investigated the effect of increasing the supply of flux to the prominence feet, and found that the feet of normal polarity filaments become wider as a result of a larger flux input. In order to account for some of the effects in three dimensions without the computational expense of a fully 3D model, some authors opt to use a 2.5D model, a basically 2D model extended to include inputs and outputs in the third dimension. A useful model was created by Xia et al. (2012), which claims to capture all phases of prominence formation. There are various theories on the structure of the magnetic field within prominence-filament structures. Since oscillating threads are frequently observed as the main component of filaments, it is hardly surprising that a popular model involves magnetic flux ropes, where the threads are modeled as tubes, which can all carry plasma. Hence the flux ropes correspond to the threads observed in filaments. Their behavior is determined by magnetohydrodynamic (MHD) equations, such as the model by Gibson & Fan (2006) which attempts to explain various effects such as coronal cavities through the use of a helical flux tube model held in place by an arcade of overarching ropes.

However, this is not the only possible form of support according to van Ballegooijen & Cranmer (2010), who suggest that tangled flux fields may create prominences, and support large amounts of plasma against gravity in the same way as a flux tube. In this model, large amounts of plasma can be trapped in various locations in the tangled magnetic field, and can be pushed upwards. They also suggest an explanation for vertical threads: they suggest that a vertical thread may exist in a dip where the speed of the movement of the plasma is subsonic, then at the next peak there is a sonic point; the speed of the plasma in the next

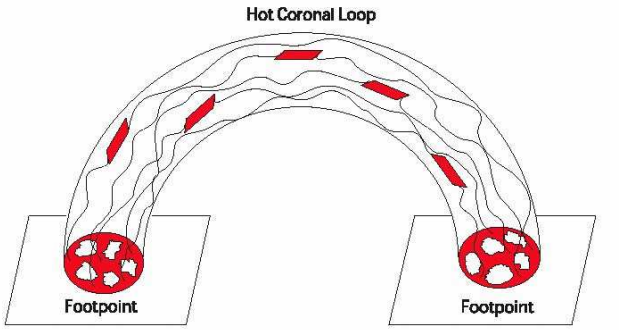

Figure 1.4: A schematic diagram of a hypothetical coronal loop. This was Figure 1 in Kittinaradorn et al. (2009).

dip is supersonic, then at the next peak there is a shock. The significance of this setup is that the shocks can disperse the gravitational potential energy, and hence prevent freefall. Another aspect of prominence modeling is the attempt to explain the bubbles and rising plumes which have been observed in prominences. One of the explanations given for the extraordinary buoyancy of such structures is of a twisted flux rope rising through the prominence, as hypothesized by Sakurai (1976). Hillier et al. (2011b) attempted to model the rising plumes being caused by a Rayleigh-Taylor instability (an instability where plasmas of different densities meet); although rising plumes similar to those observed with the SOT were produced by this simulation, the velocities of the plumes were in the order of double-quadruple the velocities observed with the SOT. However, some explanation may be found in a paper by Berger et al. (2008), where they found that the upflows seen with HINODE have a much greater velocity than those seen in various H-alpha observations.

1.2.2 Coronal Loops

Coronal loops are vast arch-like structures with their feet in two regions of opposite polarity; they can connect different active regions to each other. They are claimed to be rooted in areas of active region "moss", which is subsequently heated significantly by the coronal loops (Kittinaradorn et al., 2009). Coronal loops are filled with hot plasma, hence they appear as bright structures in EUV observations, both against the solar limb and on the solar disc. They can reach altitudes of 1000s of km (Durak et al., 2007), and can also form arcades (Reva et al. (2015),Jain et al. (2015),Kumar et al. (2015)). The dynamics and configurations of groups of coronal loops can be altered by nearby features, such as flares (Zimovets & Nakariakov, 2015), or filament eruptions (Kushwaha et al., 2015). The effects on the coronal loops can be substantial: oscillations (Zimovets & Nakariakov, 2015) or even magnetic reconnection leading to a reconfiguration of the coronal loops. This reconfiguration can lead to the release of free energy, for instance through flares (Pinto et al. (2016), Browning & Gordovskyy (2011)).

Coronal loops are believed to be composed of a series of threads (Tajfirouze et al. (2016), Schmelz et al. (2015)). These individual threads are likely to be tangled (Schmelz et al. (2015), Schmelz (2011),Kittinaradorn et al. (2009)) and can have different characteristics and in particular can have significantly different temperatures (Schmelz et al., 2015). It is believed that coronal loops are heated from the base, and Dahlburg et al. (2016) claim that only a small proportion of the coronal loop is undergoing heating at any particular time.

A schematic diagram of a coronal loop is provided in Figure 1.4. This is was Figure 1 in Kittinaradorn et al. (2009).

1.2.3 Some Other Common Solar Structures

Other structures observed on the solar surface include spicules, coronal holes and plages.

Spicules are narrow jet-like features which are proposed as a cause of coronal heating (Athay & Holzer (1982), Pneuman & Kopp (1978)) and perhaps of the solar wind (Pike & Harrison, 1997).They may be powered by magnetic reconnection (Cheung et al., 2015). The threads composing spicules are understood to be twisted such that the spicules are roughly helical (Tavabi et al., 2015).

Coronal holes are areas of the corona which appear in EUV observations as large dark areas on the solar disc, due to a lack of UV, EUV and x-ray emissions compared to their surroundings. They persist for long time periods and rotate rigidly over time (whereas the corona rotates differentially) (Krieger et al. (1973), Neupert & Pizzo (1974), Nolte et al. (1976), Hegde et al. (2012), Japaridze et al. (2015)). Their dark appearance does not preclude emission; on the contrary, many authors such as Tsurutani et al. (1995), Gosling & Pizzo (1999) and Cranmer (2009) hold that they emit many particles into space in streams, and this is held to be a major contributor to the solar wind.

Plages appear as bright regions on the solar disc and are areas where there is a very large unipolar polarity (Carlsson et al., 2015). The nature of these differs between the northern and southern hemispheres as a function of the solar cycle (Dorotovič et al., 2010).

1.3 Waves in Solar Filaments and Coronal Loops

1.3.1 MHD Theory

Magnetohydrodynamics, or MHD, is a field of study often used to describe plasmas such as those in the solar corona, for frequencies much less than the ion gyrofrequency. It considers the effect of electric fields on the flow of ions in the plasma. The flow of ions in the plasma in its turn alters the magnetic field. MHD models can contain many variables, but in its simplest form, ideal MHD is described by a set of equations which principally combine Maxwell's electromagnetic equations with the Navier-Stokes equations for fluids. Ideal MHD assumes that the plasma is non-resistant, that is the plasma has infinite conductivity. This can also be expressed by saying that the magnetic Reynolds number R_m is very large. The consequence of the frozen-in condition is that any particular parcel of plasma will move with the field lines.

Maxwell's equations as used for MHD purposes are composed of four differential equations:

- Gauss' Law:

  $\bigtriangledown \cdot \mathbf{E} = \frac{\rho_c}{\epsilon_0}$

  Where $\mathbf{E}$ is the electic field, ρ_c is the charge density and ϵ_0 is the permittivity of free space. This law states that the the electric field leaving a given volume is proportional to the charge inside the volume. MHD assumes charge neutrality, and as a result ρ_c is treated as 0.

- Gauss' law for magnetism:

  $\bigtriangledown \cdot \mathbf{B} = 0$

  Where $\mathbf{B}$ is the magnetic field. This law serves to discount any magnetic monopoles, and is sometimes explained as a flux equilibrium: the total of the magnetic flux through the closed boundary of a given volume is 0.

- Maxwell-Faraday equation

  $\bigtriangledown \times \mathbf{E} = -\frac{\partial \mathbf{B}}{\partial t}$

  Where t is time. This law states that if the magnetic field varies with time, the electric field varies spatially. The converse is also true.

- Ampere's Law (as amended by Maxwell)

  $\bigtriangledown \times \mathbf{B} = \mu_0 \mathbf{J}$

where μ_0 is the permeability of free space and $\mathbf{J}$ is the current density. In Ampere's law the displacement current is dropped since it is negligible.

For a simple electron-proton plasma (where the number densities of the electrons and protons are equal), The Navier-Stokes equations used for MHD purposes are as follows:

- Mass Continuity Equation

  $\frac{\partial \rho_m}{\partial t} + \bigtriangledown \cdot (\rho_m \mathbf{U}) = 0$

  Where ρ_m is the mass density and $\mathbf{U}$ is the fluid velocity. This can be described as an equation stating the conservation of mass in the context of a plasma.

- Momentum equation

  For MHD, this simplifies to:

  $\frac{\partial (\rho_m \mathbf{U})}{\partial t} + \bigtriangledown \cdot (\rho_m \mathbf{U}\mathbf{U}) = -\bigtriangledown \cdot P + \mathbf{J} \times \mathbf{B}$

  Where P is the plasma pressure tensor.

The equations for MHD can now be deduced.

- Mass Continuity Equation

  $\frac{\partial \rho_m}{\partial t} + \bigtriangledown \cdot (\rho_m \mathbf{U}) = 0$

  It is critical for this that the fluid velocity represents the mass-weighted average of the velocities of the individual charged particles.

- Momentum Equation

  $\rho_m [\frac{\partial \mathbf{U}}{\partial t} + \mathbf{U}(\bigtriangledown \cdot \mathbf{U})] = \mathbf{J} \times \mathbf{B} - \bigtriangledown \cdot P$

  or alternatively, using Ampere's Law:

  $\rho_m [\frac{\partial \mathbf{U}}{\partial t} + \mathbf{U}(\bigtriangledown \cdot \mathbf{U})] = \frac{1}{\mu_0}(\bigtriangledown \times \mathbf{B}) \times \mathbf{B} - \bigtriangledown \cdot P$

- Simplified Ohm's Law

  Simplified Ohm's law modifies Ohm's original law to include the effects of the electric and magnetic fields in a plasma, and also the movement of the plasma. The full equation would read as follows:

  $\mathbf{E} + \mathbf{U} \times \mathbf{B} = \eta \mathbf{J}$

  However, the term on the right hand side is often negligible. η is the resistivity of the plasma which is often assumed to be negligible. Hence the final equation is simpler:

$\mathbf{E} + \mathbf{U} \times \mathbf{B} = 0$

- Induction Equation

  Substituting the Maxwell-Faraday equation yields the induction equation:

  $frac\delta\mathbf{B}\delta t = \bigtriangledown \times (\mathbf{U} \times \mathbf{B}) + \nabla \bigtriangledown^2 \mathbf{B}$

MHD waves can be grouped into three main categories (although there are also sub-categories as discussed later):

- magneto-acoustic waves (also known as sound waves or acoustic waves) travel at the local sound speed, which in flux tubes varies greatly but can be in the order of 100km s^{-1}. The speed of sound waves in a flux tube will depend on various parameters, such as the local temperature, the density of plasma in the flux tube and the plasma pressure in the flux tube
- Alfvén waves travel at the Alfvén speed within the flux tube. Again, the Alfvén speed within a flux tube depends on a number of parameters. Three important characteristics of Alfvén waves is that they always follow the magnetic field, they are dispersionless and they do not produce density fluctuations in the surrounding atmosphere, thus making observation of Alfvén waves very difficult.
- Fast waves are generally faster than acoustic or Alfvén waves, though their precise speed depends mostly on the Alfvén speed. In the limiting case where the Alfvén speed (and hence the magnetic field) is very small, they become acoustic waves.

Depending on the parameters of the flux tube, the relationship between the slow, fast and Alfvén waves differs. Modeling has allowed researchers to investigate these relationships. Edwin & Roberts (1983) pioneered the modern modeling of waves in flux tubes, using a cylinder model. By calculating the dispersion relations inside and outside a slender cylinder, they succeeded in deriving relations between phase speed and wave-number for slow and fast sausage and kink waves. They found that, for the case where the interal Alfvén speed exceeds the external Alfvén speed, the hypothetical sausage mode increases monotonically, however the kink mode is not monotonic but has a defined minimum or maximum. A hypothetical situation is shown in Figure 1.5 (credit Edwin and Roberts).

For coronal conditions, the results are more interesting. Figure 1.6 (credit Edwin and Roberts) shows the relationship between phase-speed and wave-number for fast and slow sausage and kink waves in the solar corona. The magneto-acoustic waves shown on the graph are families of waves with a large number of potential speeds. The presence or absence of fast waves depends on whether $V_{ae}>V_a$. The implications of this, if the magnetic field strength and pressure are the same both within and outside the flux tube, is that

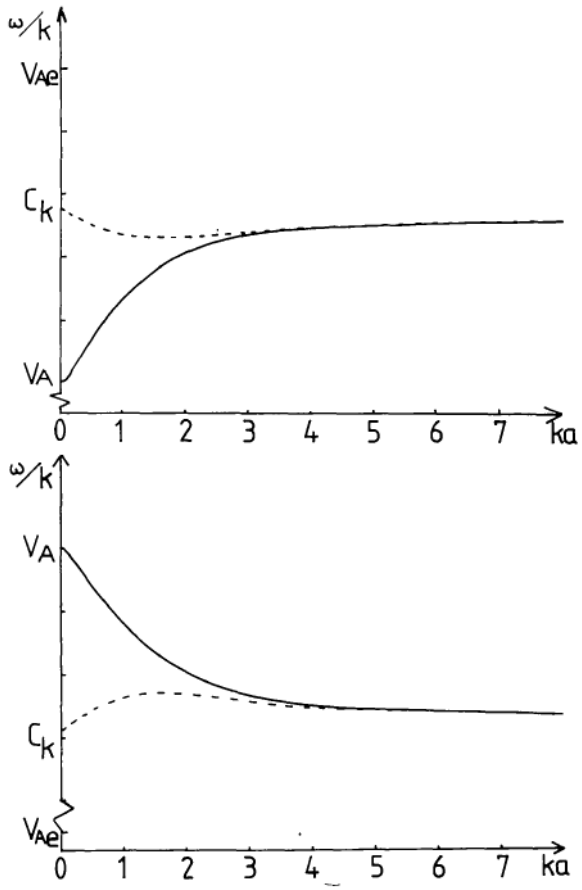

Figure 1.5: Hypothetical relation between phase speed and wave-number for kink and sausage waves. This is Figure 2 in Edwin and Roberts, 1983.

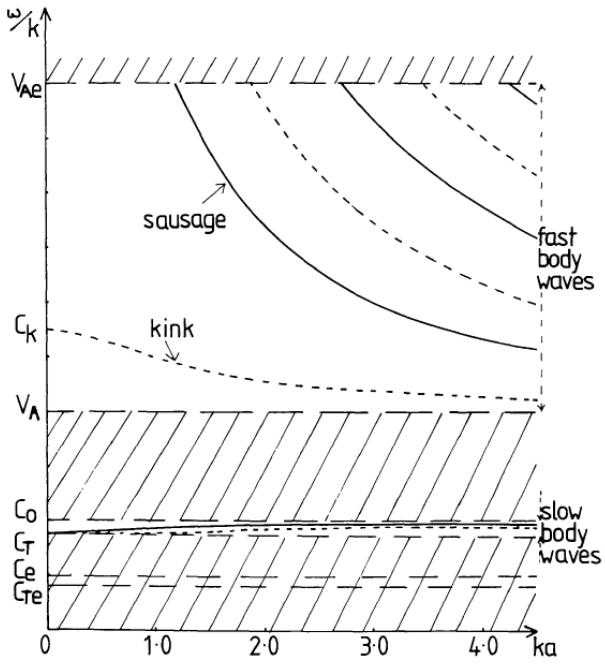

Figure 1.6: Graph of how phase speed (horizontal axis) varies with wave-number (vertical axis) for slow and fast kink modes in flux tubes in the solar corona. This is Figure 4 in Edwin and Roberts, 1983.

fast waves are only present if the density within the tube is greater than the surrounding density. This indicates that dense coronal flux tubes can support fast waves.

1.3.2 Kink Waves

A key feature of waves in flux tubes is kink waves, also known as transverse waves. Kink waves are characterized by their sinusoidal shape, where the cross-section of the wave remains constant but the central axis moves sinusoidally. An illustration is provided in Figure 1.7, on the right. Kink waves have been the source of much study. Observations have progressed recently, with higher resolution instruments. For example in 2004, Verwichte et al. (2005) observed "tadpole-like" kink waves with periods of 90-220s, noting that their speed was significantly lower near to the solar surface; these earlier discoveries expanded greatly when authors such as Van Doorsselaere et al. (2008) interpreted a widely observed set of coronal waves as kink waves rather than Alfvén waves. In fact, kink waves are now believed to be ubiquitous in the solar atmosphere (De Pontieu et al. (2007), De Pontieu et al. (2012), Tomczyk et al. (2007), Lin et al. (2009), McIntosh et al. (2011), Okamoto & De Pontieu (2011), Kuridze et al. (2012), Morton & McLaughlin (2013), Morton et al. (2014)). This observational ubiquity has been recently supported by Bareford et al. (2016), who investigated magnetic reconnection within a network of interlaced flux tubes, performing 5 experiments, and found that

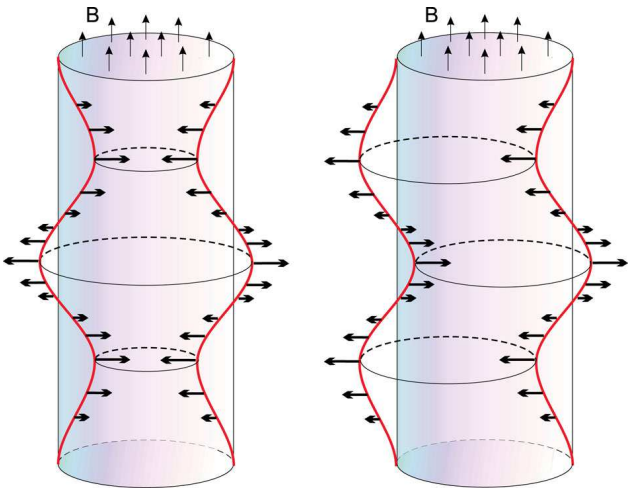

Figure 1.7: Left: An illustration of the structure of a sausage wave. Note that the cross-section varies constantly, but the central axis always points in the direction of travel. Right: An illustration of the structure of a kink wave. Note that the cross-section remains constant, despite the sinusoidal motion of the central axis. Image from Morton et al. (2012).

all of their models produced a kink instability. They also found that flux tubes with a tighter curvature have a tendency to be more unstable. This adds fuel to the idea of the importance of kink waves in the solar atmosphere.

One of the questions arising from this is for how long can such waves propagate. The results of authors such as Pascoe et al. (2016), who performed a statistical study to show that damping of kink oscillations in coronal loops could be described by an exponential profile, or alternatively by a gaussian profile, suggest that the oscillations would decay quite rapidly. However, Soler & Terradas (2015) found the damping of kink waves, to be a two-stage process where stage one consists of fast damping and stage two consists of constant oscillations without damping (see Figure 1.8). This would suggest that kink waves can continue to propagate for a long time in the solar atmosphere, albeit at a greatly decreased amplitude. Furthermore, the research of Yu et al. (2015) found that the lowest order kink modes were unable to escape whatever their wave-number; however other kink modes and all sausage modes were leaky for low values of k. The mechanism for damping is held to be mode coupling, where the oscillatory motion is converted into torsional motion (Goddard & Nakariakov (2016), Hood et al. (2013)).

Kink waves can also be fast: Guo et al. (2015) found a fast standing kink wave in a coronal loop system with a velocity in the region of 800km s^{-1}, showing that fast as well as magneto-acoustic waves can be observed in coronal loops. They found further that the period of the oscillations was 530s for the fundamental node and in the order of 300s for the first overture.

Kink modes are also held to be responsible for causing major changes to the configuration of solar structures:

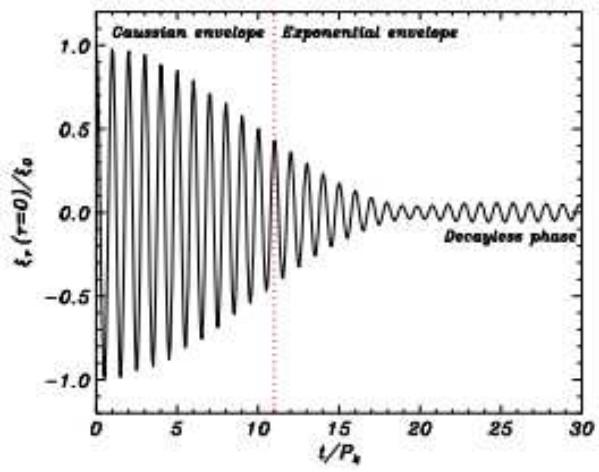

Figure 1.8: Two-stage damping of waves, according to Soler & Terradas (2015). This image was Figure 11 in their paper.

Hood et al. (2016) modeled an MHD avalanche in a cluster of flux tubes, and found that only one of the flux tubes needs to become unstable to make the entire configuration unstable. They found that a tube with a kink instability could interact with the surrounding flux tubes and radically change the magnetic field. This was found to release a significant amount of free energy within the configuration as a whole.

Although kink waves are not the main subject of this work, they are clearly an important component of the solar atmosphere, and further details can be found in reviews, such as De Moortel & Nakariakov (2012) and Mathioudakis et al. (2013)

1.3.3 Sausage Waves

Sausage waves are so named since they resemble a string of sausages. The central axis is entirely straight, in the direction of the wave's travel, but the cross-section of the wave expands and contracts regularly. An illustration of this is provided on the left in Figure 1.7.

Further details have been published by authors such as Lopin & Nagorny (2015), Moreels et al. (2013), Spruit (1982), Nakariakov et al. (2003), Melnikov et al. (2005), Srivastava et al. (2008), Nakariakov & Melnikov (2009), Vasheghani Farahani et al. (2014), Hornsey et al. (2014), Pascoe et al. (2009).

1.3.4 Bright blobs

An intriguing feature observed in filaments and in coronal loops is moving bright blobs. These can be considered as an effect of less visible waves or as flows; the waves vs flows conflict will be dealt at more

length in a later chapter. The bright blobs are therefore very useful for studies of solar structure dynamics, for instance Deng et al. (2002) used bright blobs to observe counter-streaming motions in a solar filament.

McIntosh & De Pontieu (2009) observed bright blobs with speeds of $100 - 140$km s^{-1} and discussed whether these were flows or waves. They eventually interpreted these as upflows. Tian et al. (2011) also explained the movements of bright blobs in solar prominences as upflows, rather than waves, mostly due to the lack of evidence of oscillations in their observations of Doppler shifts. However, Mariska et al. (2008) found from HINODE observations that some features which appeared to be upflows were in fact waves, citing the evidence of oscillations with period of approximately 10 minutes in the observed Doppler shifts in the solar corona. Following this, Wang et al. (2009) interpreted rising blobs in solar prominences as waves, on the basis of HINODE observations, and speculated that these may result from waves "leaking" through the chromosphere and into the corona. They also suggested that this may also happen in solar spicules.

Zhang et al. (2016) observed bright blobs as features of coronal jets in coronal loops, with size 4.5-9Mm and velocity 140-380km s^{-1}. The temperature of the blobs was estimated as 1.8-3.1MK. Intriguingly, they interpreted the bright blobs as the sole observable manifestation of the coronal jets, implying that the coronal jets observed were composed of a series of bright blobs.

1.3.5 EIT Waves and their Interaction with Solar Filaments

EIT waves, first observed by Dere et al. (1997) and Moses et al. (1997), are radial waves which propagate isotropically for significant distances across the quiet Sun; however they do not occur in coronal holes or active regions. They are observed using EUV observations, and they have observed speeds of 100-250km s^{-1}. They are however diffusive, which reduces their strength at large distances from their epicenter. (Admiranto et al., 2015)

Okamoto et al. (2004) studied 14 instances of EIT waves, and compared them with H-α data. They found that 11 of the EIT waves were associated with filament eruptions, 1 was associated with filament oscillations and 3 were associated with Morton waves. This suggests that EIT waves could be a cause of filament oscillations and/or eruptions. However, they cite a case where they studied a number of filaments within range of an EIT wave but only found consequent oscillations in 4 of them as raising the possibility that EIT waves do not necessarily cause oscillations in a filament. Despite this, whether caused by EIT waves or not, oscillations are a common and major part of filament dynamics and can propagate for large distances along filaments: Okamoto et al. (2007) observed numerous coherent oscillations in filament threads as far as 16,000km.

1.3.6 Moreton Waves and their Interaction with Solar Filaments

Moreton waves, first observed by Moreton (1960), are waves which propagate radially in an arc; that is to say, in contrast to EIT waves they have a clear direction of travel. The angle of the arc where the Moreton waves propagate is estimated to be approximately 90 degrees (Admiranto et al., 2015), and Morton waves are observed to have velocities in the order of 500-2000km s^{-1}. For instance, Srivastava & Goossens (2013) observed a wave front in the corona propagating at approximately 750km s^{-1}, and periods of 795s and 530s. Moreton waves are not as diffusive as their EIT counterparts and have been observed to travel up to 500Mm (Krause et al., 2015)

Moreton Waves and EIT waves are commonly believed to be related, and various authors have observed them co-spatially (Khan & Aurass (2002), Warmuth et al. (2001), Pohjolainen et al. (2001), Thompson et al. (2000)). Some of these authors have theorized that EIT waves may simply be decelerated Moreton waves. However, Eto et al. (2002) observed a Moreton wave and an EIT wave with similar characteristics but claimed that they propagated from different locations. Major differences commonly cited between Moreton Waves and EIT waves are their vastly different velocities and the much more diffusive nature of EIT waves. Also, EIT waves propagate radially, whilst Moreton waves propagate in a particular direction of travel (Okamoto et al., 2004).

Eto et al. (2002) observed a Moreton Wave and its interaction with a quiescent filament. They observed the Moreton wave traveling with an average velocity of approximately 715km s^{-1}, but the wave ceased to be visible in their observations before arriving at the filament. However, at the time when the Moreton wave was expected to arrive at the filament, they observed oscillations in the filament. They also observed a prominence eruption which occurred in the same direction as the Moreton wave's direction of travel. They also observed an EIT wave in a similar area but did not detect any oscillations associated with this. These findings suggest that Moreton waves can cause oscillations in filaments and can also cause eruptions. It could be argued that this kind of relationship may explain why oscillations and eruptions of filaments have frequently been observed at similar times. Gilbert et al. (2008) observed similar phenomena, this time observing three Moreton waves activating different filaments with different consequences. The authors postulated that the difference in oscillations could be a result of both the characteristics of the Moreton wave and also the different expected heights of the two filaments: perhaps the Moreton waves have a different effect at filaments of different altitudes.

1.3.7 Solitons

Solitons are a special class of waves first observed in 1844 (Russell (1844)) and first explained mathematically in 1895 (Korteweg & de Vries (1895)). They consist of a single pulse which, given constant external conditions, retains its shape and intensity as it travels. The possibilities for solitons in solar structures is exciting and has merited study as a special case in terms of waves. The theoretical study of solitons in flux tubes i.e. in coronal loops, filaments and spicules, became a growing field in the 1980s, for instance, Roberts & Mangeney (1982) modeled solitons in flux tubes, and found that a "tube soliton" could propagate at around 7km s^{-1} and that "external solitons" could propagate at about 11km s^{-1}. External soliton was a terminology applied to a second solution to equations in the scenario when the flux tube is slightly cooler than the surrounding plasma. They also found that the speed of the soliton exceeds the usual speed within the tube, and that the difference between the two is proportional to the velocity amplitude. They also found that the speed of the soliton only depends on the parameters of the slab, and not the parameters of the surrounding plasma. These early studies underpinned the study of solitons in flux tubes. It later became apparent that there are several types of solitons in flux tubes, for instance Wu et al. (1996) and Wu et al. (1997) discovered a new type of density soliton: the dipole density soliton, as well as detecting single dip density solitons and hump density solitons. More recently, Garcia de Andrade (2007) made a theoretical study of solitons, finding a new set of solutions for vortex filaments (thin strips of vorticity) in coronal loops, taking into account the effects of diffusion.

More recently, observations have suggested that solitons take the form of bright blobs. For instance Zaqarashvili et al. (2010) observed a blob traveling with a speed of approximately 35km s^{-1} in the solar atmosphere, which was significantly greater than the surrounding sound speed. They also noticed that as the flux tube became wider, the blob also became wider. The options of kink or Alfvén pulses were excluded, leading to the conclusion that the blob was a manifestation of a pressure pulse. Since leakage was not observed, they concluded that a slow sausage soliton was the most likely explanation for the bright blob. The idea that a bright blob can propogate more rapidly than the sound speed is supported by the research of Ballai et al. (2003), who studied solitary waves in the solar wind and found that, in the case of solitons, the non-linear magneto-acoustic waves propapagate faster than the linear sound speed for the plasma.

Solitons are held to propagate in various structures in the solar chromosphere and corona, and may have great significance: Ryutova & Hagenaar (2007) argued that solitons are an extremely important component of solar surface dynamics, and particularly in penumbral environments. In fact, they claim to show that all types of moving magnetic features can be explained using shocks and solitons. They showed that non-linear

coupling of magnetic fields and plasma flows causes a magnetic kink, which could be represented by a soliton or by a shock.

1.3.8 Flares as a trigger for filament activity

There is also a lot of evidence for flares triggering filament activity. This has been observed, sometimes in a vertical direction and sometimes in a horizontal direction, by a number of authors including Jing et al. (2003), Jing et al. (2006), Vršnak et al. (2007), Kleczek & Kuperus (1969) and Hershaw et al. (2011).

1.4 The Research

This research seeks to expand understanding of the processes which occur in solar filaments. Such understanding could be arrived at both by modeling and by observational methods, hence the thesis uses both to try to develop understanding of processes in solar filaments. SDO data is used to observe, analyze and model events. To this end, the research in this thesis involves three themes, one modeling and two observational, which are divided into three chapters.

1.4.1 A New Method for Non-Linear Force-Free Field Modeling

Non-Linear Force Free Field (NLFFF) modeling is a popular and active area of solar physics research. It attempts to model solar structures by extrapolating from the underlying magnetic field. Many methods exist for this modeling, however most methods only have a temporal cadence of 12 minutes. In this chapter, a cutting-edge area of Non-Linear Force Free modeling is significantly expanded to allow 3D multi-wavelength models with 45 second cadence; this is important because it allows prediction of rapid changes to the structures under study. The modeling of fast-developing systems would be significantly more complete with a 45 second cadence. The original intention was to use this method to model a solar filament; however the method as it stands concentrates on the areas with the strongest magnetic field and is therefore not currently suitable for filament modeling. As a result, a system of coronal loops are studied, with an intention for further expansion of such methods to allow modeling of solar filaments in the future; three-dimensional multi-wavelength models of the system are created to visualize the system in three dimensions. This also allows comparison between the different wavelengths, which represent plasma of different temperatures; as a result the chapter deduces some of the temperature distribution in the coronal loop system. Also, the

chapter attempts to draw conclusions about an eruptive event, including a calculation of the free energy released in the eruption.

1.4.2 Observation and Discussion of Wave Trains in a Solar Filament

In the following chapter, wave trains are observed in a solar filament, which I believe to be the first observations of their kind. These are interpreted as two very fast waves propagating across flux tubes in a solar filament, which in turn cause a succession of magneto-acoustic waves in different flux tubes. These are interpreted as waves rather than flows due to significant acceleration and deceleration in one of the features. Following these exciting observations, the chapter attempts to explain the origin of this phenomenon, and finds a significant decrease in magnetic flux in a region of strong polarity where the very fast waves were seen to originate, co-temporal with the beginning of the wave trains phenomenon.

1.4.3 Observing, Classifying and Discussing the Causes of Counter-Streaming Motions in a Solar Filament

Finally, counter-streaming motions are observed and discussed. Counter-streaming motions are a frequently observed feature of solar filaments. However these flows are usually slow and derived from H-α observations. In this chapter, widespread counter-streaming motions are observed in a solar filament using AIA data, showing the ubiquity of fast motions in EUV and attempting to discover their properties. These are interpreted as waves rather than mass flows and it is thus postulated that many features in other filaments which could be interpreted as mass flows may in fact be waves, which is a contribution to the waves vs flows controversy. Through analysis of the magnetic field, observations of motions propagating in both directions from the same area and observations of the "reversal" of motions in the same flux rope, this chapter also offers possible explanations for the fascinating phenomenon of counter-streaming.

Bibliography

Admiranto, A. G., Priyatikanto, R., Yus'an, U., & Puspitaningrum, E. 2015, American Institute of Physics Conference Series, 1677, 050014

Alexander, C. E., Walsh, R. W., Régnier, S., et al. 2013, The AstroPhysical Journal Letters, 775, L32

Athay, R.G., Holzer, T.E. 1982, The AstroPhysical Journal, 255, 743

Anzer, U., & Poland, A. I. 1979, Solar Physics, 61, 95

Arregui, I., Oliver, R., & Ballester, J. L. 2012, Living Reviews in Solar Physics, 9,

Ballai, I., Thelen, J. C., Roberts, B. 2003, Astronomy & Astrophysics, 404, 701

van Ballegooijen, A. A., & Martens, P. C. H. 1989, The AstroPhysical Journal, 343, 971

van Ballegooijen, A. A., & Cranmer, S. R. 2010, The AstroPhysical Journal, 711, 164

Bareford, M. R., Gordovskyy, M., Browning, P. K., & Hood, A. W. 2016, Solar Physics, 291, 187

Bennett, S. M., & Erdélyi, R. 2015, The AstroPhysical Journal, 808, 135

Berger, T. E., Shine, R. A., Slater, G. L., et al. 2008, The AstroPhysical Journal Letters, 676, L89

Berger, T. E., Shine, R. A., Slater, G. L., et al. 2008, The AstroPhysical Journal Letters, 676, L89

Berger, T. E., Slater, G., Hurlburt, N., et al. 2010, The AstroPhysical Journal, 716, 1288

Berger, T., Testa, P., Hillier, A., et al. 2011, Nature, 472, 197

Browning, P., & Gordovskyy, M. 2011, AGU Fall Meeting Abstracts

Carlsson, M., Leenaarts, J., & De Pontieu, B. 2015, The AstroPhysical Journal Letters, 809, L30

Chae, J., Moon, Y.-J., & Park, Y.-D. 2005, The AstroPhysical Journal, 626, 574

Chae, J. 2010, The AstroPhysical Journal, 714, 618

Chen, S.-X., Li, B., Xia, L.-D., & Yu, H. 2015, Solar Physics, 290, 2231

Cheung, M. C. M., De Pontieu, B., Tarbell, T. D., et al. 2015, The AstroPhysical Journal, 801, 83

Cranmer, S.R. 2009, Living Reviews in Solar Physics, 6, 3

Cranmer, S. R., & Woolsey, L. N. 2015, The AstroPhysical Journal, 812, 71

Dahlburg, R. B., Einaudi, G., Taylor, B. D., et al. 2016, The AstroPhysical Journal, 817, 47

Demoulin, P., Priest, E. R., & Anzer, U. 1989, Astronomy & Astrophysics, 221, 326

Deng, Y., Lin, Y., Schmieder, B., & Engvold, O. 2002, Solar Physics, 209, 153

Dere, K. P., Brueckner, G. E., Howard, R. A., et al. 1997, Solar Physics, 175, 601

Dorotovič, I., Rybak, J., Garcia, A., Journoud, P. 2010, Proceedings of the 20th National Solar Physics Meeting, Slovak Central Observatory, Hurbanovo, 58

Van Doorsselaere, T., Nakariakov, V. M., & Verwichte, E. 2008, The AstroPhysical Journal Letters, 676, L73

Durak, N., Nasraoui,O., Gomez,J., Gonzalez,F., Elgazzar,H., Sellah,S., Rojas,C., Schmelz,J., Roames,J., Nasraoui,K. 2007, NAFIPS, 514

Edwin, P. M., & Roberts, B. 1983, Solar Physics, 88, 179

Eto, S., Isobe, H., Narukage, N., et al. 2002, Publications of the Astronomical Society of Japan, 54, 481

Garcia de Andrade, L. C. 2007, AstroPhysics & Space Science, 312, 161

Gibson, S. E., & Fan, Y. 2006, The AstroPhysical Journal Letters, 637, L65

Gilbert, H. R., Daou, A. G., Young, D., Tripathi, D., & Alexander, D. 2008, The AstroPhysical Journal, 685, 629-645

Goddard, C. R., & Nakariakov, V. M. 2016, Astronomy & Astrophysics, 590, L5

Golub, L. & Pasachoff, J. 1997, The Solar Corona

Gosling, J.T., Pizzo, V.J. 1999, Space Science Reviews, 89, 21

Guo, Y., Erdélyi, R., Srivastava, A. K., et al. 2015, The AstroPhysical Journal, 799, 151

Hegde, M., Hiremath, K. M., & Doddamani, V. H. 2012, 39th COSPAR Scientific Assembly, 39, 739

Hershaw, J., Foullon, C., Nakariakov, V. M., & Verwichte, E. 2011, Astronomy & Astrophysics, 531, A53

Hillier, A., Isobe, H., & Watanabe, H. 2011, Publications of the Astronomical Society of Japan, 63, 19

Hillier, A. S., Isobe, H., Shibata, K., & Berger, T. E. 2011, Astronomical Society of India Conference Series, 2,331

Hood, A. W., Ruderman, M., Pascoe, D. J., et al. 2013, Astronomy & Astrophysics, 551, A39

Hood, A. W., Cargill, P. J., Browning, P. K., & Tam, K. V. 2016, The AstroPhysical Journal, 817, 5

Hornsey, C., Nakariakov, V. M., & Fludra, A. 2014, Astronomy & Astrophysics, 567, A24

Jain, R., Maurya, R. A., & Hindman, B. W. 2015, The AstroPhysical Journal Letters, 804, L19

Janssen, P. 1869, Proc. Acad. Sci., 68, 367

Janssen, P. 1869, Astronomical Register, 7, 132

Japaridze, D. R., Bagashvili, S. R., Shergelasvili, B. M., & Chargeishvili, B. B. 2015, Astrophysics, 58, 575

Jing, J., Lee, J., Spirock, T. J., et al. 2003, The AstroPhysical Journal Letters, 584, L103

Jing, J., Lee, J., Spirock, T. J., & Wang, H. 2006, Solar Physics, 236, 97

Khan, J. I., & Aurass, H. 2002, Astronomy & Astrophysics, 383, 1018

Kippenhahn, R. & Schlüter, A. 1957, Z. Astrophys, 43, 36

Kittinaradorn, R., Ruffolo, D., & Matthaeus, W. H. 2009, The AstroPhysical Journal Letters, 702, L138

Kleczek, J., & Kuperus, M. 1969, Solar Physics, 6, 72

Korteweg, D. J., & de Vries, F. 1895, Philos. Mag., 39, 422-443

Krause, G., Cécere, M., Francile, C., et al. 2015, Monthly Notices of the Royal Astronomical Society, 453, 2799

Krieger, A. S., Timothy, A. F., & Roelof, E. C. 1973, Solar Physics, 29, 505

Kumar, P., Nakariakov, V. M., & Cho, K.-S. 2015, The AstroPhysical Journal, 804, 4

Kuridze, D., Morton, R. J., Erdélyi, R., et al. 2012, The AstroPhysical Journal, 750, 51

Kushwaha, U., Joshi, B., Veronig, A. M., & Moon, Y.-J. 2015, The AstroPhysical Journal, 807, 101

Labrosse, N., Heinzel, P., Vial, J.-C., et al. 2010, Space Science Reviews, 151, 243

Leroy, C., Rancoita, P. G. 2015, Principles of Radiation Interaction in Matter Detection

Lin, Y., Engvold, O. R., & Wiik, J. E. 2003, Solar Physics, 216, 109

Lin, Y., Engvold, O., Rouppe van der Voort, L., Wiik, J. E., & Berger, T. E. 2005, Solar Physics, 226, 239

Lin, Y., Wiik, J. E., Engvold, O., Rouppe van der Voort, L., & Frank, Z. A. 2005, Solar Physics, 227, 283

Lin, Y., Soler, R., Engvold, O., et al. 2009, The AstroPhysical Journal, 704, 870

Lockyer, N. 1868, Comptes rendus hebdomadaires des séances de l'Académie des sciences, p836

Lopin, I., & Nagorny, I. 2015, The AstroPhysical Journal, 810, 87

Low, B. C. 1982, Solar Physics, 75, 119

Low, B. C., & Petrie, G. J. D. 2005, The AstroPhysical Journal, 626, 551

Mariska, J. T., Warren, H. P., Williams, D. R., & Watanabe, T. 2008, The AstroPhysical Journal Letters, 681, L41

Mathioudakis, M., Jess, D. B., & Erdélyi, R. 2013, Space Science Reviews, 175, 1

McIntosh, S. W., & De Pontieu, B. 2009, The AstroPhysical Journal Letters, 706, L80

McIntosh, S. W., de Pontieu, B., Carlsson, M., et al. 2011, Nature, 475, 477

Melnikov, V. F., Reznikova, V. E., Shibasaki, K., & Nakariakov, V. M. 2005, Astronomy & Astrophysics, 439, 727

Milne, A. M., Priest, E. R., & Roberts, B. 1979, The AstroPhysical Journal, 232, 304

De Moortel, I., & Nakariakov, V. M. 2012, Philosophical Transactions of the Royal Society of London Series A, 370, 3193

Moreels, M. G., Goossens, M., & Van Doorsselaere, T. 2013, Astronomy & Astrophysics, 555, A75

Moreton, G.E. 1960 Astronomical Journal, 64, 494

Morton, R. J., Verth, G., Jess, D. B., et al. 2012, Nature Communications, 3, 1315

Morton, R. J., & McLaughlin, J. A. 2013, Astronomy & Astrophysics, 553, L10

Morton, R. J., Verth, G., Hillier, A., & Erdélyi, R. 2014, The AstroPhysical Journal, 784, 29

Moses, D., Clette, F., Delaboudinière, J.-P., et al. 1997, Solar Physics, 175, 571

Muller, R., Utz, D., & Hanslmeier, A. 2011, Solar Physics, 274, 87

Nakariakov, V. M., Melnikov, V. F., & Reznikova, V. E. 2003, Astronomy & Astrophysics, 412, L7

Nakariakov, V. M., & Melnikov, V. F. 2009, Space Science Reviews, 149, 119

NASA 2014, <http://solarscience.msfc.nasa.gov/feature1.shtml>, Photospheric Features, accessed March 2016

NASA 2015, The Solar Interior, <http://solarscience.msfc.nasa.gov/interior.shtml>, accessed March 2016

Neupert, W.M., Pizzo, V. 1974, J. Geophys. Res., 79, 3701

Nolte, J. T., Krieger, A. S., Timothy, A. F., et al. 1976, Solar Physics, 46, 303

Okamoto, T. J., Nakai, H., Keiyama, A., et al. 2004, The AstroPhysical Journal, 608, 1124

Okamoto, T. J., Tsuneta, S., Berger, T. E., et al. 2007, Science, 318, 1577

Okamoto, T. J., & De Pontieu, B. 2011, The AstroPhysical Journal Letters, 736, L24

Pascoe, D. J., Nakariakov, V. M., Arber, T. D., & Murawski, K. 2009, Astronomy & Astrophysics, 494, 1119

Pascoe, D. J., Goddard, C. R., Nisticò, G., Anfinogentov, S., & Nakariakov, V. M. 2016, Astronomy & Astrophysics, 585, L6

Pike, C. D., & Harrison, R. A. 1997, Solar Physics, 175, 457

Pinto, R. F., Gordovskyy, M., Browning, P. K., & Vilmer, N. 2016, Astronomy & Astrophysics, 585, A159

Pneuman, G.W., Kopp, R.A. 1978, Solar Physics, 57, 49

Pohjolainen, S., Maia, D., Pick, M., et al. 2001, The AstroPhysical Journal, 556, 421

De Pontieu, B., McIntosh, S. W., Carlsson, M., et al. 2007, Science, 318, 1574

De Pontieu, B., Carlsson, M., Rouppe van der Voort, L. H. M., et al. 2012, The AstroPhysical Journal Letters, 752, L12

Reva, A., Shestov, S., Zimovets, I., Bogachev, S., & Kuzin, S. 2015, Solar Physics, 290, 2909

Roberts, B., & Mangeney, A. 1982, Monthly Notices of the Royal Astronomical Society, 198, 7P

Russell, J. S. 1844, Report of the 14th Meeting of the British Association for the Advancement of Science. London: John Murray, 311-390

Ryutova, M., & Hagenaar, H. 2007, Solar Physics, 246, 281

Sakurai, T. 1976, Publications of the Astronomical Society of Japan, 28, 177

Schmelz, J. T. 2011, Bulletin of the American Astronomical Society, 43, 213.02

Schmelz, J. T., Pathak, S., Christian, G. M., Dhaliwal, R. S. S., & Paul, K. S. 2015, The AstroPhysical Journal, 813, 71

Schmieder, B., Mein, N., Deng, Y., et al. 2004, Solar Physics, 223, 119

Schwartz, P., Heinzel, P., Kotrč, P., et al. 2015, Astronomy and Astrophysics, 574, A62

Seeds, M. A., Backman, D., Montgomery, M. M. 2016 Horizons: Exploring the Universe, Enhanced

Skogsrud, H., Rouppe van der Voort, L., De Pontieu, B., & Pereira, T. M. D. 2015, The AstroPhysical Journal, 806, 170

Soler, R., & Terradas, J. 2015, The AstroPhysical Journal, 803, 43

Spruit, H. C. 1982, Solar Physics, 75, 3

Srivastava, A. K., Zaqarashvili, T. V., Uddin, W., Dwivedi, B. N., & Kumar, P. 2008, Monthly Notices of the Royal Astronomical Society, 388, 1899

Srivastava, A. K., & Goossens, M. 2013, The AstroPhysical Journal, 777, 17

Stix, M. 1989, The Sun An Introduction

Tajfirouze, E., Reale, F., Peres, G., & Testa, P. 2016, The AstroPhysical Journal Letters, 817, L11

Tavabi, E., Koutchmy, S., Ajabshirizadeh, A., Ahangarzadeh Maralani, A. R., & Zeighami, S. 2015, Astronomy & Astrophysics, 573, A4

University of Tennessee 2010, <http://csep10.phys.utk.edu/astr162/lect/sun/photosphere.html> Accessed March 2016

Tian, H., McIntosh, S. W., & De Pontieu, B. 2011, The AstroPhysical Journal Letters, 727, L37

Thompson, B. J., Reynolds, B., Aurass, H., et al. 2000, Solar Physics, 193, 161

Tomczyk, S., McIntosh, S. W., Keil, S. L., et al. 2007, Science, 317, 1192

Tsurutani, B. T., Gonzalez, W. D., Gonzalez, A. L. C., et al. 1995, Journal of Geophysical Research, 100, 21717

UCAR Science Education 2014, The Sun's Chromosphere, accessed March 2016

Vasheghani Farahani, S., Hornsey, C., Van Doorsselaere, T., & Goossens, M. 2014, The AstroPhysical Journal, 781, 92

Verwichte, E., Nakariakov, V. M., & Cooper, F. C. 2005, Astronomy & Astrophysics, 430, L65

Vial, J.C., Engvold, O. 2015, Solar Prominences

Vršnak, B., Veronig, A. M., Thalmann, J. K., & Žic, T. 2007, Astronomy & Astrophysics, 471, 295

Wang, Y.-M. 1999, The AstroPhysical Journal Letters, 520, L71

Wang, T. J., Ofman, L., & Davila, J. M. 2009, The AstroPhysical Journal, 696, 1448

Warmuth, A., Vršnak, B., Aurass, H., & Hanslmeier, A. 2001, The AstroPhysical Journal Letters, 560, L105

Wu, D. J., Huang, G. L., Wang, D. Y. 1996, Physical Review Letters, 77, 4346

Xia, C., Chen, P. F., & Keppens, R. 2012, The AstroPhysical Journal Letters, 748, L26

Yu, H., Li, B., Chen, S.-X., & Guo, M.-Z. 2015, The AstroPhysical Journal, 814, 60

Wu, D. J., Wang, D. Y, Huang, G. L. 1997, Phys. Plasmas, 4 (3), 611

Zaqarashvili, T. V., Kukhianidze, V., & Khodachenko, M. L. 2010, Monthly Notices of the Royal Astronomical Society, 404, L74

Zhang, Q. M., Ji, H. S., & Su, Y. N. 2016, arXiv:1601.04390

Zimovets, I. V., & Nakariakov, V. M. 2015, Astronomy & Astrophysics, 577, A4

Chapter 2

Instrumentation

All observational data used in this work is derived from the Solar Dynamics Observatory (SDO). The SDO has many advantages over other telescopes, including spatial and temporal cadence, easy comparison of coronal and magnetic field data, a full-disc field of view and uninterrupted observations. The SDO contains three instruments, as outlined below.

2.1 The Solar Dynamics Observatory (SDO)

The Solar Dynamics Observatory was launched on 11^{th} February 2011, at Cape Canaveral, Florida (NASA, 2010), as part of NASA's Living With a Star program. It aims to image the solar disc at a very high resolution using a series of telescopes which detect different aspects of the solar surface. The SDO contains three telescopes, the Atmospheric Imaging Assembly (AIA), the Helioseismic Magnetic Imager (HMI) and the EUV Variability Experiment (EVE), and between them they collect a huge amount of data and send approximately 1.5Tb of data each day back to Earth. The AIA focuses on the dynamics of plasma in the chromosphere and corona, the HMI focuses on the magnetic field in the photosphere and the EVE focuses on the output of heat radiation from the Sun and its temperature, in an attempt to understand the processes of solar heating.

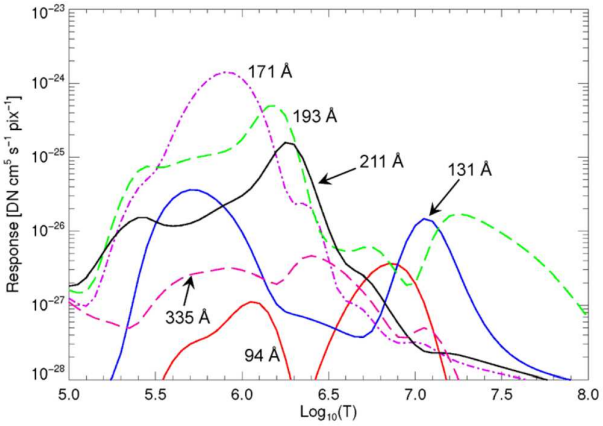

Figure 2.1: How the sensitivity of different wavelengths varies with the temperature of the plasmas being studied, image from Lemen et al, 2012.

2.1.1 AIA

The AIA telescope system is one of the three instruments on the SDO. It consists essentially of four Cassegrain telescopes, three of which focus on 2 wavelengths each and one of which focuses on 4 wavelengths. Telescope 1 observes the Sun in the 131Å and 335Å wavelengths. Telescope 2 observes the Sun in the 193Å and 211Å wavelengths. Telescope 3 observes the Sun in the 171Å wavelengths and also three Ultra-Violet (UV) wavelengths - 1600Å, 1700Å and 4500Å. Telescope 4 provides observations in the 94Å and 304Å wavelengths. Most of the telescopes have filter wheels which can change the wavelength studied Lemen et al. (2012). Each of the telescopes has a primary mirror of diameter 20cm and a secondary mirror. A mechanical shutter starts and ends the exposure time (Lemen et al., 2012). The Charge-Coupled Devices (CCDs) are 4096 pixels $\times$ 4096 pixels, where each pixel corresponds to 0.6 arcseconds $\times$ 0.6 arcseconds. This allows a high spatial resolution. The temporal cadence of the observations is 12 seconds for each wavelength, with an exposure time of 2 seconds. Hence, AIA provides 16 times as many pixels per image as its immediate predecessor on the SOHO observatory, with 700 times the frequency for each wavelength, and twice the number of wavelengths. This provides a large amount of useful data which helps to analyze the dynamics of the solar corona and its structures.

The different wavelengths observed concentrate on plasmas within a certain temperature range. Figure 2.1, which was Figure 13 in Lemen et al (2012) shows how the CCDs for the different wavelengths respond to different plasma temperatures. The peaks for each wavelength represent the main temperatures that the data for that wavelength will concentrate on, whilst the troughs indicate the temperatures of plasma that will be less prominent in the data for that wavelength.

The 4500Åand 1700Åwavelengths concentrate on plasma with a temperature of approximately $10^{3.7}$K, whilst the 1600Åwavelength concentrates on plasma with a temperature of around 10^5K: this demonstrates the range of temperatures which can be studied with UV observations. Moving on to the Extreme Ultra-Violet (EUV) wavelengths, which are used extensively in this research, the 94Åwavelength concentrates on the Fe XVIII ions which indicate plasma temperatures in the order of $10^{6.8}$K. The 131Åwavelength concentrates on the Fe VIII and Fe XXI ions, with typical temperatures of around $10^{5.6}$K and 10^7K. The 171Åwavelength concentrates on the Fe IX, Fe X and Fe XI ions, with temperatures around 10^6K. The 193Åwavelength observations concentrate on Fe XII and XXIV ions, with temperatures of $10^{6.2}$K and $10^{7.3}$K respectively, whilst the 211Åwavelength concentrates on plasma containing many Fe XIV ions: the characteristic temperature is similar to that of the Fe XII line, $10^{6.3}$K. The 304Åwavelength focuses on the He II ions, with a characteristic temperature of around $10^{4.7}$K, whilst the 335Åwavelength focuses on the Fe XVI ions, with a typical typical temperatures of approximately $10^{6.4}$K. Hence the different telescopes and wavelengths observe a wide range of temperatures, allowing such applications as temperature maps and temperature detection in flares and large-scale solar structures.

2.1.2 HMI

The Helioseismic Magnetic Imager (HMI) is an instrument on the SDO which observes the full solar disc, focusing on the Fe I line, with wavelength 6173Å. This data provides a two-dimensional representation of the magnetic field in the photosphere, and is hence very different from the data obtained by AIA. Whereas the AIA data shows the dynamics of structures on the solar surface, the HMI data gives insight into the magnetic activity that is often held to influence the dynamics of structures on the solar surface. So the HMI and AIA data, whilst being radically different at first sight, complement each other very well in solar research.

The principal components of the HMI apparatus consist of an optics package, an electronics box, and a connector between the two. The optics package supports two CCDs and two Camera Electronics Boxes. The initial point of contact for sunlight reaching the instrument is a 50Åfilter made from various layers of different glasses which deflects much of the unwanted light. There then follows a telescope of 14cm diameter, and primary and secondary lenses to direct the remaining light. There then follow a series of filters, which act to narrow the wavelength observed to 6173Åand to prevent excess heat from accumulating and thus distorting the instruments. Schou et al. (2012)

The CCDs have 4096 pixels $\times$ 4096 pixels, each of which measures 12μm $\times$ 12μm. Each pixel corresponds to

0.5 arcseconds × 0.5 arcseconds, and the resolution of the instrument is 1 arcsecond. At first glance it may appear strange that the area represented by each pixel in the AIA observations differs significantly from the area represented by each pixel in the HMI observations but the result is that the Sun appears larger in the HMI image than it does in the AIA image. This is due to the significant interest in coronal loops, flares and so on which protrude over the solar limb: these are visible in the AIA images but not in the HMI images, explaining why the Sun needs to appear smaller in an AIA image than in a HMI image.

2.1.3 EVE

This work does not use any data from the EVE apparatus, but a brief summary is included for completeness. The EVE apparatus consists of five telescopes: EEB, ESP, MEGS B, MEGS A and SAM. Each of these studies a different range of wavelengths Woods et al. (2012). The EVE apparatus has several main aims: to measure more precisely the irradiance of the Sun, to study trends in the irradiance of the Sun such as during the course of a solar cycle, to study and possibly explain short-term changes in solar irradiance, to improve temperature maps and associated models, and to try to predict the occurance of variations in solar irradiance that could for instance damage satellites.

Bibliography

Lemen, J. R., Title, A. M., Akin, D. J., et al. 2012, Solar Physics, 275, 17

NASA 2010, <http://sdo.gsfc.nasa.gov/mission/>, accessed March 2016

Schou, J., Scherrer, P. H., Bush, R. I., et al. 2012, Solar Physics, 275, 229

Woods, T. N., Eparvier, F. G., Hock, R., et al. 2012, Solar Physics, 275, 115

Chapter 3

A Multi-wavelength Model to Visualize and Analyze Magnetic Fields in the Solar Corona

3.1 Preface

Coronal loops are large structures on the solar surface (sometimes reaching an altitude of 1000s of km), which generally take a roughly semi-circular or semi-elliptical form. They are composed of threads which carry plasma. The plasma in these structures is generally hotter than the surrounding plasma, and coronal loops are seen as bright features in AIA observations. They can oscillate, move and erupt. Many attempts have been made previously to model such loops, but usually with a temporal cadence of only 12 minutes. This chapter develops recent research to expand such a method to a temporal cadence of 45 seconds, and applies this to model a set of coronal loops observed over a period of one hour. It also attempts to produce three-dimensional models in seven wavelengths: 94Å, 131Å, 171Å, 193Å, 211Å, 304Å and 335Å. The plots produced in some cases provide a fair representation of the loop system compared to AIA observations, however some of the plots are inconsistent with plots produced at a similar time. The free energy in the loop system is modeled over a period of 1 hour, and a large sudden decrease in the free energy is seen to be co-temporal with the observation of a partial eruption in AIA timelapse movies. This allows an estimate of the free energy released. However, the free energy graph is extremely erratic, and large sudden increases

in free energy also occur. Despite this, the modeled magnetic field appears to be fairly stable, and the heartening results obtained suggest that methods with 45 second temporal cadence could be useful in the future developments of NLFFF modeling.

3.2 Previous research: An Overview

A wide range of models have been created to represent solar structures such as coronal loops and filaments, including Non-Linear Force-Free Field models (NLFFF). A detailed overview of these was produced by Wiegelmann & Sakurai (2012). Such models involve creating a three-dimensional representation of the magnetic field, and sometimes also the electrical field and other factors, and then extrapolating magnetic field lines based on the derived magnetic field and other factors. Several theoretical problems in the field were solved by analytical methods for instance by Low & Lou (1990), although these cannot include all real-world scenarios. Several authors have aimed to model real-world situations by using various methods which will be explained in a later subsection. For instance, Wiegelmann (2004), Wheatland (2006), Tadesse et al. (2014) and Guo et al. (2012) succeeded in creating accurate models of solar structures. Some authors have used magneto-frictional methods, for example Su et al. (2009) succeeded in modeling a solar flare in an active region, and Kliem et al. (2013) modeled an active region eruption that was observed on 8 April 2008. Others have used MHD models, for instance Jiang & Feng (2013) simulated coronal loops very accurately. Some authors have used the Grad-Rubin method, and the results obtained were a good match to the observations in Malanushenko et al. (2012), for instance. More recently, a forward-fitting method was proposed which uses EUV observations, (Aschwanden, 2013b).

The accuracy of such methods can be tested by a range of techniques, including visual comparisons of observations with the simulated structures, and study of the misalignment angle which will be mentioned later.

3.3 Modeling solar processes

3.3.1 The Force-Free Assumption

When modeling an area of the Sun, assumptions must be made to produce a solvable problem. We begin by noting that the magnetic field $\boldsymbol{B}$ is continuous, and this can be expressed mathematically by:

$\nabla \cdot \boldsymbol{B} = 0$

A plasma in the presence of a magnetic field is now considered, and a low plasma-beta value is assumed: that is, the effect of the magnetic pressure by far outweighs the plasma pressure. If the plasma is in equilibrium, the below equation applies:

$\boldsymbol{j} \times \boldsymbol{B} = 0$

This is the force-free assumption. The parameter $j = \frac{1}{\mu_0}(\nabla \times \boldsymbol{B})$ denotes the current density, while μ_0 denotes the vacuum permeability.

$\frac{1}{\mu_0}(\nabla \times \boldsymbol{B}) \times \boldsymbol{B} = 0$

therefore

$(\nabla \times \boldsymbol{B}) \times \boldsymbol{B} = 0.$

This equation is highly important, since it implies that $\nabla \times \boldsymbol{B}$ is parallel to $\boldsymbol{B}$. Since these are parallel, we can write

$\nabla \times \boldsymbol{B} = \alpha \boldsymbol{B}$, where α is a scalar.

3.3.2 Setting a value for α

When modeling, it is possible to set a value for α, to enable calculations to determine the magnetic field quickly and easily. For the simplest model (the potential field), α is set to be 0 everywhere, yielding

$\nabla \times \boldsymbol{B} = 0.$

Clearly, this is a very simple model. To discover the magnetic field in the chromosphere and the corona using this equation, boundary conditions must be set for α. As an example, two point charges are placed for B in the photosphere, with strengths 1000G and -1000G respectively. The magnetic field configuration in the chromosphere and corona can now be discovered, and the result is shown in Figure 3.1. The field lines

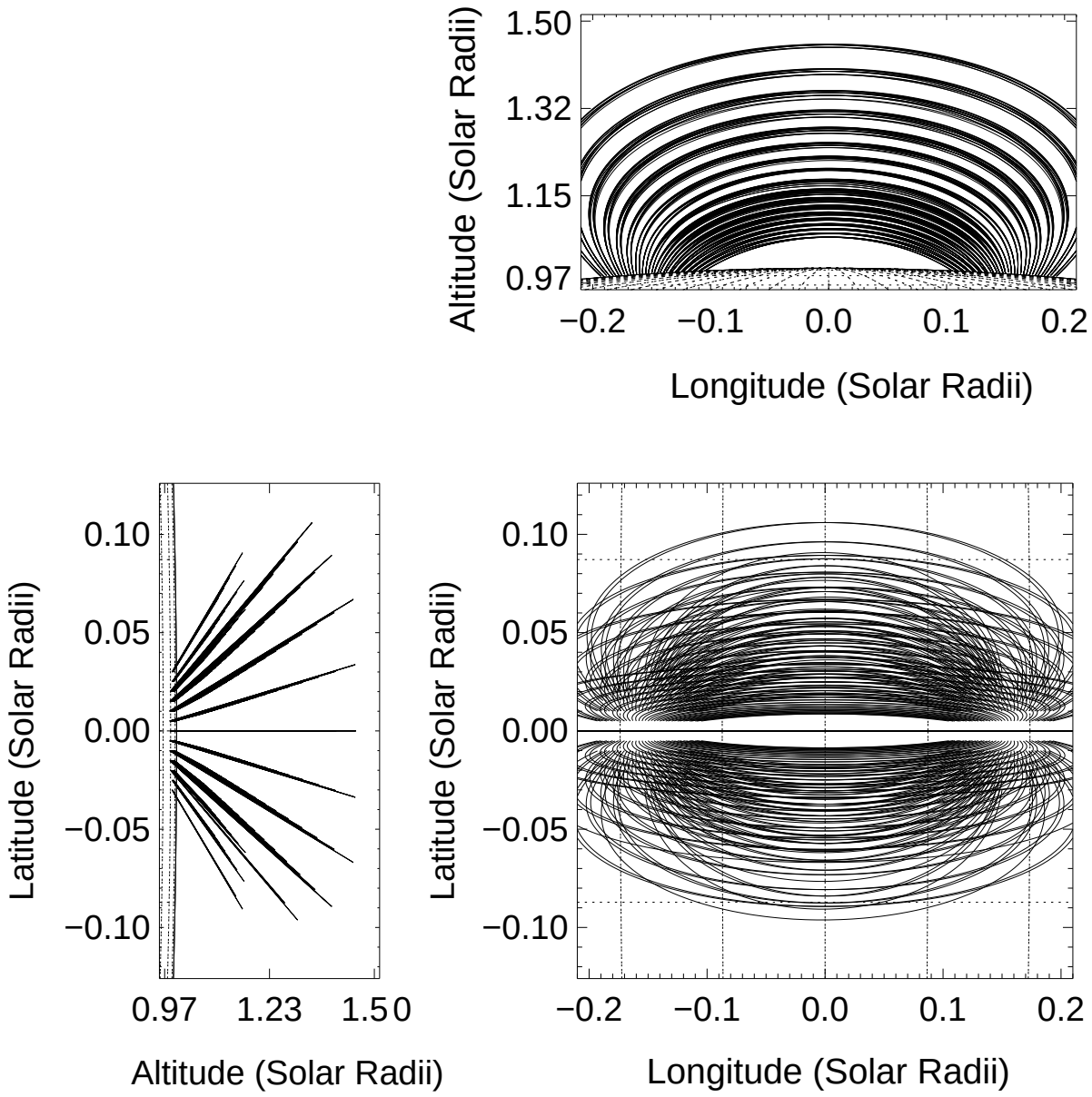

Figure 3.1: Potential field configuration ($\alpha = 0$) in the chromosphere and corona, modeled by using two point charges.

which connect the two point charges are much straighter than is frequently seen in AIA observations, and the magnetic field lines will not exhibit the twisting observed in real data.

It is also prudent to note that the twist in the magnetic field lines is believed to store the free energy (Chiueh & Zweibel, 1989). This suggests that a twistless model, such as this, has no free energy. This is another disadvantage since the model will not be a realistic situation for eruptions, flares, coronal mass ejections etc.

For accuracy and to estimate the free energy of a real magnetic field configuration, α must be allowed to be non-zero, and to take varying values. Non-Linear Force-Free Field methods (NLFFF) allow the parameter α to vary non-linearly without unreasonable restriction. Liu et al. (2012) compared the potential field model to the NLFFF model in detail, and Mackay & van Ballegooijen (2009) compared NLFFF models to Linear Force Free Field models (LFFF, where α is everywhere constant but not necessarily zero). NLFFF models were shown to be much more realistic and agreed much better with the structures seen in filaments, for instance with respect to EUV observations. For instance, the filament barbs which connect the filament to the photosphere were seen to be significantly more accurate. Given that filaments are highly non-potential structures, it is presumed that the accuracy advantage of NLFFF methods over LFFF methods would also be true for active regions and coronal loops.

3.3.3 An Overview of NLFFF methods

There are various methods of approximating solar structures by NLFFF models, all with their advantages and disadvantages in their accuracy, calculation speed, essential data inputs and temporal cadence. Most of these use the full magnetic field data in 3 dimensions, but this comes at the cost of temporal cadence: the data is generally available every 12 minutes. By using the magnetic field in 3 dimensions, models can be built which closely match observed structures. Some of the methods are described below.

The Upward Integration Method, suggested by Nakagawa (1974), aims to build a magnetic field configuration in the chromosphere and corona in 3 dimensions by beginning at one horizontal level of the chromosphere, calculating the current and α, and then using this information to estimate the magnetic field at the next level. By performing this on many levels of the chromosphere, a 3D model can be built of the magnetic field configuration. Despite this, the model can be unstable.

The Grad-Rubin method (Grad & Rubin, 1958) solves a well-posed mathematical problem. A process of iteration uses the distribution of alpha values to find the theoretical magnetic field which best corresponds to the data. However, the requirement to know the distribution of α as an input is a major disadvantage.

Chodura & Schlüter (1981) offered a time-dependent MHD method which can be used to arrive at an equilibrium by iterating in time, for instance Wiegelmann (2004) offered an optimization method to solve a problem, by iterating in time to an equilibrium. More terms can be included to attempt to find a more accurate solution.

Recently, Aschwanden (2013b) has aimed to build new NLFFF models where the 3D magnetograph information for the photosphere is not necessary, through using the 2D magnetogram and observed coronal loops. At the cost of accuracy, a temporal resolution of 45 seconds can be obtained, and the model can be computed much more rapidly in this way than by methods which use 3D magnetic field data.

3.3.4 Aschwanden's Code: An Outline

In this research, codes based on Aschwanden's forward-fitting NLFFF codes are used as a starting point, with many modifications and extensions added to model the magnetic field in the chromosphere and the corona. Specifically, this work is extended to discover changes in the structure and energy of the system with a temporal cadence of 45 seconds, and also to build 3-dimensional multi-wavelength images of coronal loops. The machinery of the original codes is outlined in a 3-part series by Aschwanden and Malanushenko (Aschwanden (2013b), Aschwanden & Malanushenko (2013), Aschwanden (2013c)).

The codes begin by decomposing a 2D magnetogram into a set of point charges, in order to roughly estimate the 3D magnetic field in the photosphere. Each of these point charges has a 3-dimensional location, a magnetic field strength and a value of α, and these are set to provide the optimal possible representation of the data contained in the 2D magnetogram. After this step, the location and strength of each point charge are known, but α is still unknown for each. However, α can be estimated by comparing AIA observations at the footpoints of the coronal loops with the potential field model for the set of point charges: the average angle between the observed loops and the potential field simulation in the immediate environs of each point charge yields an estimate of α in the vicinity of each point charge.

The five parameters can now be used as boundary conditions at the base of the chromosphere to extrapolate magnetic field lines which extend into the chromosphere and corona. The extrapolation is performed in small steps, accounting for spatial changes in the distribution of α and the magnetic field. The extrapolated magnetic field lines can then be readily compared (in 2D) with observed coronal loops. These can be followed and traced in two dimensions using the procedures outlined by Aschwanden (2013a)

Magnetic field strength (G)	X co-ordinate (Solar radii)	Y co-ordinate (Solar radii)	Z co-ordinate (Solar radii)	α
1000	-0.10	-0.10	0.90	-5
-1000	-0.05	0.10	0.90	-5
1000	0.05	-0.05	0.90	-4
-1000	0.10	0.00	0.90	-4

Table 3.1: Non-potential magnetic field parameters for Figure 3.2

3.3.5 Effectiveness of the method

Like any other method, the effectiveness of this method at modeling test cases must be determined. This is achieved by creating theoretical magnetic fields in terms of point charges in the photosphere where the values of α in the vicinity of each point charge are known. Then the above method is used to extrapolate the magnetic field into the chromosphere, using the distributions of the magnetic field and α provided by the simulation. Through comparing this with the corresponding potential field model, and noting the angle formed between field lines of the two models in the vicinity of the point charges, α can be determined (again) in the vicinity of the point charges. The efficacy of the method can then be determined by comparing the calculated values of α with the original values of α. The configuration of the magnetic field can also be re-drawn using the new values of α, and compared with the original.

Figure 3.2 simulates a complicated situation with four point charges. Their magnetic field strengths and locations, as well as the known values of α are noted in Table 3.1.

The values calculated for α through use of this method to determine the magnetic field are -4.54, -5.45, -4.68, -3.62 respectively, which are close to the starting values in table 3.1. Figure 3.2 shows that the calculated magnetic field lines also agree well with the theoretical non-potential magnetic field, with the field lines showing the same configuration.

3.4 Method

3.4.1 Using real data

One advantage to using the data observed by the AIA telescope is that the images are available in several different wavelengths, in particular 94Å, 131Å, 171Å, 193Å, 211Å, 304Å and 335Å. The different wavelengths focus on plasmas of different temperatures: the 94Å wavelength focuses on plasma of about 6.3MK; the 131Å wavelength focuses on 0.4MK, 10MK and 16MK; the 171Å wavelength on 0.63MK; the 193Å wavelength on

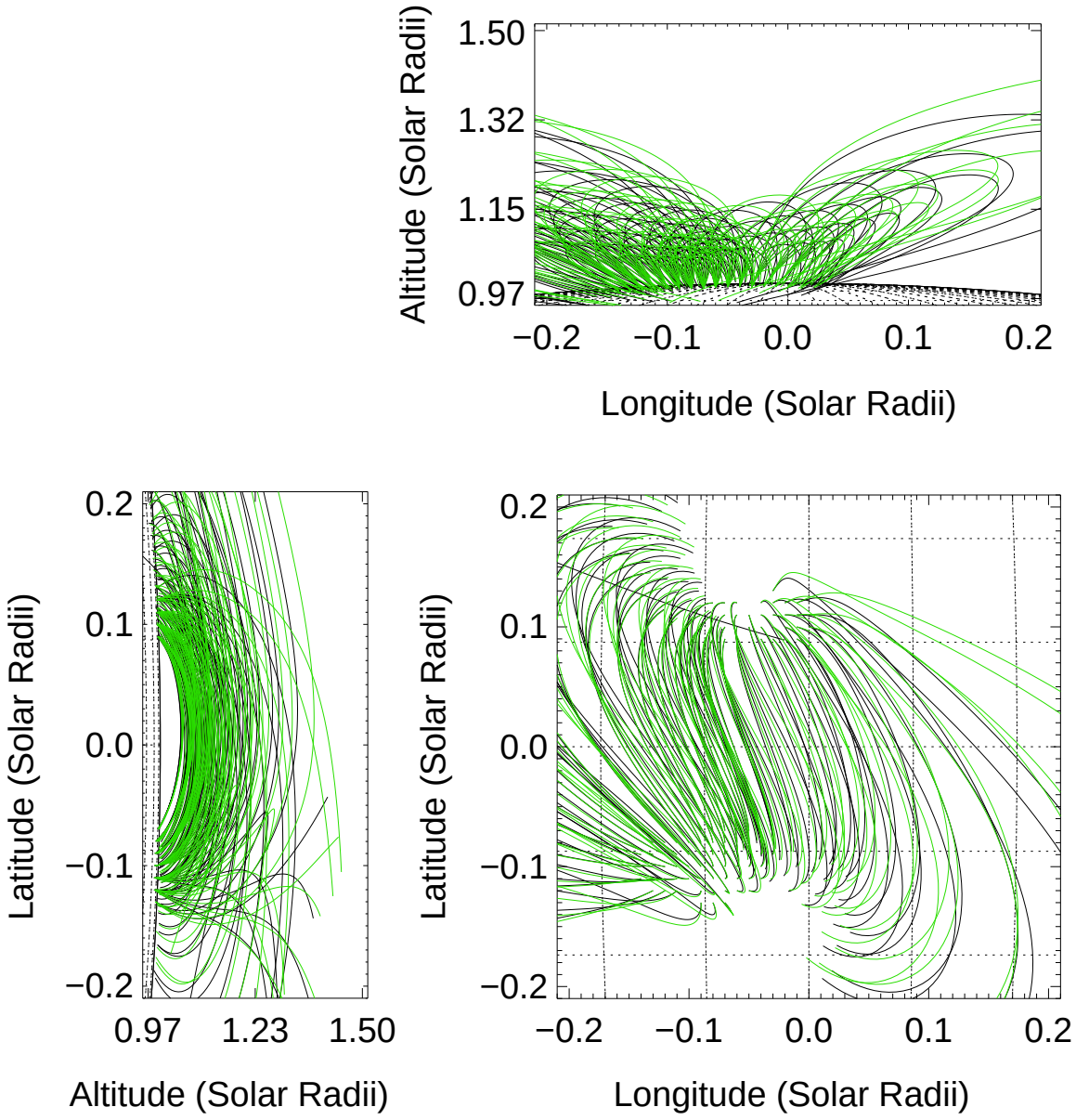

Figure 3.2: Original magnetic field (black) and the new (calculated from the original field lines) magnetic field (green) for four point charges, from 3 orthogonal directions.

1.2MK and 20MK; the 211Å wavelength on 2MK; the 304Å wavelength on 0.05MK and the 335Å wavelength on 2.5MK. In general, when observing coronal loops, geometric differences can be seen between the images in different wavelengths, and the loops appear to meet the photosphere at different angles in the different wavelengths. Considering that the aim is to use the angle between the local magnetic field and the loop footprints near the photosphere to estimate α, it is clear that the different wavelengths will yield different values for α in the vicinity of the point charges.

Two strategies arise to profit from this. Firstly, and especially when computing the free energy, considering the loops of all wavelengths together is a good use of the data, and one which will reduce the negative influence of misleading data. Secondly, the disagreement between the different wavelengths can be considered to be an advantage, by using different wavelengths to create up to seven different models of the same area. By drawing these in different colors, it is possible to compare how the magnetic field affects the temperature distribution of the plasma. Each of the colors would represent how the magnetic field configuration would be expected to appear in a particular wavelength in 3D.

3.4.2 Calculating the Free Energy

One of the most important elements of any solar structure is the free energy. It has already been noted that the potential field model does not contain free energy. The potential field is the configuration with the lowest possible energy, denoted by E_p. However, in general the energy belonging to any solar configuration is greater than E_p, and this is because of the twist which stores some energy.

The energy in a real configuration, the non-potential energy, is denoted by E_{np}. If the configuration changes - and it is clear from observations that most structures reconfigure over time and therefore the non-potential energy will change. These kinds of change can occur due to magnetic reconnection or coronal mass ejections. The free energy - the difference between the non-potential field energy and the potential field energy - is denoted by E_f and

$$E_f = E_{np} - E_p$$

This is the maximum energy that any structure can eject, before reverting to the potential field. Although observations suggest that it is not common for a structure to lose its entire free energy at once, estimation of how much energy could escape in the course of a coronal mass ejection is important for solar weather prediction. Consider a magnetic field in the chromosphere and corona which exhibits twist. α is non-zero.

Consider further the components of the non-potential magnetic field $\boldsymbol{B}$ in the chromosphere and corona such that one component is parallel to the potential field $\boldsymbol{B}_{\parallel}$, and the other is perpendicular to the potential field, $\boldsymbol{B}_{\perp}$. In vector form:

$$\boldsymbol{B}_{np} = \boldsymbol{B}_{\perp} + \boldsymbol{B}_{\parallel}.$$

By definition, $\boldsymbol{B}_{p} = \boldsymbol{B}_{\parallel}$.

The energy of a structure is given by:

$$E = \frac{1}{2\mu_o} \int \boldsymbol{B} \cdot \boldsymbol{B} dV = \frac{1}{2\mu_0} \int B^2 dV$$

where V denotes the volume under consideration, E denotes the energy and B denotes the magnetic field. The free energy can therefore be calculated by:

$$E_{np} - E_p = \frac{1}{2\mu_0}(\int \boldsymbol{B}_{np}^2 dV - \int \boldsymbol{B}_{p}^2 dV)$$

By considering the perpendicular and parallel components to the magnetic field, it can be shown that:

$$E_f = \frac{1}{2\mu_0} \int ((\boldsymbol{B}_{\parallel} + \boldsymbol{B}_{\perp})^2 - \boldsymbol{B}_{\parallel}^2) dV = \frac{1}{2\mu_0} \int (\boldsymbol{B}_{\parallel}^2 + 2\boldsymbol{B}_{\parallel} \cdot \boldsymbol{B}_{\perp} + \boldsymbol{B}_{\perp}^2 - \boldsymbol{B}_{\parallel}^2) dV$$

Noting that $\boldsymbol{B}_{\perp}$ a $\boldsymbol{B}_{\parallel}$ are mutually perpendicular:

$$E_f = \frac{1}{2\mu_0} \int \boldsymbol{B}_{\perp}^2 dV$$

Hence, the free energy is dependent only on the perpendicular component $B_{\perp}$.

To calculate the free energy, a 3-dimensional grid is considered, as mentioned previously, which extends from the photosphere and contains areas of the chromosphere and corona, and integration is performed throughout the grid to calculate the sum of the free energy. The height of the grid must be curtailed, since the force-free condition breaks down far above the photosphere; 1.15 solar radii is a sensible constraint. In this process, the magnetic field is assumed to be constant in each grid cell and the value of α is calculated in each cell. The potential energy and non-potential energy are also computed.

Since the observational data from the magnetograms and AIA images is available every 45 seconds, the model can hence be used to compute the free energy every 45 seconds and to study changes in the free energy.

3.5 Example: 08:00-09:00, 2011-11-11

A system of coronal loops was observed in the south east of the Sun on the morning of 2011-11-11. The AIA data (Animation 3, in the 171Å wavelength between 08:00 and 09:00 on 2011-11-11) suggests that the system exhibits at least one coronal mass ejection, with associated magnetic reconnection. By modeling this system with a temporal cadence of 45 seconds, more can be learned about the dynamics and energy of the system. Animation 3 also suggests flows along the coronal loops, which whilst important in its own right is unfortunately outside the scope of this work.

3.5.1 Parameters

The magnetic field in the photosphere was estimated by 50 point charges. Although it is not possible to consider the immense complexity of an entire magnetic field with only a few point charges, it is held to be a fair simplification of the situation. The grid extends across a space which is 0.2 solar radii in latitude, 0.2 solar radii in longitude and 0.15 solar radii in altitude. The spatial resolution is 0.001 solar radii. This provides a network of cells of $200 \times 200 \times 150 =$ six million cells. The spatial resolution allows both the magnetic field and α to vary spatially in the corona. α is discovered in the vicinity of the point charges by the methods previously outlined.

3.5.2 Modeling the magnetic field

By using each of the 7 main wavelengths, a model can be built of the magnetic field in the chromosphere and corona by assuming that the loops all follow the magnetic field lines in the chromosphere and corona. Usually, approximately 250 loops are used to estimate α in the vicinity of the point charges. The more loops are considered, the more believable the approximation appears to be. Figure 3.3 shows the magnetic field at 08:40:30 on 2011-11-11 from 3 orthogonal directions, as well as a co-temporal AIA image in the 171Å wavelength, for comparison. The magnetic field lines in the longitude-latitude graph appear to correspond well to the AIA observations, especially at the footpoints of the loops in the top left corner of the 2 panels. A careful examination of the panels yields field lines in the top right of the lower left panel which correspond to the loops observed in the top left of the AIA panel in terms of layout and shape. This model, despite any

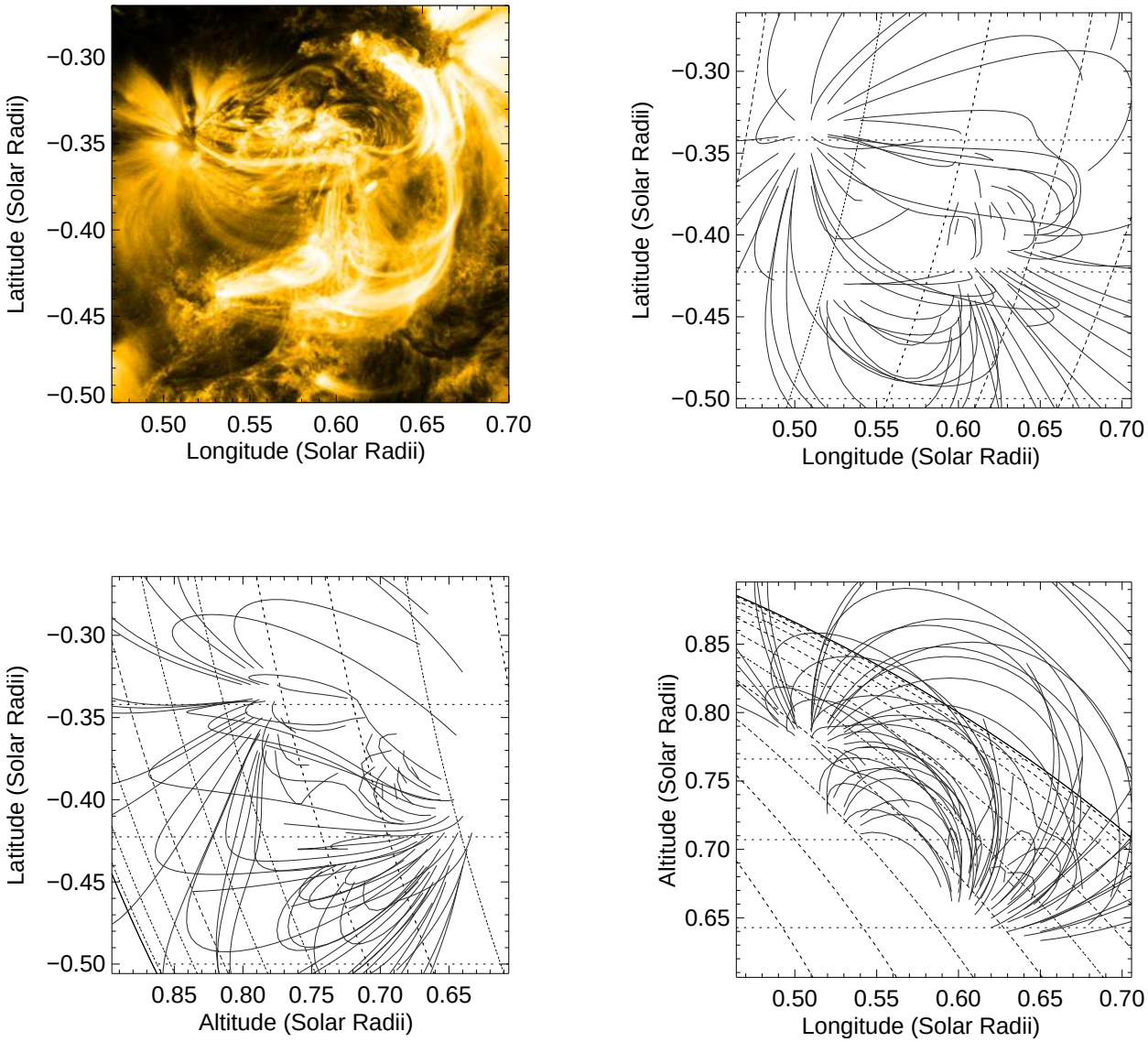

Figure 3.3: AIA 171Å observations (top left panel) and the modeled magnetic field (other panels) at 08:40:30, 2011-11-11.

differences, is much more useful than AIA observations alone for estimating the height of different loops. The other two panels simulate observations in terms of height, the third dimension which is absent from AIA observations. Many loops seen in the model, particularly those mid-range in terms of latitude and longitude, were presumably either too small or too low in altitude to be seen clearly from the AIA observations.

3.5.3 Modeling with different wavelengths

The loops observed in different wavelengths are used to estimate the parameter α. This is achieved by considering each wavelength separately, and values for α at the loop footprints are obtained for each of the different wavelengths, thus allowing the construction of different configurations of the magnetic field in three dimensions in the corona for each wavelength. Remembering that each of the wavelengths represents plasma of a particular temperature (or several temperatures), this allows an analysis of the distribution of plasmas of different temperatures. By considering changes in the configurations over time, it is possible to study the dynamics of the plasma configurations. A major disadvantage of this method of studying each wavelength separately is that the number of loops available from the data, used to estimate the value of α in various locations, is comparatively small. If all wavelengths are considered together, the number of loops is significantly greater, but then the information about the configuration of plasmas of different temperatures would be lost. When considering the different wavelengths separately, the small number of loops can at times lead to the construction of rather strange magnetic field configurations by yielding an unbelievably high or low value for α. This is perhaps not entirely unexpected, when attempting to obtain α values for 50 point charges using the footprints of less than 40 loops each time; however I have included upper limits in the optimization algorithm which calculates the distribution of α in an attempt to reduce the influence of bad estimates of α.

Despite this problem, an example of the power of this technique can be seen in Figure 3.4 where the configuration of the magnetic field in an area is denoted with green representing the 94Å wavelength, light blue representing the 131Å wavelength, yellow representing the 171Å wavelength, brown representing the 193Å wavelength, purple representing the 211Å wavelength, red representing the 304Å wavelength and dark blue representing the 335Å wavelength. It is clear that the lower latitudes are dominated by the 131Å wavelength, suggesting that the plasma at lower latitudes is significantly hotter than much of the rest of the plasma.

The striking differences between figures 3.3 and 3.4 can be partially explained by the different techniques used (all wavelengths together vs each wavelength separately), and partially by large variations in the values

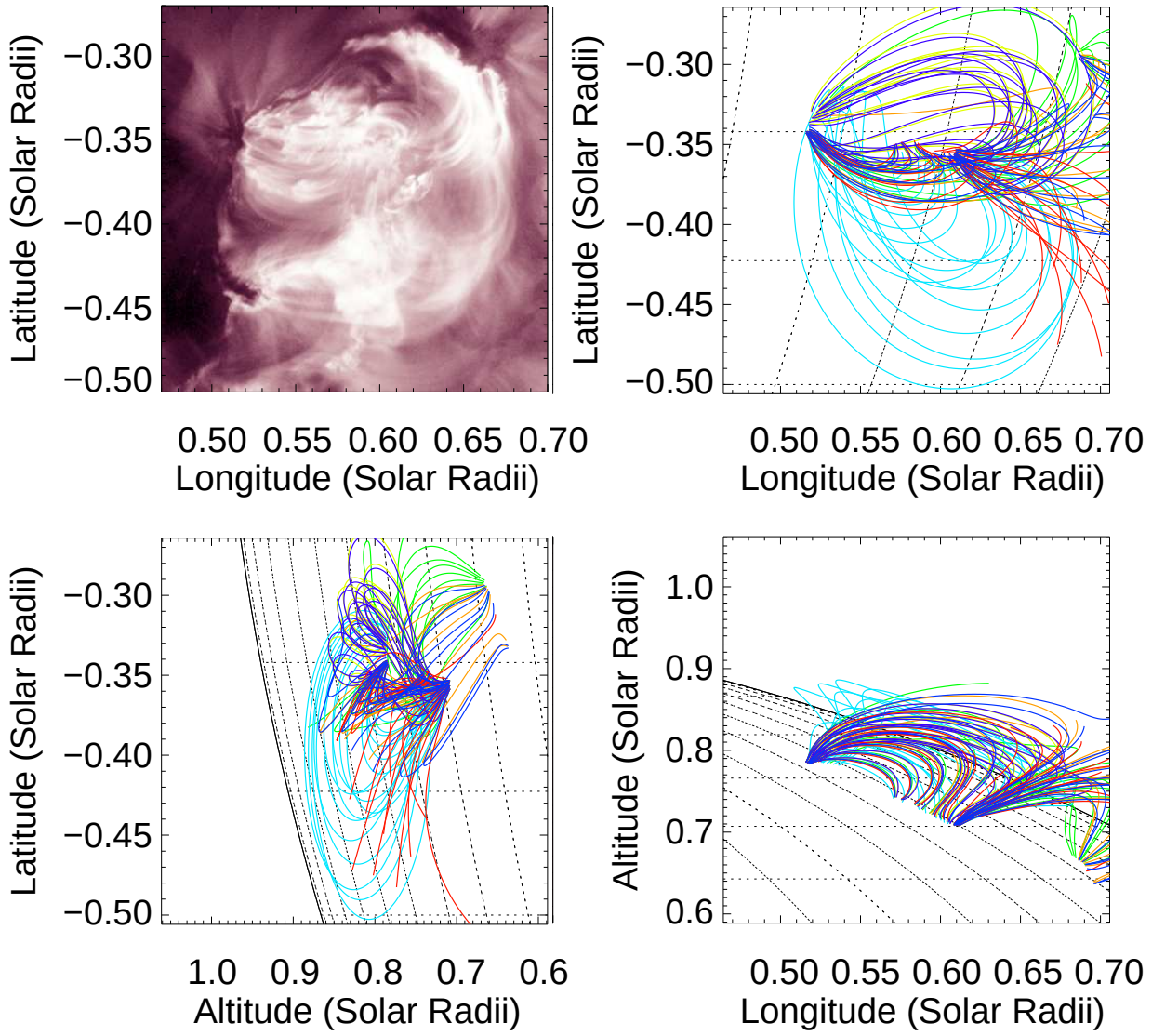

Figure 3.4: AIA observations (top-left panel) and the magnetic field, as modeled at 08:44:15 on 2011-11-11. The plasma at low latitudes is observed to correspond to temperatures observed by the 131Å wavelength (light blue). The different axes to Figure 3.3 reflect differences in the geometry of the extrapolated loops. Green denotes the 94Å wavelength, light blue denotes the 131Å wavelength, yellow denotes the 171Å wavelength, brown denotes the 193Å wavelength, purple denotes the 211Å wavelength, red denotes the 304Å wavelength and dark blue denotes the 335Å wavelength.

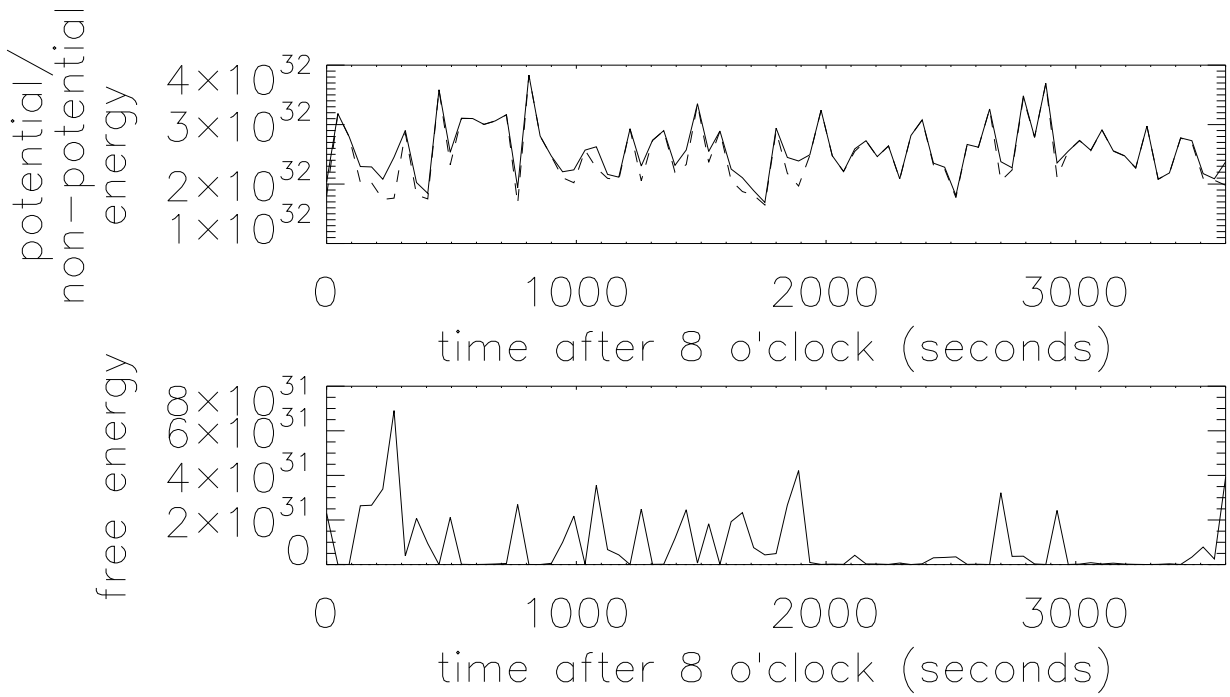

Figure 3.5: The different energies (units: erg), modeled over the period of one hour. The top graph shows changes in the potential energy (dashed line) and the non-potential energy (solid line). The lower graph shows changes in the free energy. All three measures of energy appear to vary greatly over the course of an hour in this model, with many sharp peaks and troughs. However, one of the sharp decreases in potential energy corresponds temporally to an observed partial eruption.

of alpha which will be discussed later.

3.5.4 The free energy and its relation to observations

Figure 3.5 shows the potential energy (top panel, dashed line), the non-potential energy (top panel, continuous line) and the free energy (lower panel) calculated from the models with 45 seconds cadence.

The energy estimated by the models varies significantly more than would be expected, in particular the potential energy which would be expected to remain roughly constant. This may be a result of the assumptions made (such as the representation of a complex magnetic field by compartively few point charges), however several interesting features can be seen. For example, at about quarter to 9 (2700 seconds), the free energy was seen to decrease from 3.22×10^{31} erg to 3.68×10^{30} erg. The AIA observations for this time clearly show that one of the loops appeared to open up, causing an eruption and magnetic reconnection within the structure, causing the configuration to change. With our estimates for the free energy before and after the eruption, the free energy released can be estimated as approximately 2.85×10^{31} erg. However, observations

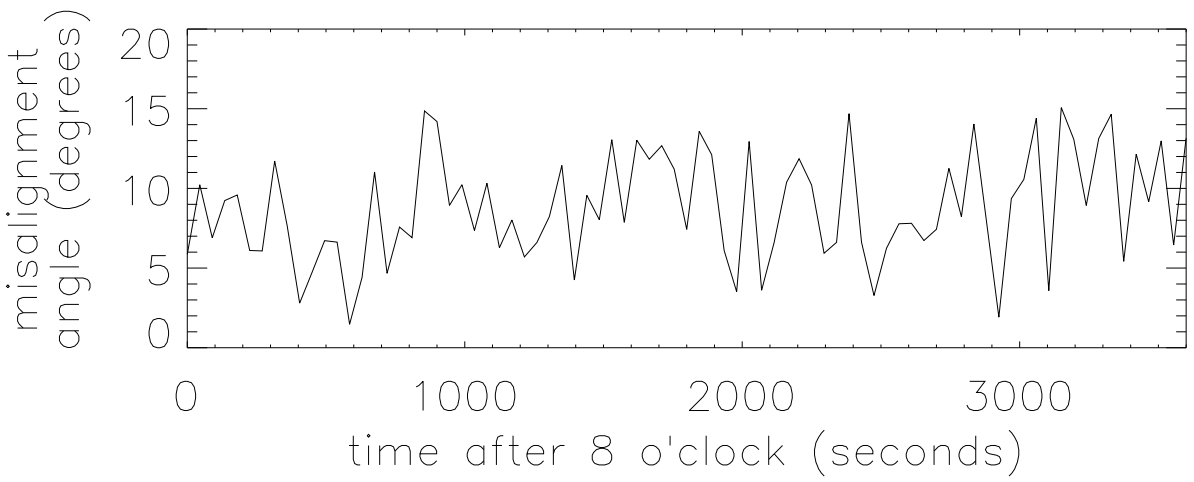

Figure 3.6: The average misalignment angle as a function of time over one hour. The misalignment angle varies greatly, but remains quite low at all times, suggesting a degree of accuracy

did not provide clear indications of other events corresponding to other major decreases in the free energy which can be seen in Figure 3.5. Other peaks have no clear links to any visible events in the AIA animation.

3.6 Discussion

It is clear that these methods can aid understanding of coronal loops. They can be used to estimate the free energy which can be lost through eruptions such as the example at about quarter to 9. One way of assessing the accuracy of an NLFFF model is to consider the misalignment between simulated magnetic field and the observed loops. The misalignment can be measured by considering the angles between the simulated and observed loops on the surface of the photosphere. The value of the angle is calculated on average throughout a particular pair of images - the observed 2D AIA image vs a 2D representation of the model from the same viewing angle as the AIA. Naturally, the value of the average angle changes with time, and the average misalignment angle for the example previously considered is shown as a function of time in Figure 3.6. An average of the misalignment angle over the time interval of one hour, that is the average of the angles in Figure 3.6 can be measured, and a value of 8.78 deg is obtained. It is also clear from Figure 3.6 that the misalignment angle never exceeded 17 deg. This suggests that none of the modelled scenarios differs dramatically from the AIA observations at that time, overall; the approximation is fairly close, although there is of course a need for significant improvement in later development of such models.

The efficacy of the method can be further assessed by a more detailed study of the point charges and their associated properties, and how these change over time. The decomposition of a 2D magnetogram to a

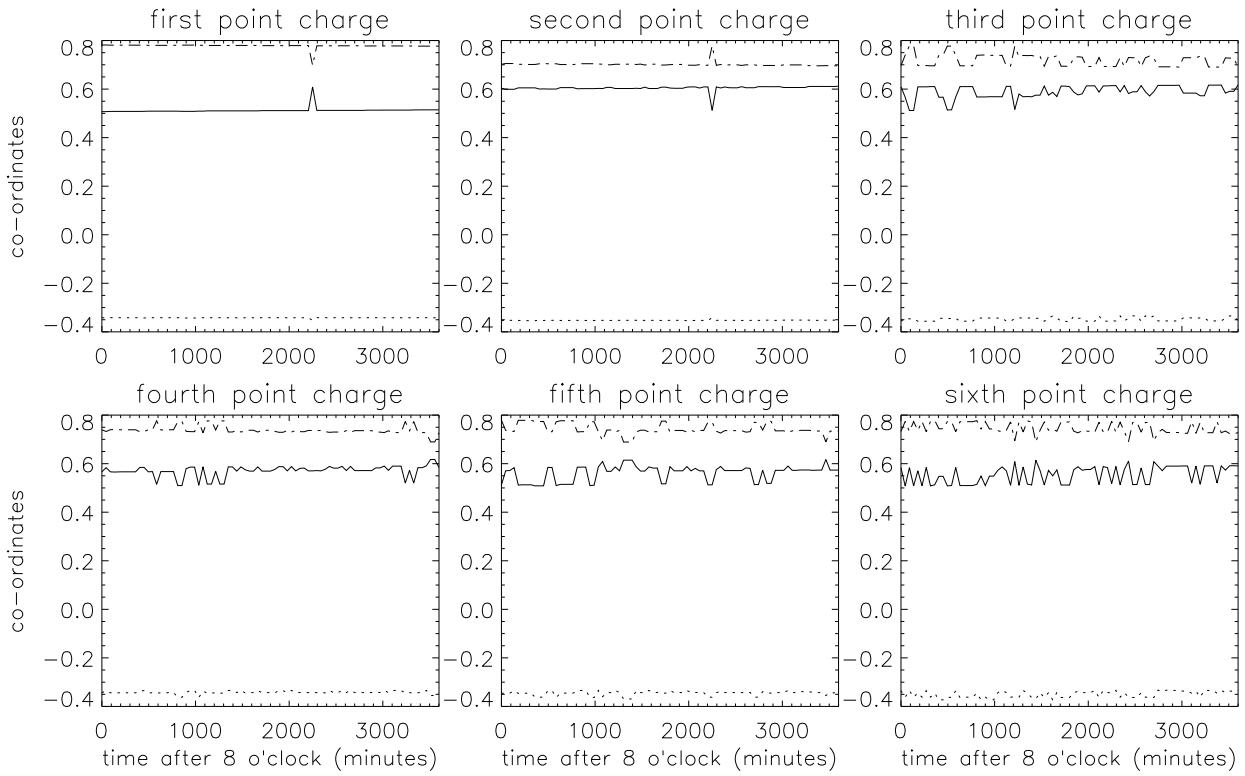

Figure 3.7: Co-ordinates of the six strongest point charges over one hour. The locations of the strongest point charges are almost entirely constant. The dashed line represents altitude; the dotted line represents latitude while the solid line represents longitude.

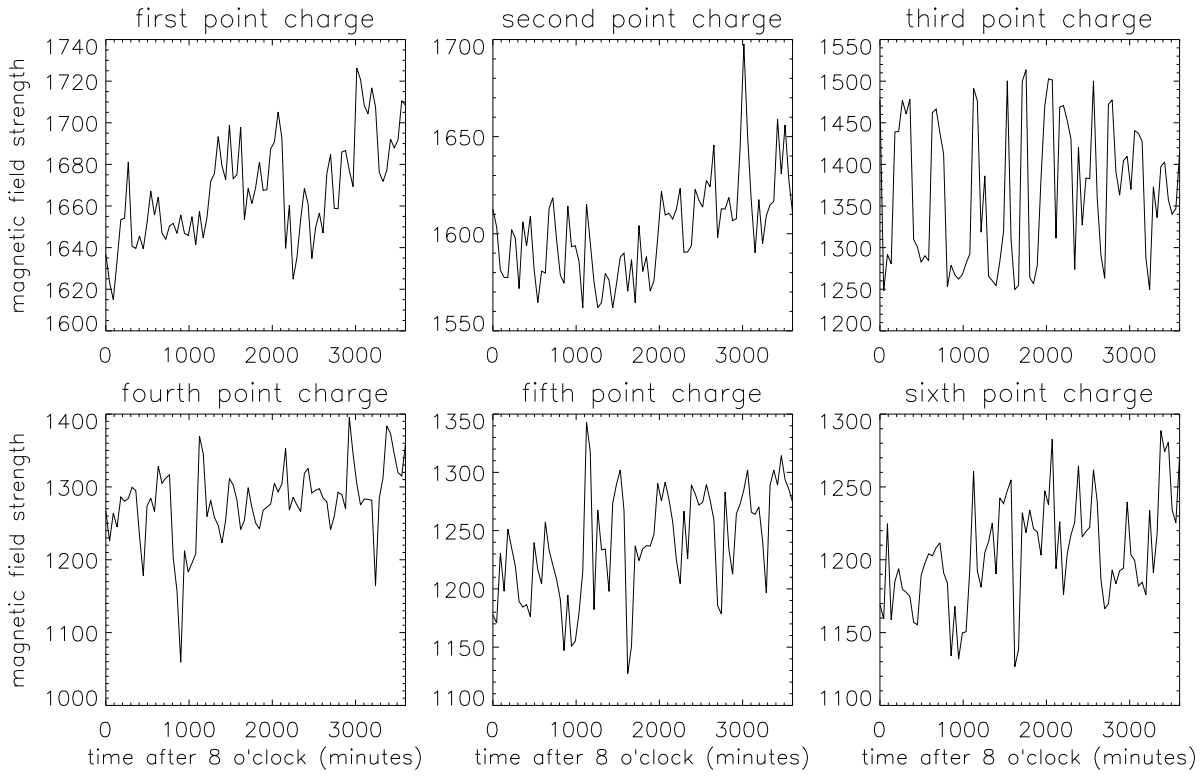

Figure 3.8: Changes in the magnetic field strength (units: Gauss) of the six strongest point charges over one hour. The magnetic field strength varies greatly.

relatively small number of point charges was key to the method. In Figures 3.7 and 3.8, changes in the magnetic field strengths and co-ordinates of six point charges are shown, with the strongest point charge in the first panel and the weakest in the last panel. Naturally, it is possible that the order of the point charges may change over time - the strongest point charge at 08:00 may not be the strongest point charge at 09:00 for instance- and therefore sudden sharp changes in the coordinates are expected. In Figure 3.7, the x co-ordinate is denoted by the dotted line, the y co-ordinate by the continuous line and the z co-ordinate by the dashed line.

The point charges stay in more or less the same place throughout time, which suggests consistency in the locations where the magnetic field is particularly strong. Where changes occur, these can be explained in terms of change in the order of the charges in the panels due to the magnetic field strength changing. However, Figure 3.8 shows that significant changes occurred in the magnetic field strength of the point charges over the hour, which suggests that the situation is not consistent with expectations for a generally quiet situation. More than six point charges were also considered to investigate whether this would yield a more consistent magnetic field strength, but the result was largely the same as for six point charges.

Figure 3.9 shows changes in the values calculated for α for the six strongest point charges over one hour. Some panels show that α changes from being large and positive to being large and negative (or vica versa) over 45 seconds - which is the temporal resolution of the model - which was unexpected. The conclusion is therefore reached that although the methods in this chapter can be useful to explain the dynamics of solar structures, care must be taken in analyzing the results.

3.7 Conclusion

The methods discussed in this chapter succeeded in creating three-dimensional images of coronal loops, in a range of different wavelengths, something which cannot be done with AIA observations alone. When images of this type are seen in two dimensions, of the same orientation as the AIA images, they correspond well to the AIA images, and they can be used to estimate the height of different loops, something which is currently impossible with 2D AIA images. The method also allows loops of lower height to be modeled: these are often invisible on the AIA images due to higher loops blocking them from view. Hence the method allows a fuller appreciation of the full coronal loop systems to be found in the solar atmosphere. The method also provides information about the distribution of plasma at different temperatures by analyzing AIA images of different wavelengths separately, although it must be noted that the multi-wavelength method is not entirely reliable due to the lack of sufficient data. The method where all wavelengths were considered together provided a

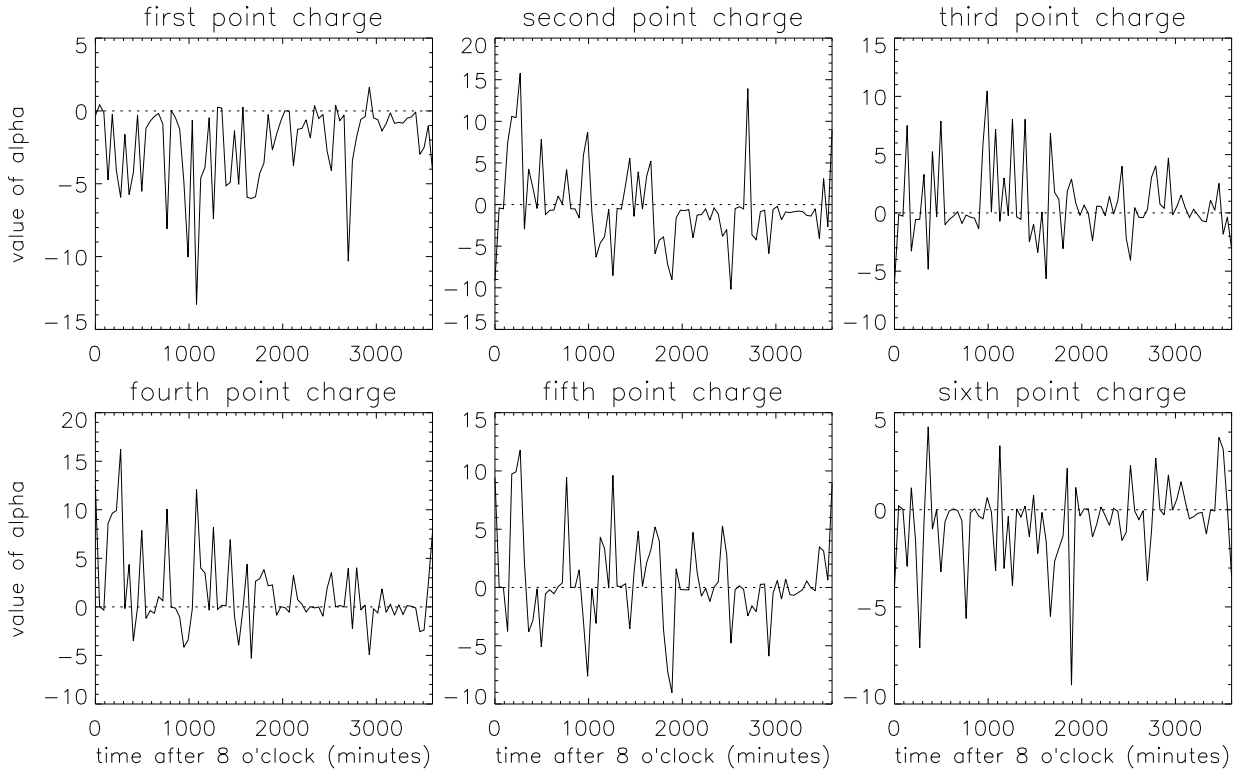

Figure 3.9: Changes in the value of α for each of the six strongest point charges over one hour. The value of alpha varies greatly, frequently varying between positive and negative, suggesting a change in direction of 'twist'.

rough idea of the energies which were contained within the structures as well as the changes which occurred over time. In particular, a major reduction in free energy is seen to correspond to an eruption, and the amount of free energy released in the eruption was estimated. Although the method is clearly not entirely reliable in estimating changes in the free energy, especially considering the dramatic changes in the potential energy over time, it suggests that new methods of this type could be very useful in the future, allowing models with a temporal resolution of 45 seconds. Therefore this research is best considered as a stepping stone to more accurate multi-wavelength modeling with a 45s cadence, rather than an entirely reliable method in its own right at this juncture; however it has already provided interesting information and findings about a real data-set.

Bibliography

Aschwanden, M. J. 2013, The AstroPhysical Journal, 763, 115

Aschwanden, M. J. 2013, Solar Physics, 287, 323

Aschwanden, M. J., & Malanushenko, A. 2013, Solar Physics, 287, 345

Aschwanden, M. J. 2013, Solar Physics, 287, 369

Chiueh, T., & Zweibel, E. G. 1989, The AstroPhysical Journal, 338, 1158

Chodura, R., & Schlüter, A. 1981, Journal of Computational Physics, 41, 68-88

Grad, H., & Rubin, H. 1958, Peaceful Uses of Atomic Energy, 31, 190

Guo, Y., Ding, M. D., Liu, Y., et al. 2012, The AstroPhysical Journal, 760, 47

Jiang, C., & Feng, X. 2013, The AstroPhysical Journal, 769, 144

Kliem, B., Su, Y. N., van Ballegooijen, A. A., & DeLuca, E. E. 2013, The AstroPhysical Journal, 779, 129

Liu, S., Zhang, H. Q., & Su, J. T. 2012, AstroPhysics and Space Science, 337, 665

Low, B. C., & Lou, Y. Q. 1990, The AstroPhysical Journal, 352, 343

Mackay, D. H., & van Ballegooijen, A. A. 2009, Solar Physics, 260, 321

Malanushenko, A., Schrijver, C. J., DeRosa, M. L., Wheatland, M. S., & Gilchrist, S. A. 2012, The AstroPhysical Journal, 756, 153

Nakagawa, Y. 1974, The AstroPhysical Journal, 190, 437

Powell, M. J. D. 1964, The Computer Journal, 7 (2), 155

Su, Y., van Ballegooijen, A., Lites, B. W., et al. 2009, The AstroPhysical Journal, 691, 105

Tadesse, T., Wiegelmann, T., MacNeice, P. J., et al. 2014, Solar Physics, 289, 831

Wheatland, M. S. 2006, Solar Physics, 238, 29

Wiegelmann, T. 2004, Solar Physics, 219, 87

Wiegelmann, T., & Sakurai, T. 2012, Living Reviews in Solar Physics, 9, 317-65

Chapter 4

Wave Trains in a Solar Filament

4.1 Preface

Two extremely fast features were observed in EUV wavelengths, emerging from a region of strong magnetic flux and traveling along a solar filament channel with speeds in the order of 1900km s^{-1}, which is interpreted as fast magnetosonic wave trains. The energy transfer caused by these phenomena appears to produce many slow magnetosonic waves, at least one of which is seen to accelerate significantly whilst traveling along the filament channel. Such acceleration precludes a mass flow, and therefore these are also interpreted as waves. I suggest that the bright blobs often interpreted as mass flows in solar filaments may in fact be waves. The region where the fast magnetosonic waves are produced is shown to experience significant drops in magnetic flux co-temporal with the production of waves, and I therefore speculate that this phenomenon may be caused by magnetic activity.

4.2 Introduction

Solar filaments appear as long, raised horizontal structures following the polarity inversion line, with barbs connecting the main structure to the photosphere. When viewed above the solar limb, they are called prominences, see reviews (Martin (1998), Mackay et al. (2010)). Upon closer examination, these are found to be composed of a multitude of threads, which appear to carry plasma (Lin et al., 2008). Filaments appear to be restless with counter-streaming flows in the order of 10km s^{-1} when observed in Hα (Zirker et al. (1998), Deng et al. (2002), Lin et al. (2003), Schmieder et al. (2008) and review paper Mackay et

al. (2010)). Much faster bright blobs moving along filament threads have also been observed, for instance using Hα images from the 1m Swedish Solar Telescope on La Palma, van Noort & Rouppe van der Voort (2006) observed chromospheric bright blobs traveling at up to 240km s^{-1} along threads and Lin et al. (2012) observed such blobs traveling at $45-111$km s^{-1}, suggesting that this could be caused by an MHD fast-mode pulse. Deng et al. (2002) suggested that these may correlate to a sudden decrease in magnetic flux at their origin.

Dynamic motions have also been routinely observed in Extreme Ultra-Violet wavelengths especially when filaments/prominences are known to produce emission at temperatures to about $\log T(\mathrm{K}) \approx 5.5$ and show motions of up to 70km s^{-1} (Wang (1999), Chae et al. (2000), Kucera et al. (2003), Kucera & Landi (2006)). Further, upward-moving jets have been cited as a mechanism for injecting mass into prominences Chae et al. (2000) or the surrounding coronal cavities Li et al. (2012). Several wave explanations have been proposed as a cause of jets in solar filaments, for instance Moreton Waves or EIT waves ((Eto et al., 2002), (Okamoto et al., 2004), (Gilbert et al., 2008)). Jets and subflares in close proximity to the filament have also been cited (Jing et al. (2003), Jing et al. (2006), Vršnak et al. (2007)). Another aspect of the observed jets is the apparent connection with the eruption, or prelude to eruption, of the filament (Tripathi et al. (2006), Isobe & Tripathi (2006), Isobe et al. (2007), Chen et al. (2008)). Some apparent dynamic motions might also be interpreted as slow magnetosonic waves (Liu et al., 2012). Alexander et al. (2013) observed flows in the order of 100km s^{-1} with the Hi-C telescope, which had extremely high temporal and spatial cadence.

In the different outer layers of the Sun, both fast and slow propagating magnetosonic waves have been widely observed in different parts of the solar atmosphere with slow magnetosonic waves more frequently observed (see review by Nakariakov & Verwichte (2005)). Several types of large-scale wave have been proposed as the possible cause of jets observed in solar filaments. More recently, new observations of fast propagating magnetosonic waves (or wave trains) have been available thanks to Solar Dynamic Observatory. Liu et al. (2011) observed waves as fast as 2200km s^{-1} which were produced by a coronal mass ejection. Liu et al. (2012) observed waves as fast as 1420km s^{-1} producing wave trains, some of which appeared to be significantly slower than the original wave. Shen et al. (2013) observed wave trains with speeds of 689km s^{-1} decelerating to 343km s^{-1}with a period of 80 seconds. Hershaw et al. (2011) observed two wave trains causing large-scale longitudinal oscillations in a solar filament. Li et al. (2012) observed a large scale fast EUV wave producing a series of slower waves, the waves propagate at between $430-780$km s^{-1}, along with significant acceleration and decelerations, and bifurcations. Intriguingly, when the wave hit a bright region of the corona it induced another wave there with double the speed. These large scale waves have been interpreted as fast magnetosonic waves. Fast magnetosonic waves in the solar atmosphere have also been

studied and reported by Nakariakov et al. (2004), Jelinek & Karlicky (2010), Pascoe et al. (2013), Yang et al. (2013), Yuan et al. (2013) and others.

This work reports a unique observation of very fast moving features (~ 2000 km s^{-1}) along a narrow filament channel and slower moving features associated with the fast ones. It goes on to interpret the fast moving features as propagating fast magnetosonic waves and the slower ones as slow magnetosonic waves.

4.3 Instrumentation and Techniques

This research uses data from the Solar Dynamics Observatory (SDO), which provides full-disk images of the sun with an unprecedented spatial and temporal cadence. The Atmospheric Imaging Apparatus (AIA) provides EUV images in 7 main wavelengths every 12 seconds, in sub-arcsecond resolution (lemen2012).

Figure 4.1 shows the location of the filament studied. The filament is U-shaped, sinistral (appears to bear left when viewed from the positive side of the polarity inversion line) and of length in the order of 500×10^3km and can be observed for several days around 2012-08-06. It is located in the southern hemisphere. Its western and eastern ends are rooted in regions of strong magnetic flux and there appear to be two other areas of strong magnetic flux which interact with the filament. HMI magnetogram data suggests that the filament follows the polarity inversion line, and that the PIL is interspersed with several areas of strong magnetic flux. Movies composed of a series of AIA images show that the filament is composed of a series of clearly defined, widely dispersed threads, carrying plasma, with bright blobs observed apparently traveling along the threads. The bright blobs appear to move through the flux tubes between the regions of strong magnetic flux, and are observed to travel in both directions simultaneously (in different tubes) along the length of the filament. A partial eruption is observed at around 14:00 on 2012-08-06, however the filament continues to exist for a long time after this.

One interesting aspect of the filament, observed between 08:20 and 08:40 on 2012-08-07, is the production of fast bright blobs at the eastern end of the filament, which appear to proceed along a flux tube, accelerating and decelerating, until colliding with another location on the filament, at which point no further progress of the blobs was visible.

The trajectory of the blob with respect to an AIA image is represented by a series of straight lines. To ensure the inclusion of the entire trajectory, a path 7 pixels wide is considered, centered around my approximation of the blob's trajectory, as shown by the red dotted lines in Figure 4.2. This approximation of the blob's trajectory is of course highly subjective, however this was the only means available of tracking it. Along the

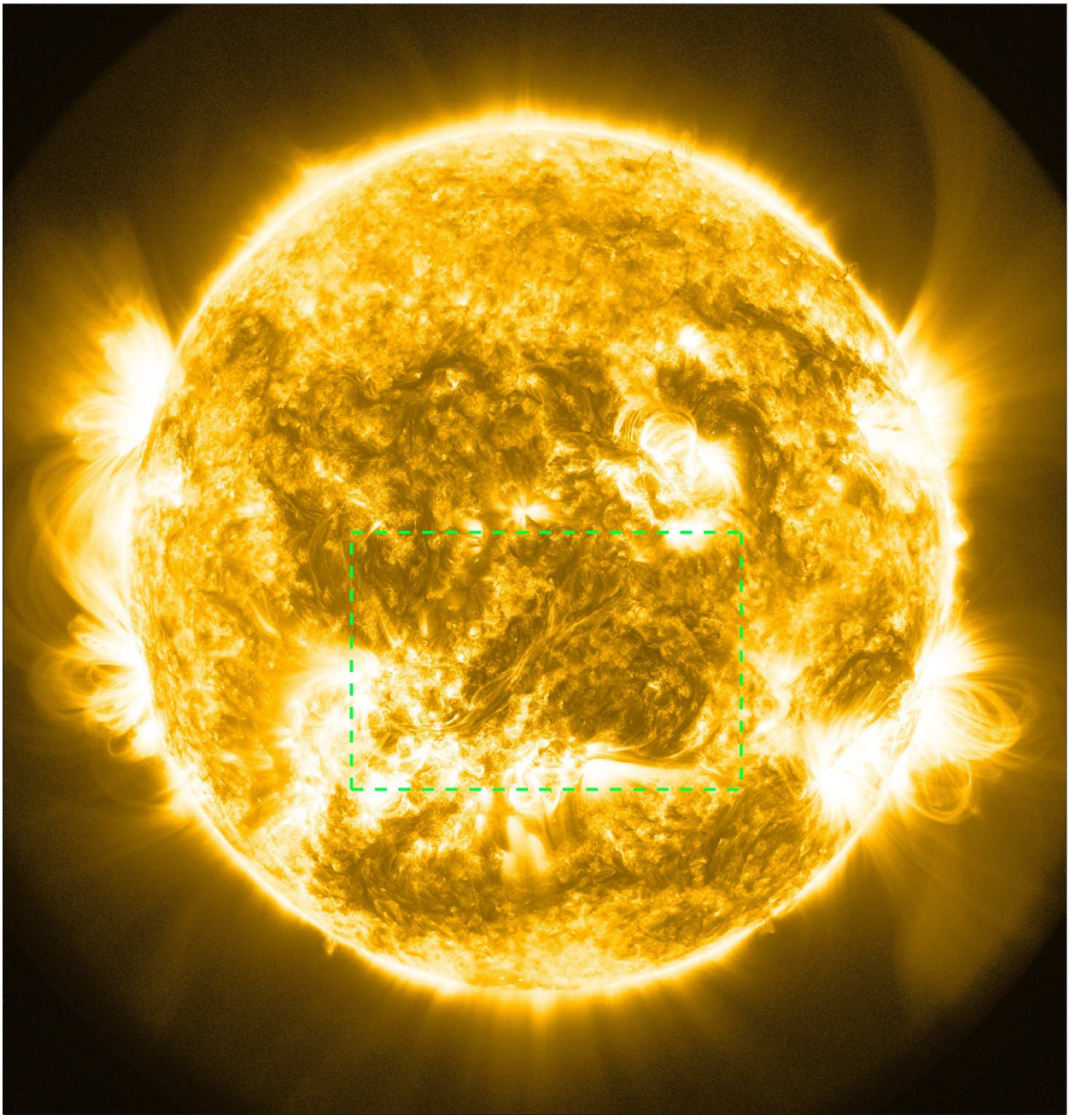

Figure 4.1: Location of the filament on the solar disc.

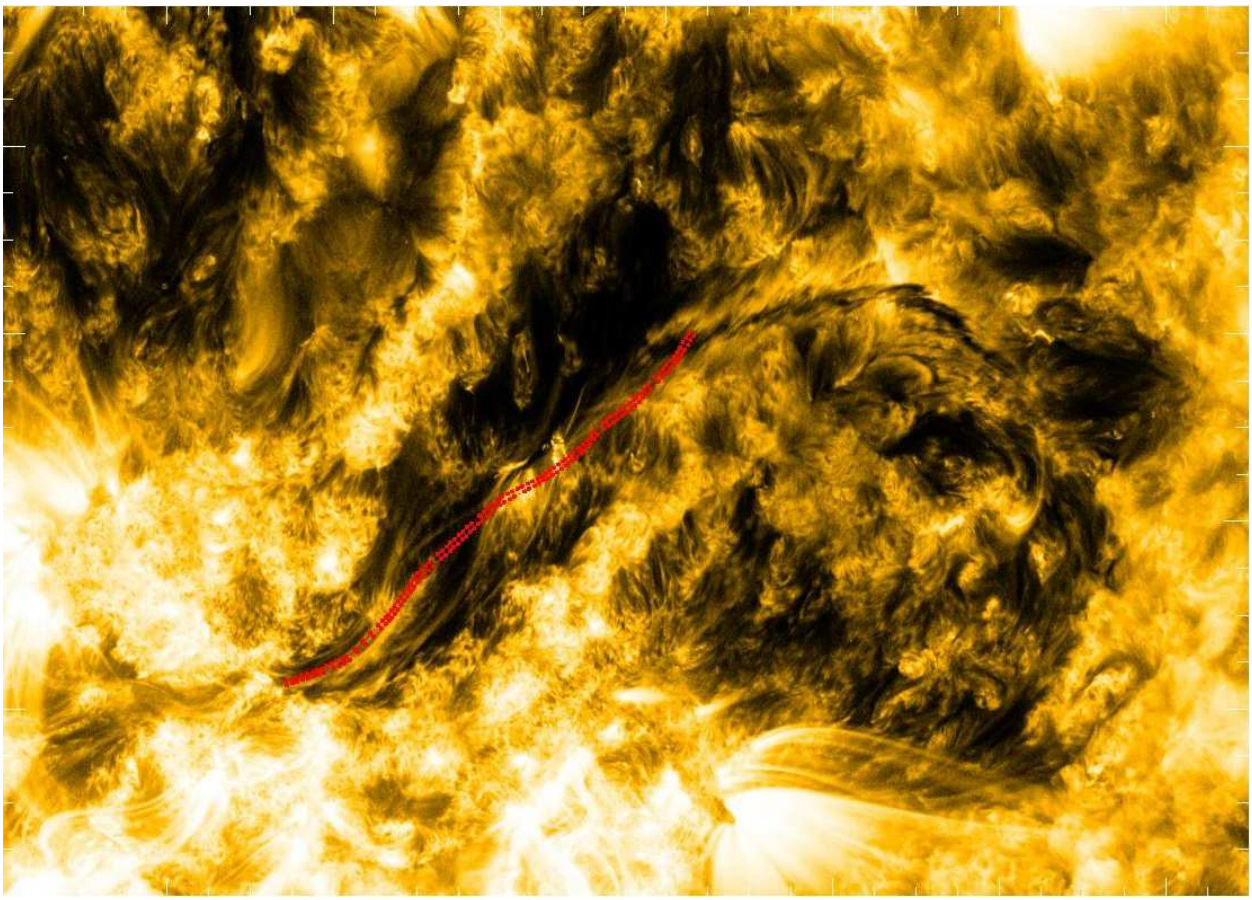

Figure 4.2: Trajectory of the path studied.

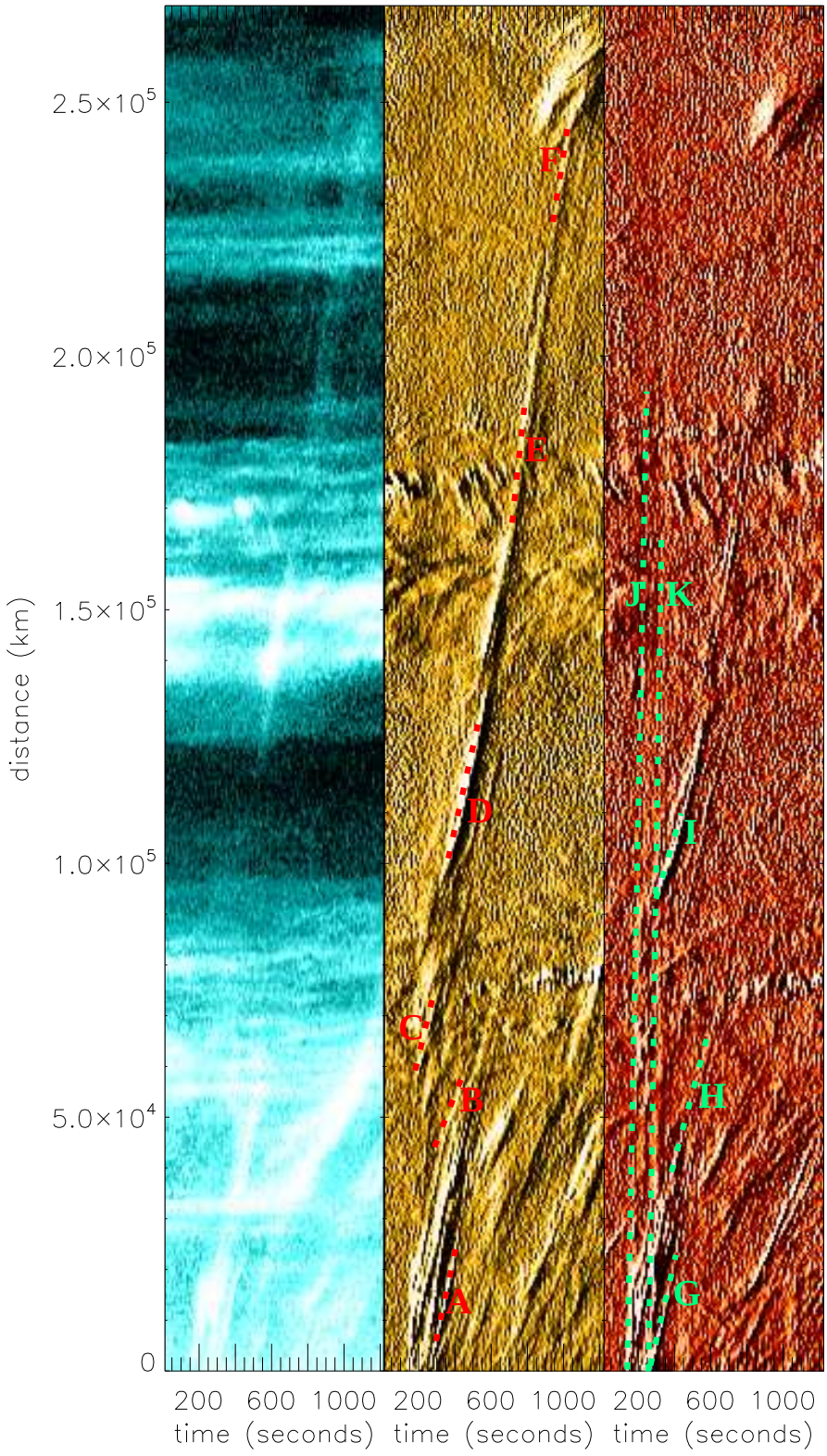

Figure 4.3: (a) distance-time plot for 131Å. (b) running ratio distance-time plot for 171Å. (c) running ratio distance-time plot for 304Å.

Line	Estimated Speed (km s^{-1})	Lower Bound for Speed (km s^{-1})	Upper Bound for Speed (km s^{-1})
A	169	147	196
B	92	82	108
C	150	114	241
D	164	129	204
E	347	194	515
F	236	206	378
G	157	146	190
H	137	119	157
I	121	105	149
J	1827	1472	2407
K	2336	1475	2948

Table 4.1: Observed speeds for 11 features denoted in Figure 4.3

length of the path, the average brightness was sampled at 620 evenly spaced points.

The changing brightness along the trajectory was analyzed by using 102 AIA images, every 12 seconds, and this data was then used to create a stack plot of distance vs time. This plot was further processed by plotting the ratio of each column to the previous - a running ratio plot. On such plots, the gradient of a bright line denotes the speed of a feature that is often reported as a bright blob.

4.4 Results

Animation 1 shows the dynamics of the filament in the 171Å line, between 08:20 and 08:40. It is clear that a bright feature emerges from a very bright region on the eastern side of the filament shortly after 08:20. The feature then appears to "jump" to another location further along the filament, following which the feature proceeds steadily until apparently accelerating on reaching a second very bright region. It is then observed to decelerate on meeting what appears to be denser plasma on the northern side of the filament and apparently ceases to move shortly afterwards. It is worth noting that the very bright regions correspond to areas with a very strong magnetic field according to the HMI data.

The speeds of the main features can be seen most clearly in the 171Å, 304Å and 131Å EUV wavelengths. Figure 4.3 shows a running ratio distance-time plots in the 171Å and 304Å wavelengths, with a distance-time plot (without running ratio) in the 131Å line for comparison. The abundance of features in the system is immediately apparent, with a series of features apparently accompanied by two much faster features.

Table 4.1 shows the estimated speeds deduced for a variety of dotted lines in Figure 4.3, together with their upper and lower bounds. The lower and upper bounds were deduced by considering the bright lines under study and considering the minimum and maximum gradient that could possibly be considered within these

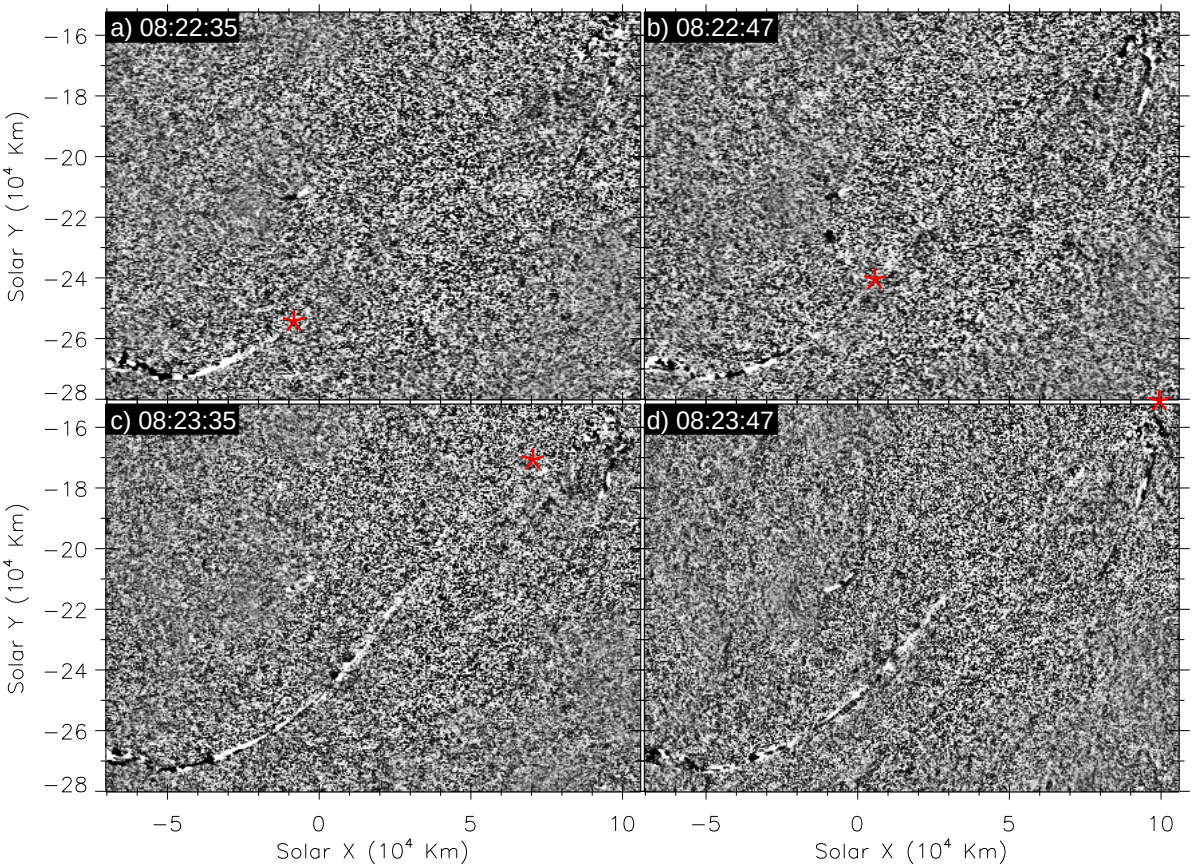

Figure 4.4: Running ratio images in the 171Å wavelength at various times show the rapid progress of features along the trajectory studied.

bright lines. The estimated speeds were deduced by my own approximation of central lines through the bright lines, entirely subjectively. The dotted lines in Figure 4.3 are not an exhaustive list of observed bright lines in Figure 4.3: these would be too numerous to portray and list. Rather, they are an illustrative set of features chosen for their clarity, importance and/or because they are representative of many other features. For instance, line B illustrates the speeds of the slower features, whilst lines J and K outline the fastest features.

A number of these lines outline fairly slow features. Most lines, such as A, B, C, G, H and I, trace features with speeds in the range $90 - 170$km s^{-1}. Line D also falls into this range. However, the feature traced by line D undergoes significant acceleration, from 164km s^{-1} to 347km s^{-1} from line D to line E, which is more than a doubling of the speed. It then decelerates to 236km s^{-1} at line F. Hence lines D, E and F track the astonishing acceleration and deceleration of one particular feature. Finally, there appear to be two very fast features, labeled J and K on the 304Å distance-time diagram, with speeds in the order of 1800km s^{-1} and 2300km s^{-1}.

Animation 2 shows a part of the filament in the 304Å line, between 08:20 and 08:30, using the running ratio technique. The significance of the features along a narrow channel is clear, together with a varying pattern. The rapid progress of a less bright, but still significant, feature along the trajectory, shortly after the first feature is seen emerging from the sunspot, is evident. Figures 4.4a, b and c show the rapid progress of the features, while figures 4.4c and d emphasize the changing patterns that are evident in this animation.

To aid understanding of the speeds involved in this process, Figure 4.4, running ratio is used to show the progression of features shown in Figs. 4.2 and 4.3 more clearly at four time instants. To aid understanding of the running-ratio plots, green 'X' symbols have been placed at my (subjective) approximation of where the blob has arrived at that particular time. The speed of the initial moving feature can be readily seen in these plots. From Fig. 4.4, several characteristics of these moving features can be deduced:

Several characteristics of the features observed can be gleaned from Animation 2 and Figure 4.4. The visual data supports the findings that feature(s) in the channel can indeed have speeds in the order of $\sim$ 2000km s^{-1}. Animation 2 suggests that small amplitude transverse motions exist; the amplitude appears to be approximately 4 pixels (1700km). These patterns change remarkably as the feature moves along the path, and it would ideally be enlightening to use these changes in patterns to characterize the features. However, the small number of pixels involved make this impossible with the spatial cadence provided by the AIA instruments. Furthermore, there appear to be different characteristic lengths in the path followed, which does not allow an accurate measure of the wavelength. However, Animation 2 and Figure 4.4 provide strong

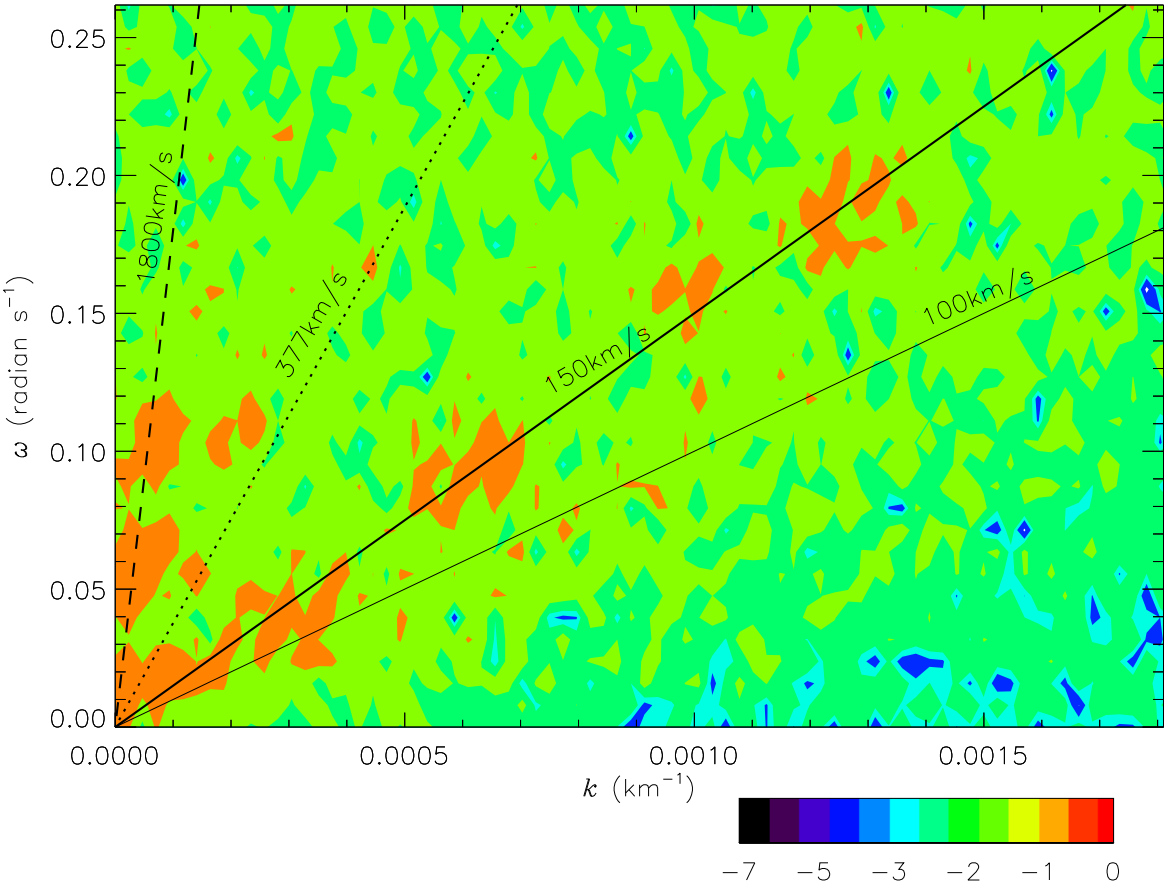

Figure 4.5: Logarithmic power of intensity fluctuations calculated from relative running difference in $\omega - k$ space by applying the two dimensional fast Fourier transform to the data in Figure 4.3c.

evidence of clear feature(s), following a narrow channel, as set out in Figure 4.2. They also confirm at least some of the estimated speeds.

The moving features shown in Figs. 4.3 and 4.4 are analyzed by calculating the two dimensional (time and spatial dimension) fast Fourier transform of the 304Å line running difference intensity using the data from Fig. 4.3c. The result is displayed in Figure 4.5. The dispersion relation of many features with substantial power is shown by this figure. For ease of understanding, several lines are drawn to show the position of different phase speeds. Several wave groups of different phase speeds are seen from this figure. Waves of very fast phase speed (1800 ± 400 km s^{-1}) with substantial power can be found. Their angular frequencies are centered at 0.1, 0.086 and 0.015 radian s^{-1} corresponding to periods of 63s, 105s and 600s. These waves appear to have roughly the same phase speed and are dispersionless. Waves with phase speed around 370-400 km s^{-1} are also recovered but are not as abundant as other groups. Two more groups of slower waves are present too with speed around 150 and 100 km s^{-1}. It is worth noting that the intensity of waves with phase speed around 100 km s^{-1} is rather low but those with phase speed around 150 km s^{-1} are the strongest,

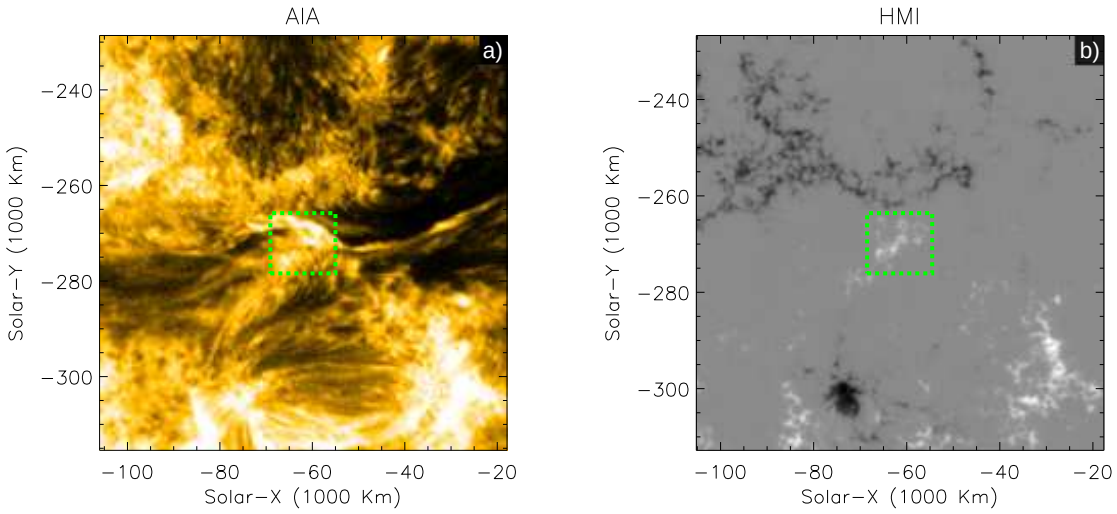

Figure 4.6: The dashed box denotes the area where magnetic flux was estimated over time. This is shown (a) in the AIA 171Å wavelength and (b) in HMI

indicating their predominance in the observations.

4.5 Relation to the Magnetic Field

From studying the HMI data in a small area at the eastern end of the filament where the fast bright waves appeared to be produced, it is clear that the emergence of the waves are co-temporal with a significant local decrease of magnetic flux. Figs 4.6(a) and 4.6(b) show the area under study.

Figure 4.7 shows significant decreases in local magnetic flux in the area where the features producing the bright waves were observed to originate. The first decrease was of 1.88×10^8Wb $\pm$ 1.75×10^8Wb between 08:20:15 and 08:21:45, and the second decrease was of 3.19×10^8Wb $\pm$ 1.75×10^8Wb between 08:23:15 and 08:25:30, representing decreases of approximately 1.5% and 2.6% respectively. Several other significant decreases in magnetic flux appear to correspond to other waves/flows which were not part of the wave train systems; several of these can be seen on the bottom right of the distance-time plots in Figure 4.3.

Further analysis shows that such a variation in the magnetic flux was significantly higher than the mean change measured at random points on the disk. 1000 random points were chosen on a 2000 pixel $\times$ 2000 pixel square on the solar disc, and the magnitudes of changes in magnetic flux summed over the time interval. The mean was 235.8G and the standard deviation was 64.5G. The parameter for the center pixel in the region where the waves originated was 545.5G. Since changes in the magnetic field in the photosphere are well known to cause changes in the chromosphere, this provides compelling evidence of high magnetic activity

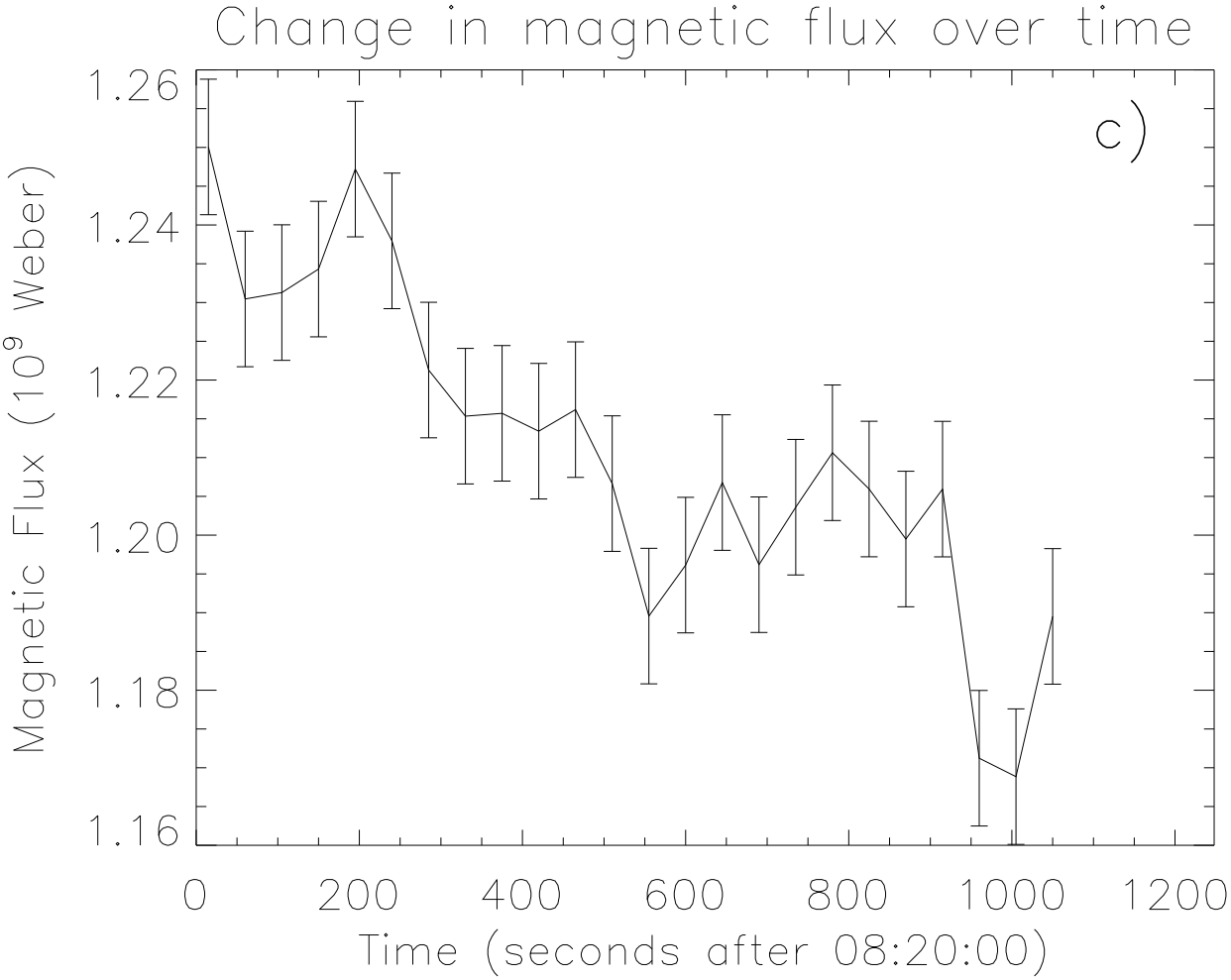

Figure 4.7: Significant decreases of local magnetic flux are observed co-temporal with the appearance of bright fast waves

producing the wave train systems.

4.6 Discussion

One of the bright features appeared to accelerate very significantly, and others show a slight acceleration/deceleration. Some acceleration could be accounted for by line-of-sight effects, but in the case of the path labeled 'A', the magnitude of the velocity roughly doubled, which I feel is strong evidence that acceleration occurred. This leads to the conclusion that the features are waves and not mass flows. The distinction between waves and mass flows is important since various authors have previously interpreted bright blobs as mass flows, and our research indicates that such features are not necessarily mass flows.

It is also clear that the multitude of magneto-acoustic waves appear to stem from the very fast waves on the distance-time plots. This suggests that the very fast waves have stimulated these various magneto-acoustic waves. However, the fact that they have similar but different characteristics regarding speed, intensity, and slight acceleration/deceleration in some cases, suggests that the magneto-acoustic waves are propagating in different flux tubes within the same filament. Different flux tubes could feasibly have different sound speeds, visibility in EUV and so on. This suggests that the very fast waves are in fact propagating across flux tubes in the filament channel, and causing a series of acoustic waves within the various flux tubes. Thus the observations can be interpreted as a wave train system where two very fast waves propagating across flux tubes stimulate a series of acoustic waves in a number of different flux tubes. Such an interpretation also explains the mysterious "jump" seen in Animation 1, where a feature along the channel appeared to "jump" from one location to another location further up the channel within the 12s cadence of the AIA instrument: given the different visibility of the different features in Figure 4.3, it is likely that the magneto-acoustic waves are more visible than the fast waves, and that the magneto-acoustic waves therefore make up most of the observations in the 171Å wavelength.

The interpretation of all the waves other than the very fast waves as magneto-acoustic waves would suggest a varying sound speed within individual strands, since some of the waves have significant acceleration, which initially appears to be strange. However, some of the acceleration appears to occur near very bright areas of the filament channel, where we would postulate that the temperature is higher than elsewhere, which would explain the higher speeds at these locations. Another phenomenon observed is the similar but different sound speed within the various flux tubes. By way of explanation, it is possible that contact with an area where the magnetic field is exceptionally strong causes the wave to "jump" from one flux tube to another, where the plasma parameters may be considerably different and different sound speeds would be plausible.

The very fast waves which appear to generate the wave trains could not possibly be magneto-acoustic waves. They would therefore be either fast waves or Alfvén waves. Given the disturbance and irregularity of intensity along the path of the very fast waves, I would suggest that they are more likely to be fast waves.

It is also noticeable that evidence of these fast waves can be seen even after no more secondary waves are generated. The reasons why these very fast waves eventually cease to produce secondary waves are undetermined, but it is possible that they have insufficient energy remaining, or that any secondary waves produced are so weak as not to register on our distance-time plots.

One interesting feature that can be seen on the distance-time plots is the presence of very close but separate waves exhibiting similar trajectories and speeds. This was also observed by Li et al. (2012) in their studies on EUV waves. Indeed, two fast waves can be seen about a minute apart in the distance-time plots, and the phenomenon is also clear in the case of many of the magneto-acoustic waves. I would argue that this is evidence of two wave train systems, which appear to be traveling along separate trajectories, but exhibiting similar behaviors. It is entirely possible - though not demonstrable - that they may be traveling at different heights.

Bibliography

Alexander, C. E., Walsh, R. W., Régnier, S., et al. 2013, The Astrophysical Journal Letters, 775, L32

Bieber, J. W., Chen, J., Matthaeus, W. H., Smith, C. W., & Pomerantz, M. A. 1993, Journal of Geophysical Research, 98, 3585

Chae, J., Denker, C., Spirock, T. J., Wang, H., & Goode, P. R. 2000, Solar Physics, 195, 333

Chae, J., Wang, H., Qiu, J., Goode, P. R., & Wilhelm, K. 2000, The Astrophysical Journal, 533, 535

Chen, P. F., Innes, D. E., & Solanki, S. K. 2008, Astronomy & AstroPhysics, 484, 487

Deng, Y., Lin, Y., Schmieder, B., & Engvold, O. 2002, Solar Physics, 209, 153

Edwin, P. M., & Roberts, B. 1988, Astronomy & AstroPhysics, 192, 343

Eto, S., Isobe, H., Narukage, N., et al. 2002, Publications of the Astronomical Society of Japan, 54, 481

Gilbert, H. R., Daou, A. G., Young, D., Tripathi, D., & Alexander, D. 2008, The Astrophysical Journal, 685, 629-645

Hershaw, J., Foullon, C., Nakariakov, V. M., & Verwichte, E. 2011, Astronomy & AstroPhysics, 531, A53

Isobe, H., & Tripathi, D. 2006, Astronomy & AstroPhysics, 449, L17

Isobe, H., Tripathi, D., Asai, A., & Jain, R. 2007, Solar Physics, 246, 89

Jelinek, P., & Karlicky, M. 2010, IEEE Transactions on Plasma Science, 38, 2243

Jing, J., Lee, J., Spirock, T. J., et al. 2003, The Astrophysical Journal Letters, 584, L103

Jing, J., Lee, J., Spirock, T. J., & Wang, H. 2006, Solar Physics, 236, 97

Katsiyannis, A. C., Williams, D. R., McAteer, R. T. J., et al. 2003, Astronomy & AstroPhysics, 406, 709

Kucera, T. A., Tovar, M., & de Pontieu, B. 2003, Solar Physics, 212, 81

Kucera, T. A., & Landi, E. 2006, The Astrophysical Journal, 645, 1525

Lemen, J. R., Title, A. M., Akin, D. J., et al. 2012, Solar Physics, 275, 17

Li, T., Zhang, J., Yang, S., & Liu, W. 2012, The Astrophysical Journal, 746, 13

Lin, Y., Engvold, O. R., & Wiik, J. E. 2003, Solar Physics, 216, 109

Lin, Y., Martin, S. F., & Engvold, O. 2008, ASP Conference Series, 383, 235

Lin, Y., Engvold, O., & Rouppe van der Voort, L. H. M. 2012, The Astrophysical Journal, 747, 129

Liu, W., Title, A. M., Zhao, J., et al. 2011, The Astrophysical Journal Letters, 736, L13

Liu, J., Zhou, Z., Wang, Y., et al. 2012, The Astrophysical Journal Letters, 758, L26

Liu, W., Ofman, L., Nitta, N. V., et al. 2012, The Astrophysical Journal, 753, 52

Mackay, D. H., Karpen, J. T., Ballester, J. L., Schmieder, B., & Aulanier, G. 2010, Space Science Reviews, 151, 333

Martin, S. F. 1998, Solar Physics, 182, 107

Nakariakov, V. M., & Roberts, B. 1995, Solar Physics, 159, 399

Nakariakov, V. M., Arber, T. D., Ault, C. E., et al. 2004, Monthly Notices of the Royal Astronomical Society, 349, 705

Nakariakov, V. M., & Verwichte, E. 2005, Living Reviews in Solar Physics, 2,

van Noort, M. J., & Rouppe van der Voort, L. H. M. 2006, The Astrophysical Journal Letters, 648, L67

Okamoto, T. J., Nakai, H., Keiyama, A., et al. 2004, The Astrophysical Journal, 608, 1124

Pascoe, D. J., Nakariakov, V. M., & Kupriyanova, E. G. 2013, Astronomy & AstroPhysics, 560, A97

Schmieder, B., Bommier, V., Kitai, R., et al. 2008, Solar Physics, 247, 321

Shen, Y.-D., Liu, Y., Su, J.-T., et al. 2013, Solar Physics, 288, 585

Tripathi, D., Isobe, H., & Mason, H. E. 2006, Astronomy & AstroPhysics, 453, 1111

Vršnak, B., Veronig, A. M., Thalmann, J. K., & Žic, T. 2007, Astronomy & AstroPhysics, 471, 295

Wang, Y.-M. 1999, The Astrophysical Journal Letters, 520, L71

Zirker, J. B., Engvold, O., & Martin, S. F. 1998, Nature, 396, 440

Williams, D. R., Phillips, K. J. H., Rudawy, P., et al. 2001, Monthly Notices of the Royal Astronomical Society, 326, 428

Williams, D. R., Mathioudakis, M., Gallagher, P. T., et al. 2002, Monthly Notices of the Royal Astronomical Society, 336, 747

Yang, L., Zhang, J., Liu, W., Li, T., & Shen, Y. 2013, The Astrophysical Journal, 775, 39

Yuan, D., Shen, Y., Liu, Y., et al. 2013, Astronomy & AstroPhysics, 554, A144

Chapter 5

Counter-streaming Motions in a Solar Filament

5.1 Preface

In this chapter, observations of counter-streaming motions in a solar filament are discussed. These have been widely observed previously, but not always at such high speeds. In addition, there can be confusion about whether the features observed as counter-streaming are in fact flows or waves. Hence this chapter uses the term "counter-streaming motions" to describe these phenomena. In a very large filament, observed at various times throughout a three-day period, counter-streaming motions are widely observed, and are very fast, often in the order of hundreds of kilometers per second. These speeds are higher than have often been reported previously. Additionally, observations of a bright feature changing direction by 180 degrees are presented, and this sheds new light on the possible explanations for counter-streaming, including the idea of motions being "reflected". Finally, a significant decrease in magnetic flux in an active region is observed immediately prior to the appearance of motions in both directions along the filament originating in the active region; this suggests that changes in the magnetic field could be driving counter-streaming motions. This leads to a number of conclusions and possibilities: that changes in the magnetic field could be an important cause of counter-streaming; that counter-streaming may involve motions being "reflected"; that some counter-streaming could be caused by flux tubes performing a "u-turn" - turning at some point and returning in the opposite 2D direction to which they arrived; and that features frequently interpreted as mass flows are likely to be waves.

5.2 Introduction

Filaments are often the largest structures to be seen on the solar surface. Filaments are long, high, horizontal structures where large amounts of plasma are raised above the solar surface. They often follow polarity inversion lines in the magnetic field. Thanks to significant improvements in the spatial and temporal resolution of observational instruments, the spine of a solar filament has been shown to be composed of a collection of flux ropes, with barbs extending down to the chromosphere, in a similar matter to legs or pillars. It was assumed by many in the past, for instance by Bommier et al. (1994) and Okamoto et al. (2007), that the magnetic field in a filament runs in one direction and that plasma would flow in such a direction. Despite this, many more recent observations have shown counter-streaming motions, where flows and/or waves in different flux ropes have been observed to flow in different directions at the same time. The first observations of this phenomenon are believed to be those of Zirker et al. (1998), who analyzed H-α images to discover counter-streaming flows in the order of $5 - 20$km s^{-1}. Also, counter-streaming flows of around 8km s^{-1} in both directions were discovered by Lin et al. (2003) with H-α observations, by finding the gradient of lines seen in stack plots and also by comparing videos of the blue shift and red shift. Lin et al. (2008) observed more counter-streaming motions in H-α, estimating speeds of $10 - 20$km s^{-1}. Gaizauskas (1998) discovered counter-streaming motions at the edge of a filament suggesting that chirality may be responsible for the counter-streaming. Panasenco & Martin (2008) suggested that mass flows could occur concurrently with counter-streaming flows. Schmieder et al. (2008) found counter-streaming motions to be more evident before an eruption than afterwards and suggested that the processes leading up to the eruption may be responsible for the observed counter-streaming flows. This followed similar research which had claimed a relationship between filament oscillations or brightenings and filament eruptions (Tripathi et al. (2006), Isobe & Tripathi (2006), Chen et al. (2008)). Schmieder et al. (2014) observed a filament both in $H - \alpha$ and 304Å EUV, and found abundant counter-streaming motions in the $H - \alpha$ data along with bright blobs moving at 50-100km s^{-1} in the EUV data. This type of study reinforces the idea that H-α and EUV counter-streaming happen concurrently, but the EUV counter-streaming motions are faster, in part since they are at higher altitude in the corona. Alexander et al. (2013) used data from the Hi-C telescope to discover counter-streaming flows in a solar filament, in Extreme Ultra-Violet (EUV) wavelengths, with speeds of 85km s^{-1} in one direction and 70km s^{-1} in the other. They also argued that the fundamental width of the flux ropes which form the filament may be 0.8 ± 0.1 arc second, with a gap of 0.9 arc second between them. By comparing the normalized intensity in an area where counter-streaming motions had been seen, in different wavelengths with AIA data obtained from the Solar Dynamics Observatory (SDO), and by comparing the locations of the peaks in normalized intensity, they came to the conclusion that mass flows cause counter-streaming

motions. Deng et al. (2002) studied the dynamics of a filament using H-α data to discover counter-streaming motions with speeds of 5-15km s^{-1}, and also observed these as bright blobs. Their study of the motion of the blobs and comparisons with HMI magnetogram time-lapse movies lead them to conclude that there was a connection between the motions of bright blobs and magnetic reconnection seen in magnetograms. Several explanations for the phenomenon were suggested: condensation, injection or increased density. Lin et al. (2012) also observed bright blobs of a similar type, but observed speeds as high as 110km s^{-1}, and suggested that the observed velocities might be the sum of the (low) velocity of the blobs and the velocity of the threads. They ruled out sound waves but suggesting the possibility of fast waves or of solitons. Ahn et al. (2010) observed what they interpreted as counter-streaming flows in a solar prominence with speeds in the order of 20km s^{-1}, and suggested that this was due to "returning flows", i.e. the same feature changing direction, as the result of a restoring force. Their possible interpretations included magnetic tension, the magnetic pressure gradient or as a result of the vertical geometry of the prominence and sag angle of the thread. Another phenomenon that could appear as counter-streaming is longitudinal oscillations along a solar filament, as studied by several authors such as Knizhnik et al. (2014). Vršnak et al. (2007) observed velocities of 51km s^{-1}, whilst Jing et al. (2006) observed velocities of $30-100$km s^{-1}. It is also worth noting that Jing et al. (2006), Jing et al. (2003) and Vršnak et al. (2007) attributed the motions they observed observations at least partially to jets or local subflare activity.

5.3 Methods of Observation

5.3.1 H-α telescopes

Many observations of counter-streaming motions have been achieved with H-α images. This data comes mainly from telescopes located on Earth, and therefore there are various constraints: daylight hours, clouds, weather and atmospheric interference. Despite this, the spatial resolution is high, and H-α observations have often been used to observed counter-streaming motions. It's worth noting that H-α observations focus mostly on cold dense plasma, with temperatures in the order of 10^4K. This plasma is hence likely to move slowly compared to what is observed in EUV wavelengths, which focuses generally on hot plasma in the solar corona. An exception is the 304Å bandpass which observes predominantly colder material but also some hot material. This bandpass contains the HeII line and a SiXII line. However, the H-α observations available in this case had a highly variable temporal cadence and therefore were not suitable for continuous-time analysis.

5.3.2 Solar Dynamics Observatory

In this chapter, observations from the Solar Dynamics Observatory (SDO) are used. The very high spatial and temporal resolution is useful for this work. Data from the AIA and HMI instruments described previously is used to observe counter-streaming motions.

5.4 The Filament Studied

The length of the filament studied was about 500,000km, and the filament was U-shaped. There were at least two areas of strong magnetic flux which appeared to be influencing the filament, and the flux ropes were spread far apart in various locations, which allowed a close study of motions within them. The filament was observed over a period of 3 days, from 2012/08/06 to 2012/08/08. The filament exhibited a partial eruption on the first day. Figure 5.1 shows the location and shape of the filament. This is the same filament as studied in Chapter 4: its large size and distinct flux ropes have yielded multiple sets of results!

5.5 Methods of Analysis

In many previous papers, stack plots were used to visualize and analyze speeds along a 1-D line drawn on an image, usually connecting two points via an area of interest. This type of plot is created by plotting the intensity at points along the line to create a column vector, at various times. These column vectors are then placed side-by-side with each other, thus forming a two-dimensional matrix. This matrix can be plotted in colors and treated as a distance (upwards) vs time (across) graph. This provides the speeds of observed motions, through measuring the gradient and direction of bright (or dark) lines seen in the stack plots.

5.5.1 Following Motions Along Flux Ropes

To use the method outlined above, it is necessary to follow a flux rope in the filament over a period of time. This is a major challenge, considering that both the Sun and the ropes move over time. There are several methods of attempting to follow the flux ropes over a period of time, each with their own advantages and disadvantages.

The Sun rotates, and this means that points on the Solar equator move at a speed of approximately 6875km/hour. Considering that one pixel on the AIA images is around 441km wide, this means that the

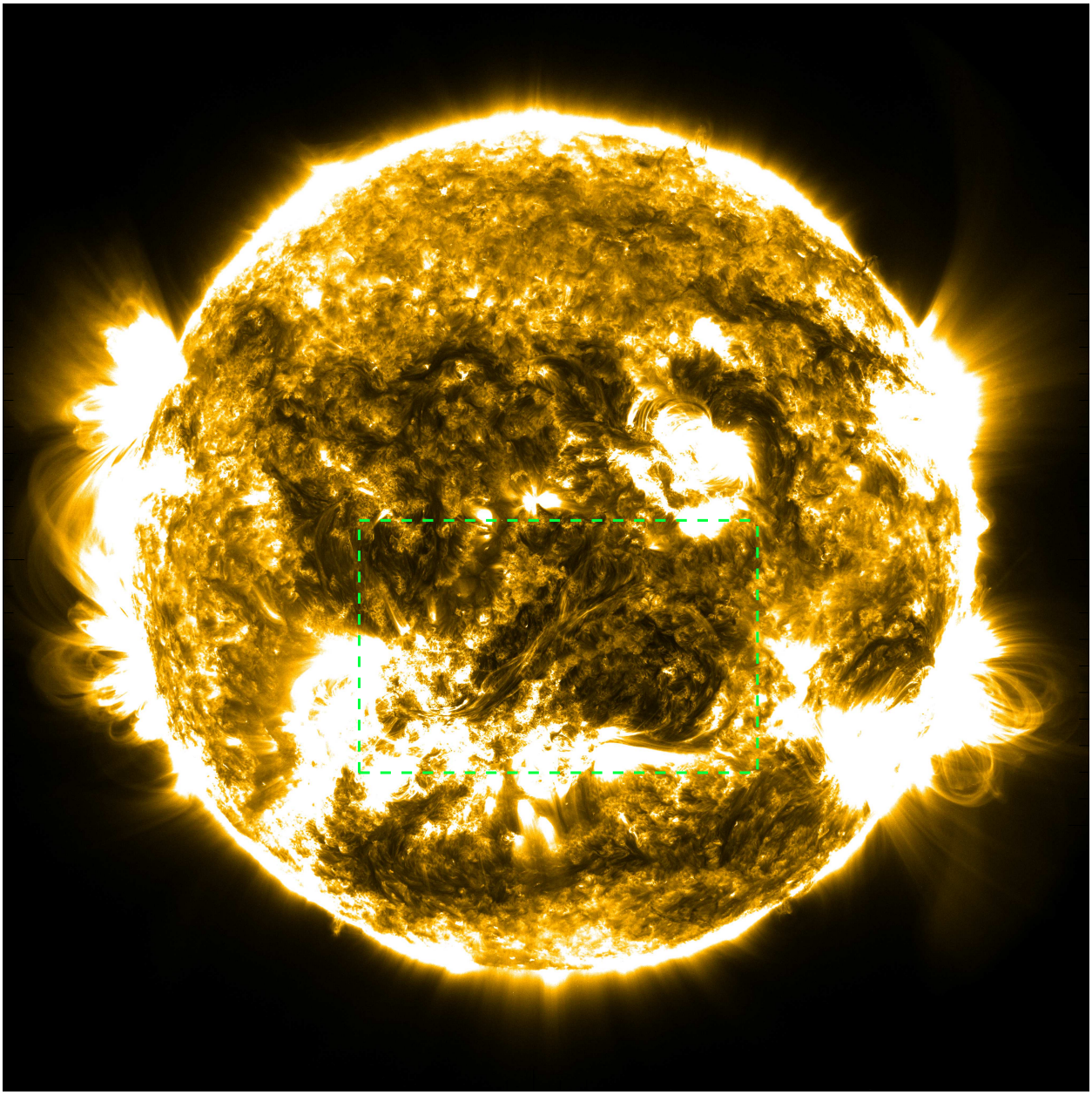

Figure 5.1: The solar disc in the 171Å wavelength at 15:00:01 on 2012-08-06. The green box shows the area of the filament studied and its surroundings.

points in the center of the AIA image move gradually to the right, at a rate of approximately 15 pixels each hour. Therefore, when considering AIA images across a significant length of time, the ropes all appear as if they are moving, and it is not possible to plot a static line to follow motions in any particular rope across a significant length of time. Therefore it is necessary to de-rotate the images so that the structures do not move with the Sun.

The "rot_xy.pro" routine from the solarsoft library is used to achieve this. The program calculates how much any particular point on the Solar disc would move over a period of time. This information can be used to de-rotate the images, so that the structures do not move too much. It is evident that there is no significant movement in the vertical direction and therefore only the horizontal direction requires the use of de-rotation routines.

One of the problems with this is the size of the pixels. The methods de-rotate the image by approximately one pixel every four minutes: if each image is de-rotated every four minutes, the location of the images is not entirely consistent, and in a time-lapse animation the images would appear to be moving slowly to the right and then suddenly moving to the left. Considering that the width of a flux rope is around 1.5 pixels according to (Alexander et al. 2013), it is not acceptable to de-rotate the images as-is, entire pixel by entire pixel. To avoid this, gradual methods must be used to de-rotate the images. By these means, the weighted average of two adjacent cells, in the horizontal direction, can be used to create images which reflect the dynamics of the structure rather than the dynamics of the Sun in general.

Another issue is how to follow any rope in a dynamic system which changes significantly over time.

Outlining Each Rope

Considering that all the flux ropes are meandering and they have no definite geometrical shape, the most obvious answer would be to approximate the shape of the ropes by noting several points along each rope and then to create a series of lines which give a rough impression of the shape of the ropes. However the structures thus denoted are a very particular shape, which is unhelpful because when the flux ropes move position, most aspects of the data that could be obtained by these means is lost. If new series of lines are approximated for each frame, as an attempt to ensure that the series of lines follow the flux ropes as they move, confusion ensues between the different flux ropes and problems ensue regarding the start and end points of the lines. Also, the use of meandering lines is a very subjective method of working. If the experiment was repeated, it is likely that it would yield different results.

This leaves three remaining methods. Two of these depend on estimating the location of the center of the

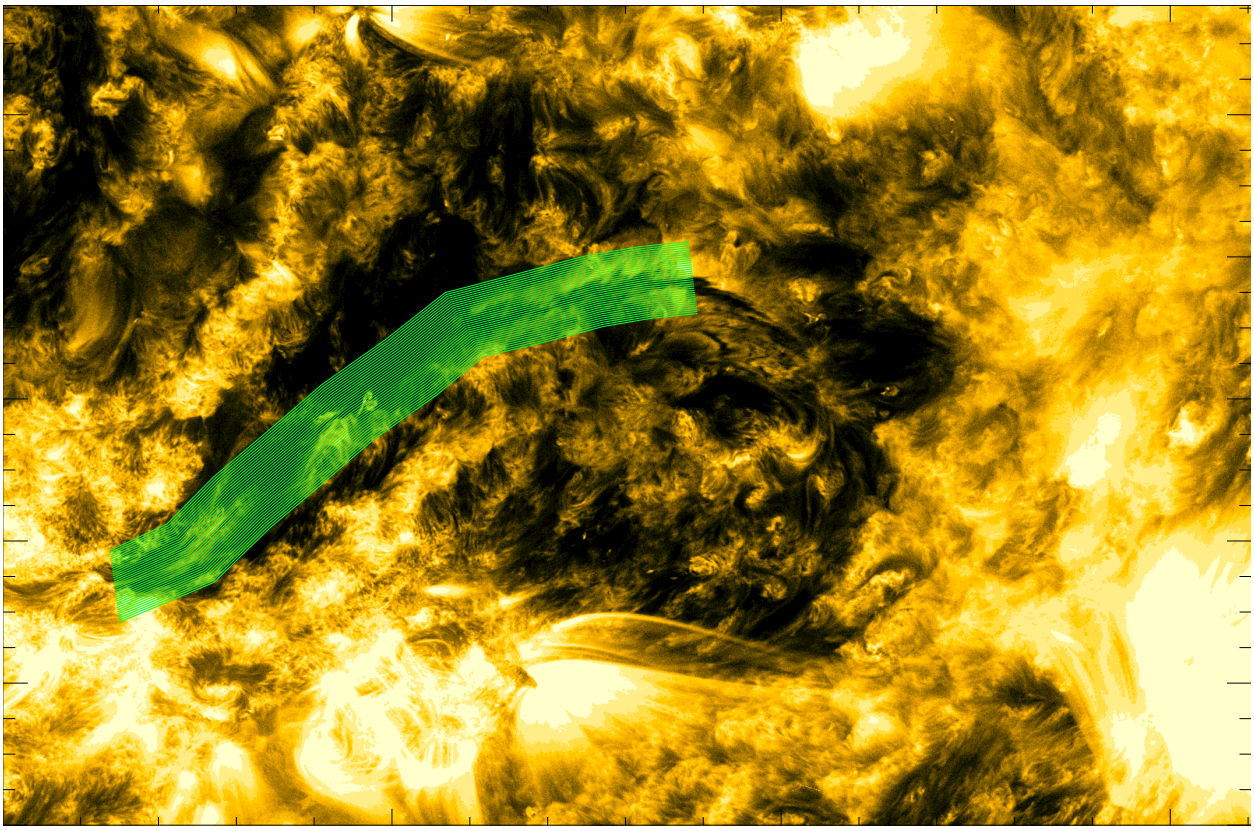

Figure 5.2: Example of following the filament spine, assuming a constant width, with 35 lines, as at 08:00:00 on the second day of observations.

filament spine, and the other involves several separate grids of lines.

Following the filament spine, assuming a constant width

If the location of the center of the filament spine is estimated, this can be treated as the basis for the arrangement of the entire system of flux ropes, assuming that they all follow the same (parallel) path along the filament channel. Therefore one of the methods is to project the lines to both sides, following parallel paths. A series of points is created by using the equations

$x_2 = x_1 + bn\sin\theta$, $y_2 = y_1 - bn\cos\theta$

Where x_1 and y_1 are the original co-ordinates, x_2 and y_2 are the new co-ordinates, b is the assumed gap between the flux ropes and n is the rope number (n could be negative in order to estimate ropes to the top-left of the center of the filament spine)

Figure 5.3 shows the proposed location of the flux ropes, with 35 ropes, where -17≥n≥17. Figure 5.2 shows the results of this, in the 131Å wavelength. Note that the bright features do not extend particularly far on

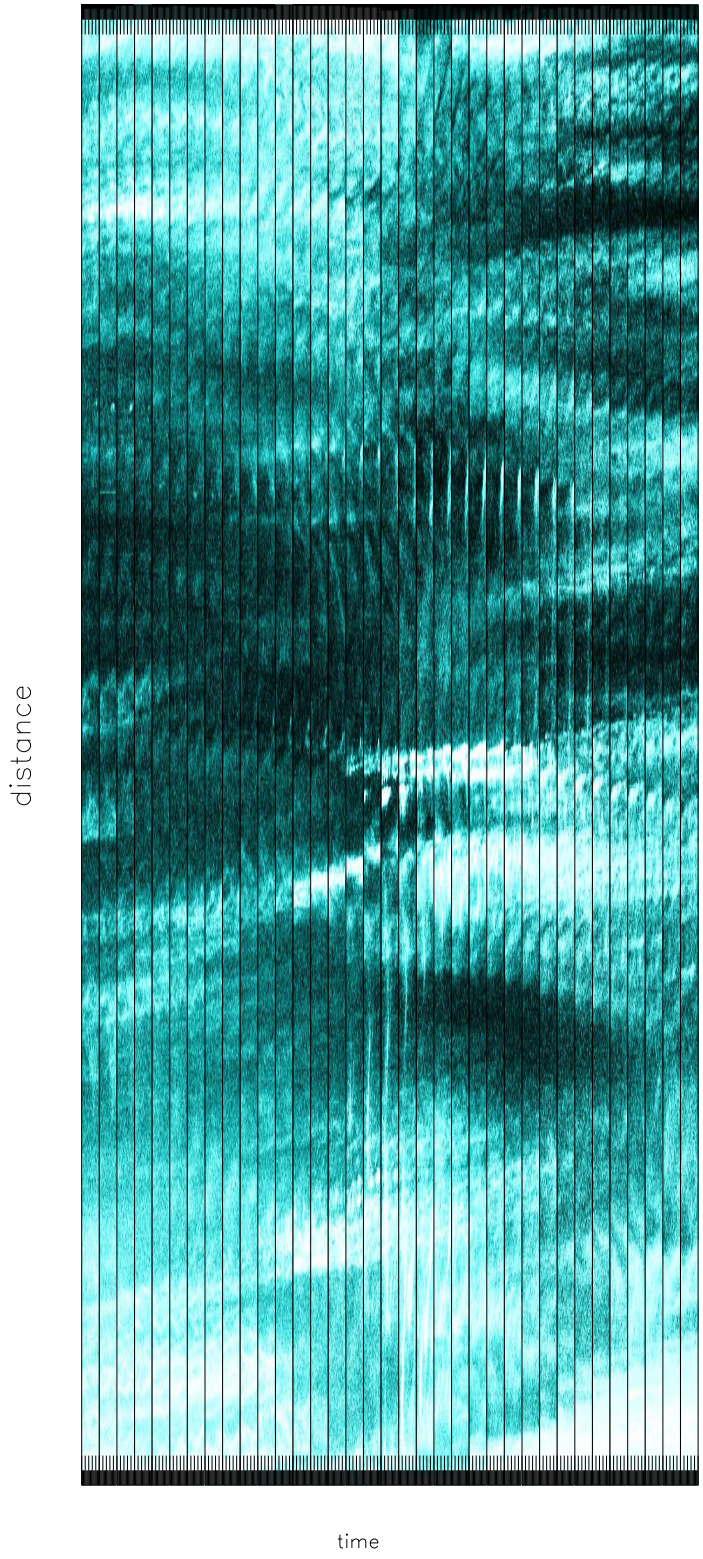

Figure 5.3: The results for the method outlined in Figure 5.2, with 35 lines, in the 131Å wavelength. Each of the 35 distance-time plots corresponds to a particular line, and features in the distance-time plots should indicate movements along flux ropes. The lines do not appear to follow the flux ropes particularly well. Time is for each particular line (due to spatial constraints inclusion of scales for these would not be feasible

the distance-time plots, which suggests that the lines do not follow the flux ropes very well.

Following the Center of the Filament Spine, Allowing the Width to Vary

The other method which stems from estimation of the center of the filament spine is that which considers variations in the filament width along the filament length. The images often show filaments are wider in some areas and narrower in other areas. Therefore a method of estimating the filament boundaries is used so that it is possible to foresee the location of each flux rope. For each point on the filament spine, the average of the angle to the horizontal of the line which connects the point to the previous and next point are calculated, and called θ_3. At the first and last points, only the relevant angle is used. A line is drawn through each point with the angle $\theta_3 - 90$deg, and then the locations where these lines reach the edge of the filament is noted. In this way, the boundaries of the filament are represented. An obvious problem arising from this method is the subjective element in the process of defining the filament boundaries.

If this method is used, the gaps between the flux ropes will vary along the filament. Therefore, although the variable defining the location of the flux ropes in the previous method was the gap between the flux ropes, here the variable defining the location of the flux ropes is the number of flux ropes in the channel. If we are to continue with the same gap between the ropes, the average of the width of the filament along its length can be calculated, and then the filament width can be divided by the proposed gap between the lines to find the most appropriate number of lines to use. Then the equations below can be used to calculate the series of points which define the layout of the proposed ropes:

$x_2 = x_t - (x_t - x_g)n/c$, $y_2 = y_t - (y_t - y_g)n/c$

Where x_2 and y_2 are the new co-ordinates, x_t and y_t are the co-ordinates of the top boundary, x_g and y_g are the co-ordinates of the lower boundary, c is the number of ropes and n is the number of the rope under consideration, where $0 \leq n \leq c$

Figure 5.4 shows the location of the proposed lines, with 35 lines, where $c = 35$. Figure 5.5 shows the results of this, in the 171Å wavelength. Note that the bright features do not extend very far along the distance-time plots, which suggests that the lines do not follow the flux ropes particularly well.

Separate Sets of Straight Lines

The last and simplest method is to recognize the problems of trying to follow flux ropes in a dynamic structure such as a filament and therefore outline a set of straight lines along parts of the filament, in several

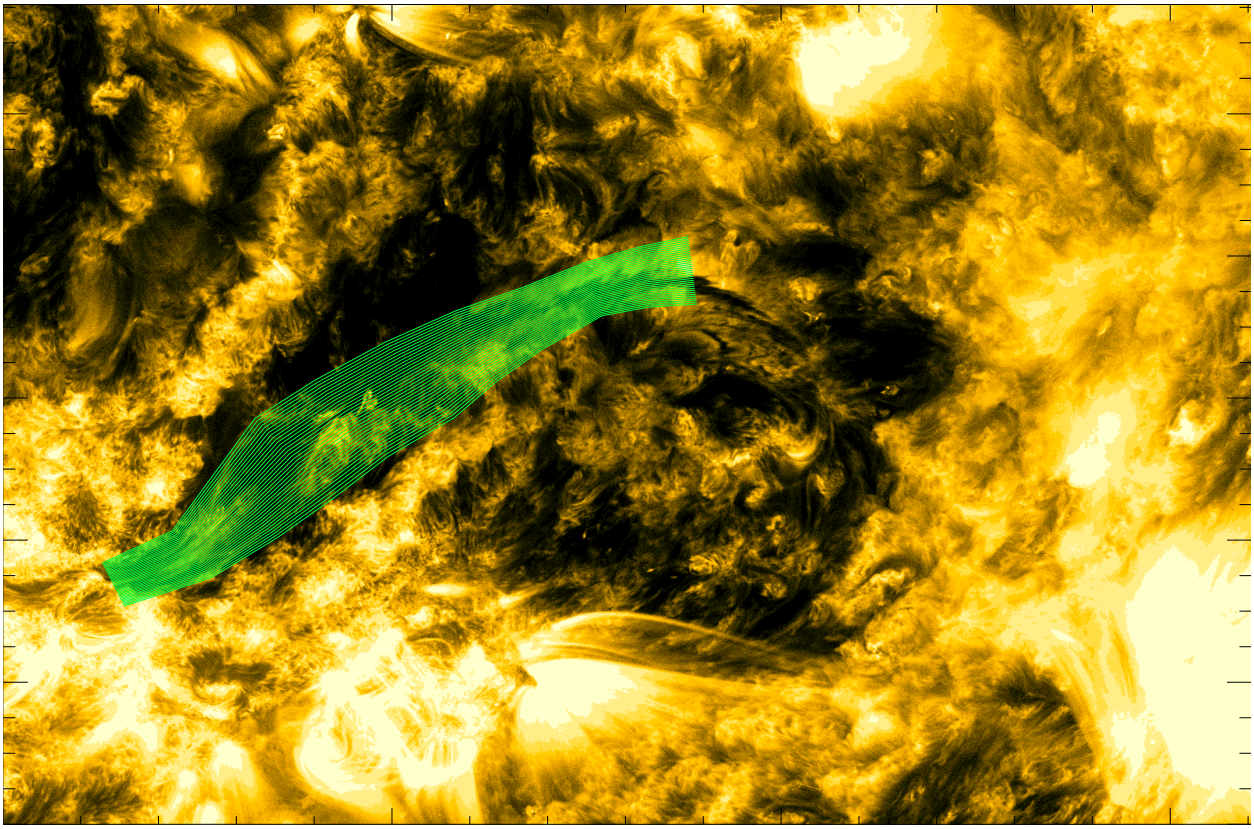

Figure 5.4: An example of following the center of the filament spine, allowing the width to vary, with 35 lines, as seen at 08:00:00 on the second day of observations.

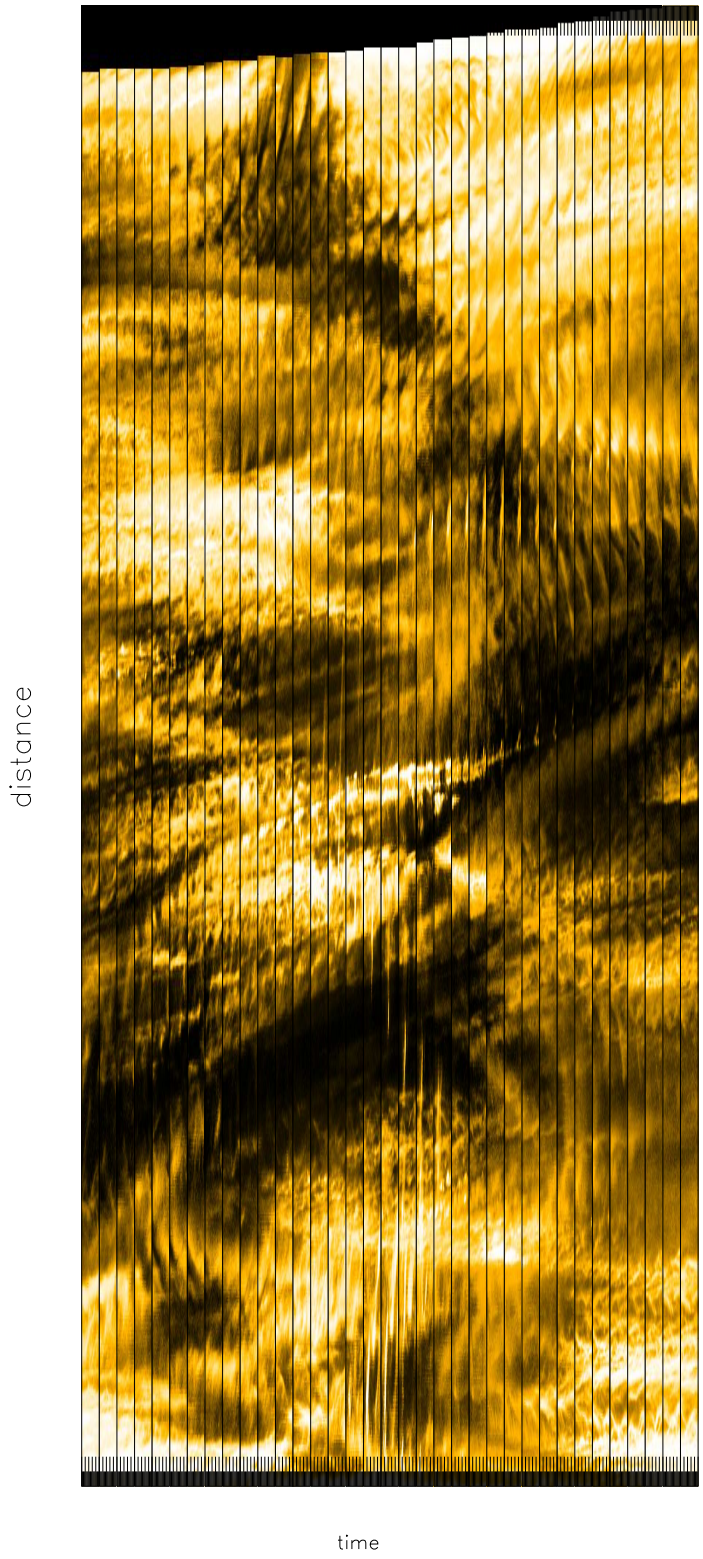

Figure 5.5: Results for the method outlined in Figure 5.4 with 35 lines, in the 171Å wavelength. It appears that the lines do not follow the flux ropes particularly well.

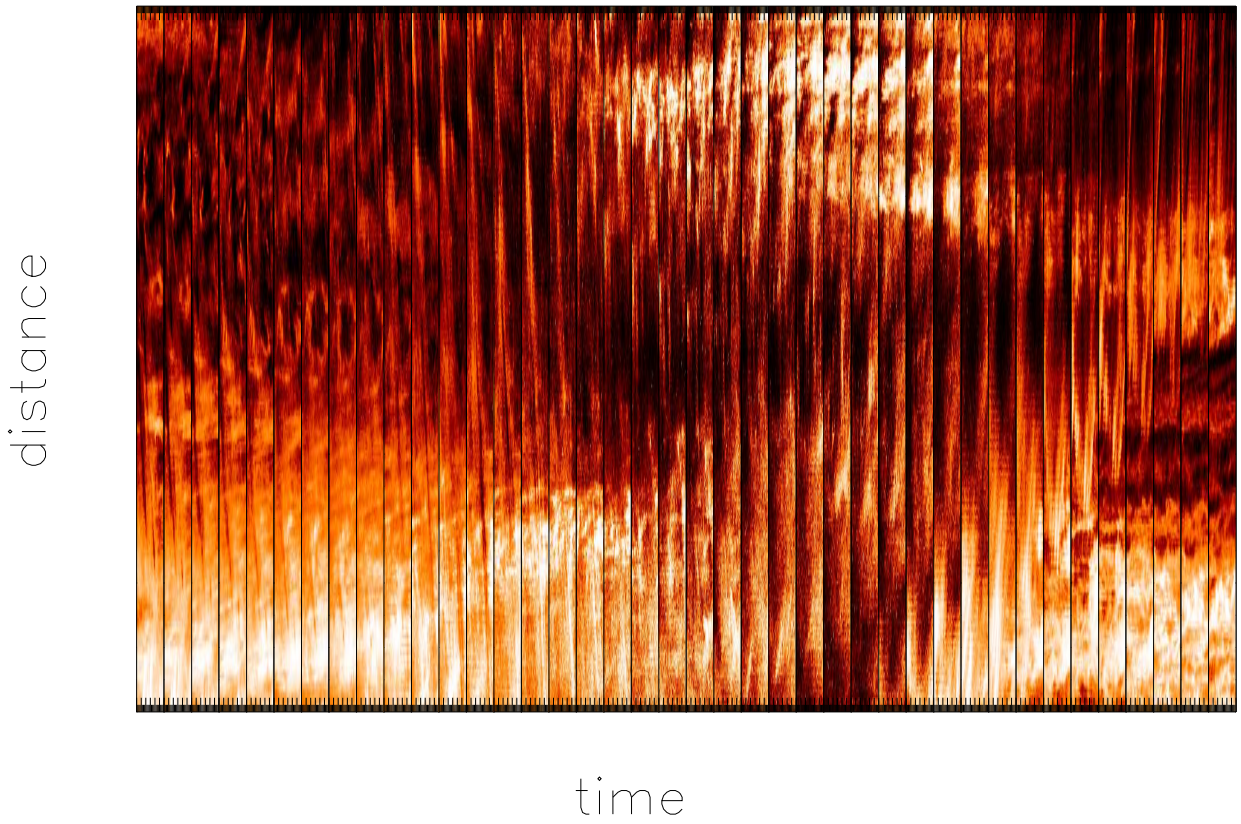

Figure 5.6: 40 lines, using separate sets of straight lines.

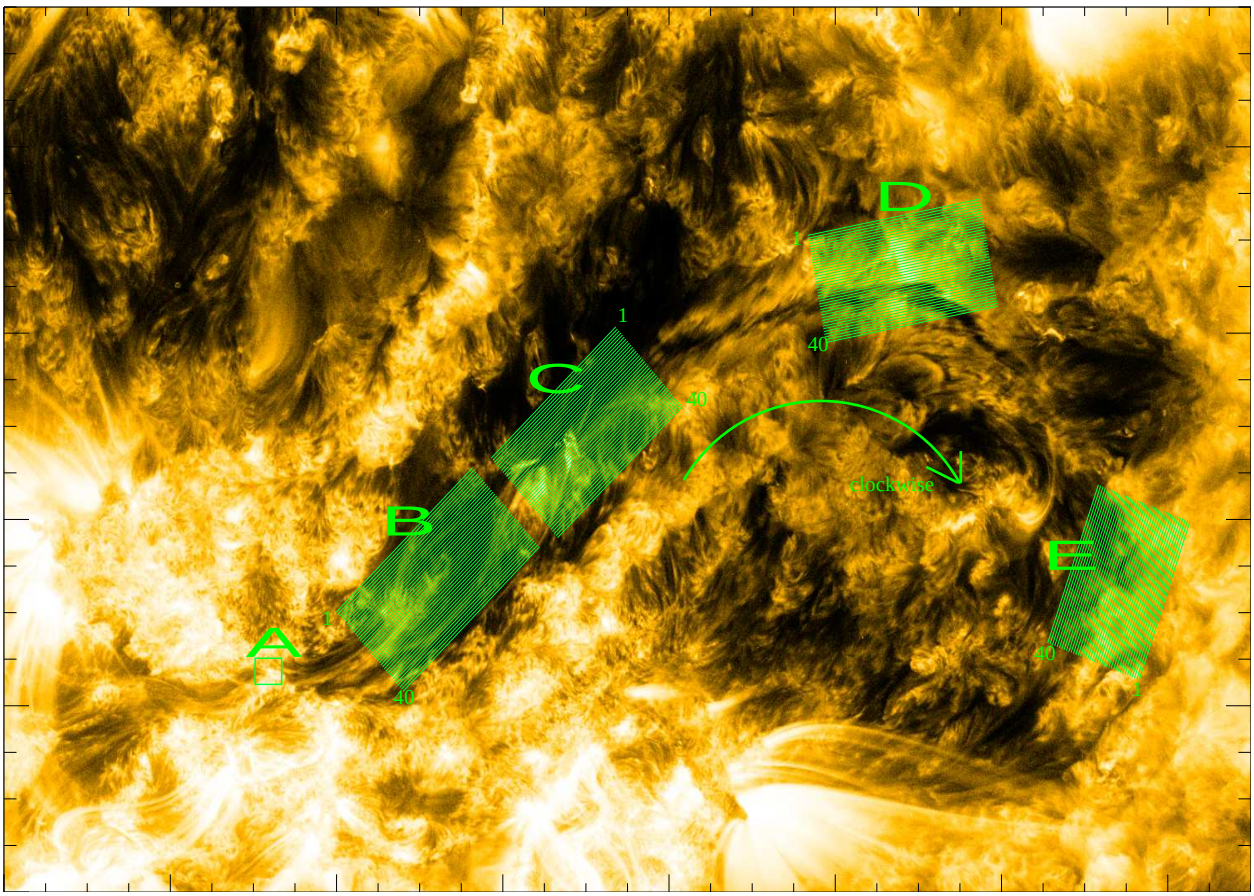

Figure 5.7: Locations of the lines. The letters denote locations B, C, D and E, where 40 lines along the filament channel were considered at each location, and the numbers denote the numbering of the lines within a set of lines, i.e. 1 denotes the first line and 40 denotes the 40^{th} line in a particular location. Due to the U-shaped nature of the filament, velocities will be expressed in terms of clockwise and anticlockwise, as indicated by the arrow. Location A is an area of strong magnetic flux which will be discussed at length later in this chapter.

different locations, in order to compare movements in nearby flux ropes. Although it is still possible for the ropes to move, and the lines often jump from one rope to the other, the method is successful, as seen in this chapter. The evidence for events can be strengthened by observing the same phenomenon in several different ropes. An example is expressed in Figure 5.6. The method is simpler and is not seen to be less effective than the other methods discussed. As a result, this is the method used in the research.

5.5.2 Choosing Locations

As already explained, the filament under study is very long and U-shaped. As can be seen in Figure 5.7, four different locations were chosen (location A is an area of strong magnetic flux which will be discussed further later on in this chapter). Location B is at the start of the filament, where much activity was seen. Location

C contains an area of strong magnetic flux. Location D contains an area where a partial eruption was seen to occur. Location E is on the western side of the filament, where less activity was seen, and although the filament appears to move from the area by the third day of observations, my view is that it is still important to consider this part of the filament.

The locations were chosen to reflect the location of the filament for most of the first day and the first part of the second day. Although the filament does move away from two of the locations by the third day, it is important to maintain consistency regarding the location of the lines in order to compare the behavior of the filament at different times.

5.6 Showing the Presence of Counter-streaming Motions

The process for choosing one-dimensional lines which describe the changes in intensity on a range of points along the line was described above. By performing this procedure on images from different times, it is possible to examine the changes in two dimensions - distance and time.

5.6.1 Distance-Time Plots

The data obtained can be used to create distance-time plots of the spatial and temporal changes along a chosen line. Such plots are obtained first by noting the intensity at a set of evenly spaced points, as a column vector. Usually, the co-ordinates of such points will not take integer values and in such cases a weighted average is taken of the four surrounding pixels. By performing this for several images at a constant time interval, a two-dimensional matrix is created, which can be colored according to intensity to provide a visual representation of the differences in intensity. Such an image has distance as the vertical axis and time as the horizontal axis. Examples can be seen in Figures 5.3 and 5.5.

5.6.2 Interpreting the Distance-Time Plots

Since velocity=displacement/time (and a negative displacement is entirely valid), the gradient of any line on a distance-time plot will provide the speed and direction of observed motions. Therefore bright (or in some cases dark) lines on the distance-time plots denote motions (mass flows or waves), and the angle between such lines and the horizontal allows calculation of the velocity. Such bright lines are frequently unclear, and it can be difficult to estimate where they begin and end. At times, the spatial resolution is insufficient to

measure the speed of very fast movements. Therefore the approximations of speeds given in this chapter are, to some extent, only an arbitrary decision and therefore lower and upper limits are also provided.

5.7 Results - counter-streaming motions in parallel flux ropes

Figure 5.6 shows fast motions in 40 lines between 15:00 and 15:20 on the first day of observations. Motions can be clearly seen in several of the distance-time plots. A bias is also observed for motions to travel in one direction on one side of the filament and in the other direction on the other side. Despite all this, it is difficult to clearly see the features and speeds in such a small graph, and therefore in the rest of this paper the distance-time plots will be presented in pairs. The following table and figures show clearly some of the motions observed along different lines. It appears that there are many counter-streaming motions, and they are frequently fast.

Table 5.1 shows some of the observed motions, in several locations and at several different times. Each distance-time plot was considered seperately, and the line upon which the fastest motion in each direction was observed was noted, in addition to their speeds. Because calculating the speeds is a largely subjective process, lower and upper limits are also provided. Where it is not feasible to compute an upper limit, a problem which affects some of the fastest motions, the (lack of) upper limit is denoted by a star (*).

Table 5.1 provides strong evidence for fast motions in several locations and at several different times, but the speeds vary spatially and temporally. Speeds are generally lower at location E. Speeds are also generally lower throughout the filament on the third day of observations than on the first and second days.

The fastest motions appear in location B on the morning of the second day, for instance 420-430km s^{-1} clockwise and 225km s^{-1} anti-clockwise, but there is also much evidence for fast motions on the first day, for example 275km s^{-1} in the clockwise direction at 15:00-15:20 in the 171Å wavelength, and 250km s^{-1} in the anti-clockwise direction at 17:20-17:40 in the 171Å wavelength.

The quietest location is location E. Several factors could be responsible for this: it is far from the strong magnetic features that appear to interact with the filament on the eastern side, it appears less developed structurally than the eastern side of the filament, and this part of the filament moves significantly during the period of observation, such that not many flux ropes appear to be aligned with the grid by the third day of observations. It is likely that the last factor is chiefly responsible for the lack of results at location E on the third day. Despite this, motions of 95km s^{-1} are seen in the clockwise direction in the 193Å wavelength on the first day, 50km s^{-1} in the anti-clockwise direction in the 171Å on the first day, and on the second

Table 5.1: The greatest speeds observed, in both directions, in several locations and at several different times, are denoted in bold. The numbers in brackets denote the lower and upper limits, while the line number denotes the line where the motions under study were observed, counting from the top-left.

Wavelength (Å)	Line number	Clockwise speed (estimated) (km s^{-1}) (lower bound, upper bound)	Line number	Anti-clockwise speed (estimated) (km s^{-1}) (lower bound, upper bound)
2012-08-06 , 15:00-15:20 , location B				
171	40	**275** (215,415)	12	**180** (145,290)
193	27	**205** (110,255)	8	**105** (90,130)
211	30	**225** (160,295)	9	**255** (155,380)
304	35	**190** (130,205)	7	**140** (110,180)
2012-08-06 , 15:00-15:20 , location D				
171	35	**70** (30,95)	9	**165** (125,285)
193	25	**50** (35,65)	10	**85** (65,100)
211	37	**45** (30,55)	13	**80** (55,90)
304	30	**125** (110,160)	8	**180** (115,250)
2012-08-06 , 17:20-17:40 , location B				
171	12	**160** (110,180)	15	**250** (170,290)
193	12	**205** (120,390)	13	**205** (135,375)
211	12	**190** (135,305)	15	**145** (100,240)
304	16	**205** (165,300)	6	**150** (85,220)
2012-08-06 , 17:20-17:40 , location D				
171	18	**105** (80,165)	3	**145** (115,195)
193	21	**195** (110,250)	3	**165** (120,220)
211	12	**95** (85,120)	3	**190** (150,260)
304	12	**215** (145,275)	13	**140** (110,155)
2012-08-06 , 17:20-17:40 , location E				
171	17	**55** (50,65)	19	**50** (30,90)
193	15	**95** (65,110)	20	**40** (35,50)
304	32	**50** (40,95)	7	**80** (70,100)
2012-08-07 , 08:20-08:40 , location B				
171	11	**420** (165,*)	25	**225** (125,*)
193	8	**380** (215,*)	23	**155** (80,*)
211	7	**290** (165,*)	19	**140** (75,345)
304	7	**255** (190,275)	6	**90** (75,110)
2012-08-07 , 08:20-08:40 , location D				
304	18	**80** (70,170)	3	**45** (35,60)
2012-08-07 , 08:20-08:40 , location E				
304	23	**110** (50,210)	5	**70** (35,110)
2012-08-08 , 08:20-08:40 , location B				
171	27	**130** (95,165)	4	**85** (60,125)
304	22	**55** (45,70)	4	**90** (70,110)

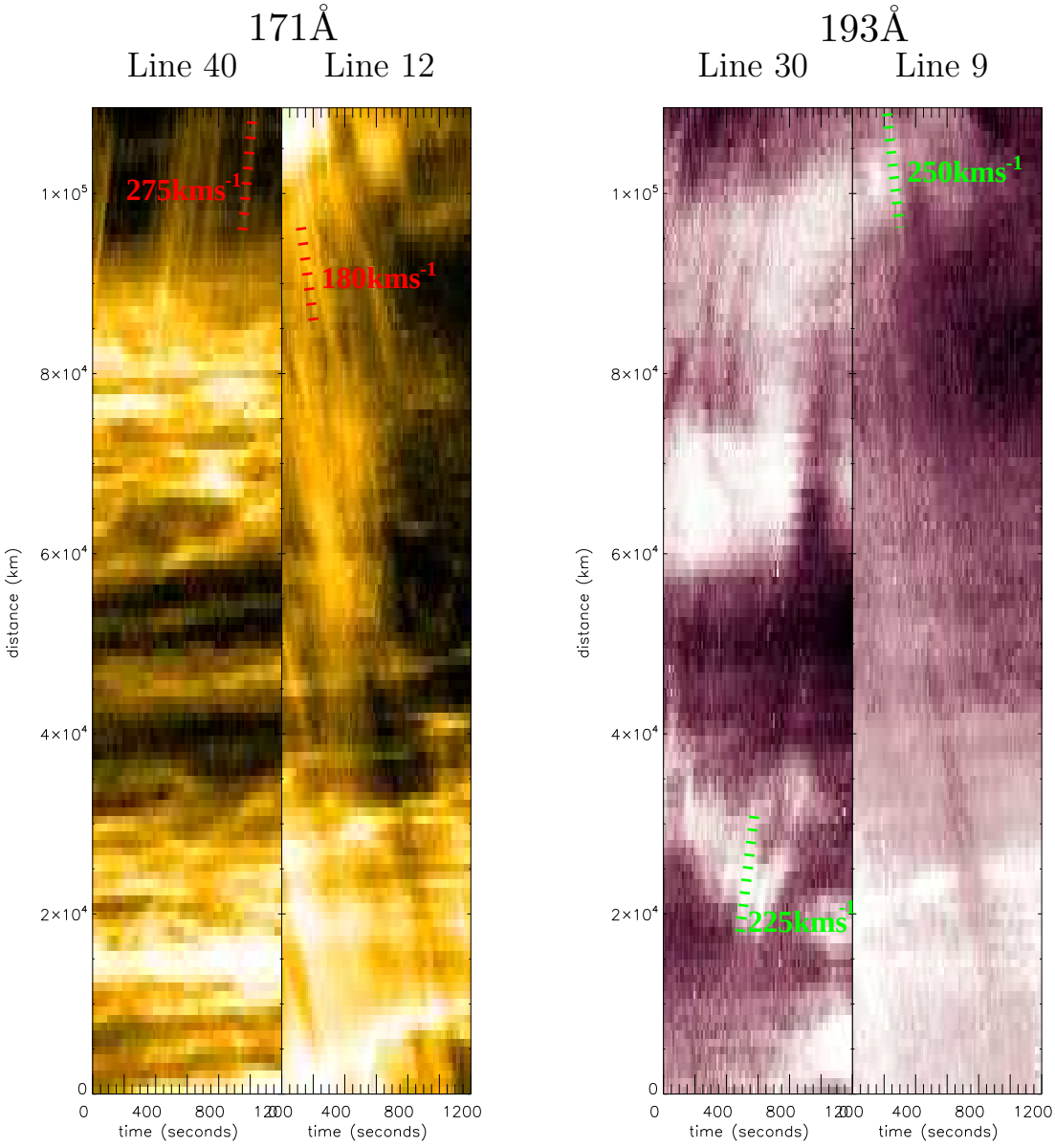

(a) 171Å

(b) 211Å

Figure 5.8: Location B, first day, 15:00-15:20. (a): The 40^{th} and 12^{th} lines in the 171Å wavelength show fast motions in different directions, for example 275km s^{-1} clockwise and 180km s^{-1} anti-clockwise. (b): The 30^{th} and 9^{th} lines in the 211Å wavelength show fast motions in different directions, for instance 225km s^{-1} clockwise and 250km s^{-1} anti-clockwise.

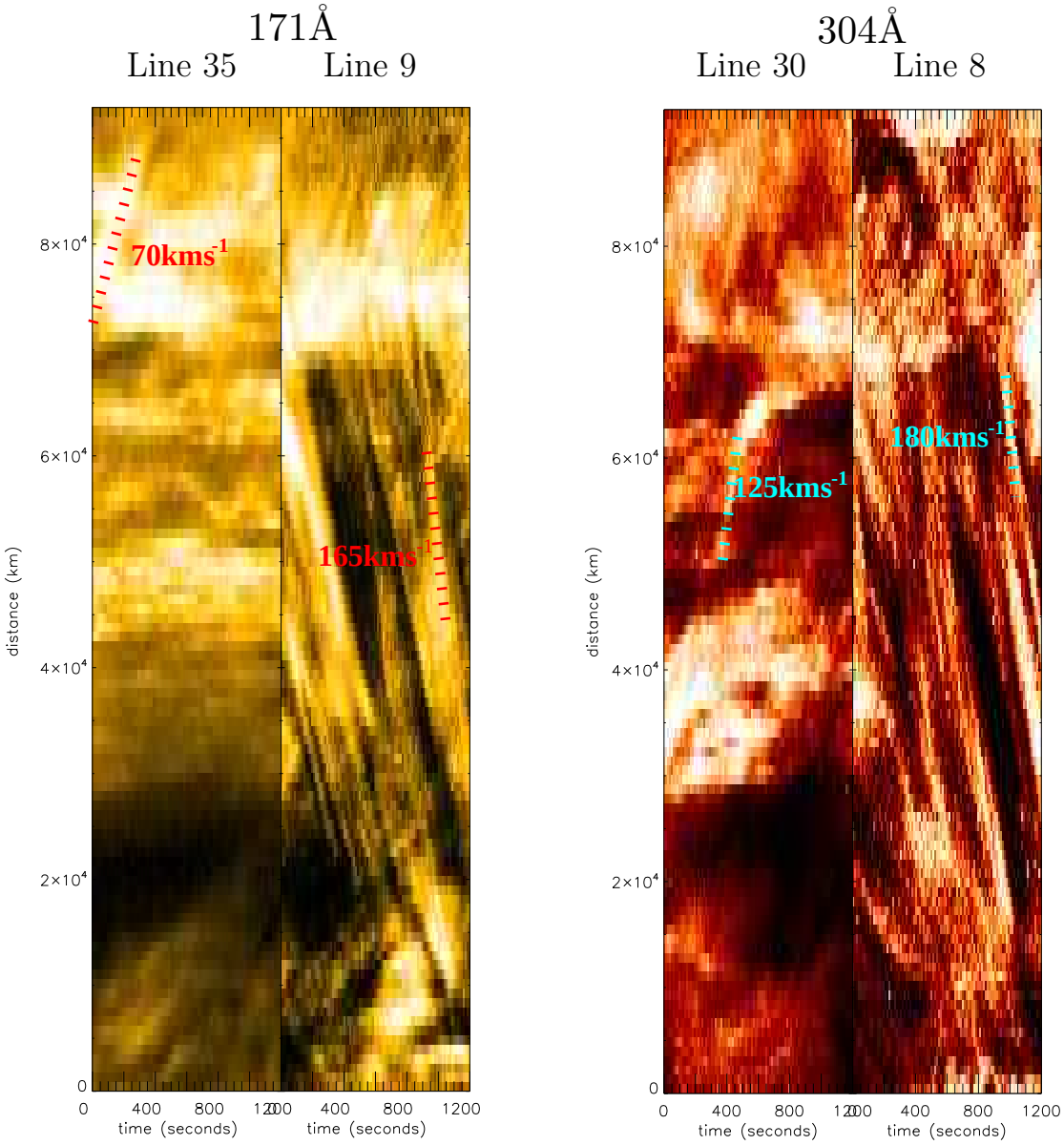

(a) 171Å

(b) 304Å

Figure 5.9: Location D, first day, 15:00-15:20. (a): The 35^{th} and 9^{th} lines in the 171Å wavelength show fast motions in different directions, for example 70km s^{-1} clockwise and 165km s^{-1} anti-clockwise. (b): The 30^{th} and 8^{th} lines in the 304Å wavelength show fast motions in different directions, for instance 125km s^{-1} clockwise and 180km s^{-1} anti-clockwise.

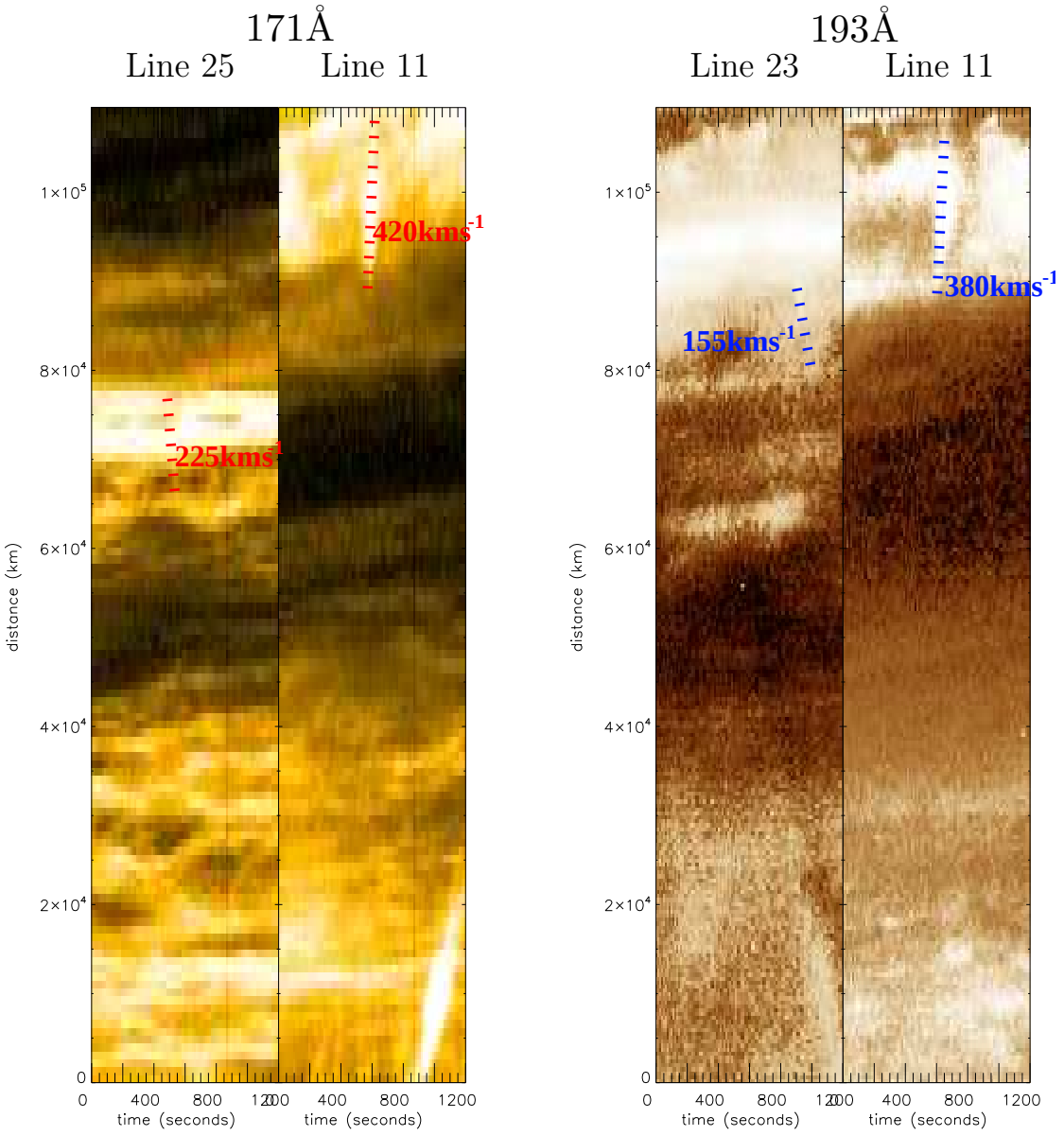

(a) 171Å

(b) 193Å

Figure 5.10: Location B, second day, 08:20-08:40. (a): The 25^{th} and 11^{th} lines in the 171Å wavelength show fast motions in different directions, for example 420km s^{-1} clockwise and 225km s^{-1} anti-clockwise. (b): The 23^{rd} and 11^{th} lines in the 193Å wavelength show fast motions in different directions, for instance 430km s^{-1} clockwise and 155km s^{-1} anti-clockwise.

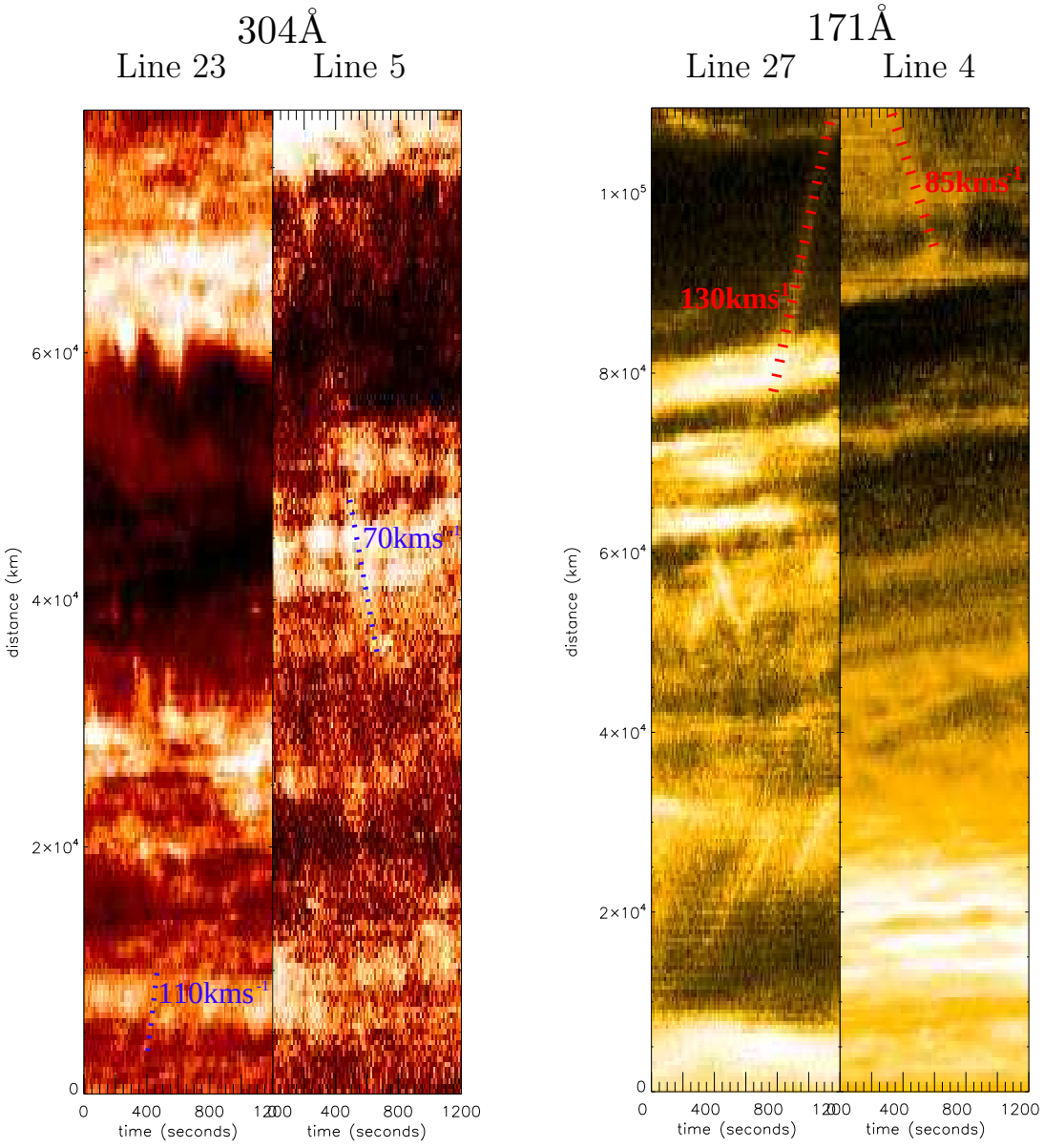

(a) 304Å

(b) 171Å

Figure 5.11: (a): Location D, second day, 08:20-08:40. The 23^{th} and 5^{th} lines in the 304Å wavelength show fast motions in different directions, for instance 110km s^{-1} clockwise and 70km s^{-1} anti-clockwise. (b): Location B, third day, 08:20-08:40. The 27^{th} and 4^{th} lines in the 171Å wavelength show fast motions in different directions, for instance 130km s^{-1} clockwise and 85km s^{-1} anti-clockwise.

day there are motions of 65km s^{-1} in the clockwise direction and 60km s^{-1} in the anti-clockwise direction in the 304Å wavelength.

The speeds also appear to decrease by the third day, and even in location B, the observed speeds are significantly lower than on the first and second days, for instance 130km s^{-1} in the clockwise direction in the 171Å wavelength and 90km s^{-1} in the anti-clockwise direction in the 304Å wavelength. Despite this, the motions are still significant and they are still much faster than the mass flows seen in H-α observations.

Figures 5.8-5.11 are provided to give a visual explanation of the situation, as examples of observed counter-streaming motions.

Figure 5.8 shows motions of 275km s^{-1} in the clockwise direction and 180km s^{-1} in the anti-clockwise direction in the 171Å wavelength, and motions of 225km s^{-1} in the clockwise direction and 250km s^{-1} in the anti-clockwise direction in the 211Å wavelength, in location B on the first day. Figure 5.9 shows motions of 70km s^{-1} in the clockwise direction and 165km s^{-1} in the anti-clockwise direction in the 171Å wavelength, and motions of 125km s^{-1} in the clockwise direction and 180km s^{-1} in the anti-clockwise direction in the 304Å wavelength, in location D on the first day. Figure 5.10 shows motions of 420km s^{-1} in the clockwise direction and 225km s^{-1} in the anti-clockwise direction in the 171Å wavelength, and motions of 430km s^{-1} in the clockwise direction and 155km s^{-1} in the anti-clockwise direction in the 193Å wavelength, in location B on the first day. Figure 5.11a shows motions of 65km s^{-1} in the clockwise direction and 60km s^{-1} in the anti-clockwise direction in the 304Å wavelength, in location E on the second day. Figure 5.11b shows motions of 130km s^{-1} in the clockwise direction and 85km s^{-1} in the anti-clockwise direction in the 171Åwavelength, in location B on the third day.

5.8 Results - Behaviors Exhibited whilst Interacting with a Region of Strong Magnetic Flux

Location C is significantly different from the other locations because it contains areas of strong magnetic flux which, from AIA observations and time-lapse movies, appear to be interacting with the filament. Figure 5.12 shows the magnetic field observed by the HMI instrument at 08:20:15 on the second day of observation, together with the lines analyzed. The HMI data shows significant patches of white, which denote areas where the magnetic field is strong and positive, beneath the lines denoted by C.

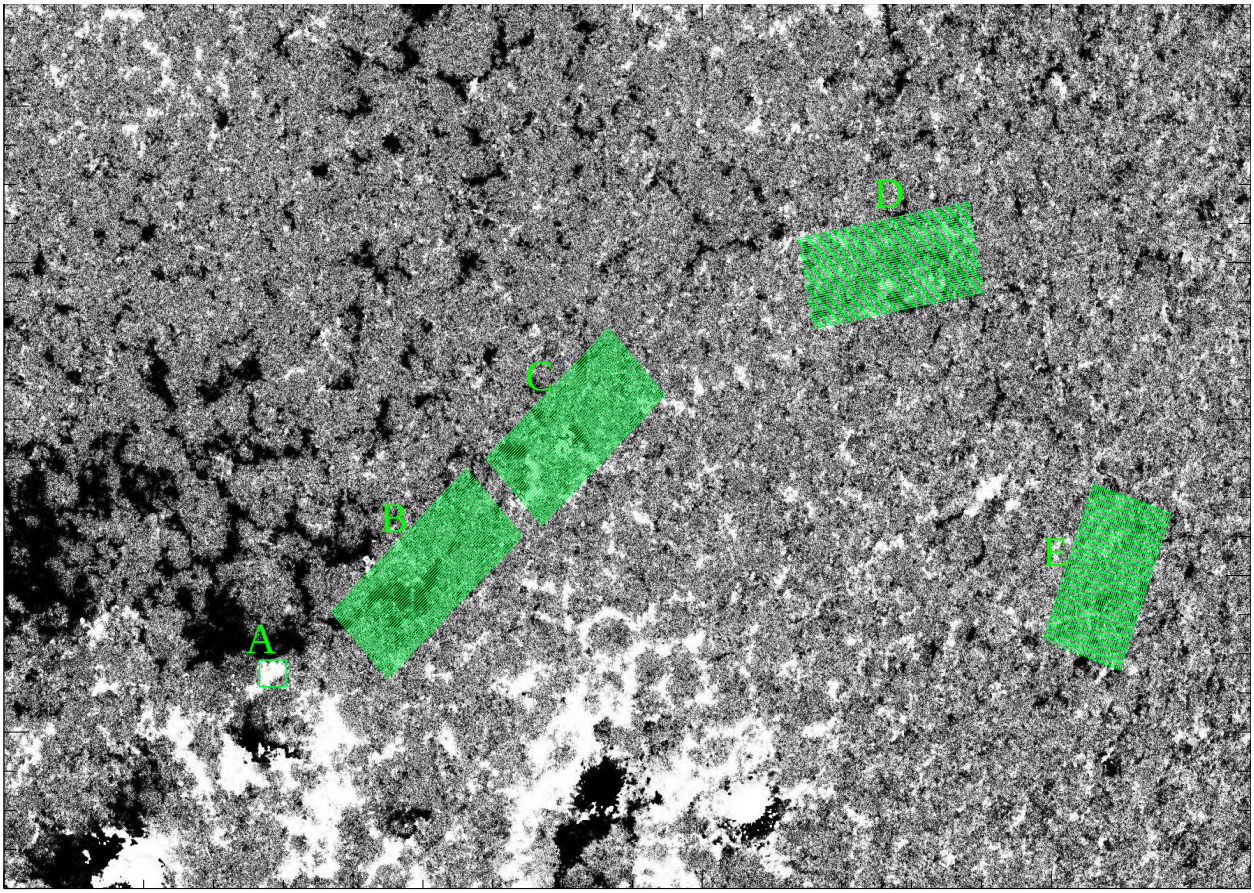

Figure 5.12: Image to represent the magnetic field, as seen from the Earth direction, at 08:20:15 on the second day of observation. Note the large white areas beneath the collection of lines denoted by C, where the magnetic field is strong and positive. The location of the filament channel can be deduced by observing the polarity inversion line, where the predominant color changes on the magnetogram, indicating a change in the direction of the magnetic field.

5.8.1 Speeds Observed at Location C

As with all other locations, there are fast bright features to be seen in the distance-time plots for location C. For example, speeds of 60km s^{-1} in the clockwise direction on line 8 and 155km s^{-1} in the anti-clockwise direction on line 19 in the 193Å wavelength between 15:00 and 15:20 on the first day of observation. Speeds such as 245km s^{-1} on line 9 were observed in the clockwise direction in the 211Å wavelength and 125km s^{-1} in the anti-clockwise direction on line 23 in the 304Å wavelength between 17:20 and 17:40 on the first day of observations. Speeds such as 110km s^{-1} on line 12 were observed in the clockwise direction and 80km s^{-1} in the anti-clockwise direction on line 27 in the 171Å wavelength between 08:20 and 08:40 on the second day of observations.

5.8.2 Fast Motions in Both Directions Apparently on the Same Line

At location C, it is clear that several lines appear to exhibit motions traveling in both directions along the same line, and these motions appear to be connected. Examples are to be seen in Figure 5.13.

Figure 5.13 shows fast motions which appear to be reflected when arriving at a location where the magnetic field is strong. Figure 5.13a shows motions which travel in the anti-clockwise direction with speed 120km s^{-1} and then in the clockwise direction with speed 240km s^{-1}. The results shown in Figure 5.13b are very similar, with speeds of 90km s^{-1} in the anticlockwise direction and then 250km s^{-1} in the clockwise direction. Therefore the speeds shown in the two plots are similar, and could be identical, however the location of the reflection is different. This could be explained by the fact that the two sets of observations are from different locations. All examples of such "reflection" occur at approximately 08:34.

The "reflected" feature, despite its increased speed, appears to have a lower intensity than the original feature. The average intensity for the original feature was 323.0 and the average intensity for the "reflected" feature was 252.2. The significance of this can be tested by use of the T-test (Loughborough, 2004), as shown below:

$$t = \frac{|\bar{x_1} - \bar{x_2}|}{S_p} \sqrt{\frac{n_1 \cdot n_2}{n_1 + n_2}}$$

Where t is the t-statistic (a measure of the departure from the mean relative to the standard deviation), $\bar{x_1}$ is the mean intensity for the original feature, $\bar{x_2}$ is the mean intensity for the "reflected" feature, n_1 is the number of data points in the dataset for the original feature, n_2 is the number of data points in the dataset for the "reflected" feature and S_p is the pooled standard deviation as described below:

$$S_p = \sqrt{\frac{(n_1 - 1) \cdot S_1^2 + (n_2 - 1) \cdot S_2^2}{n_1 + n_2 - 2}}$$

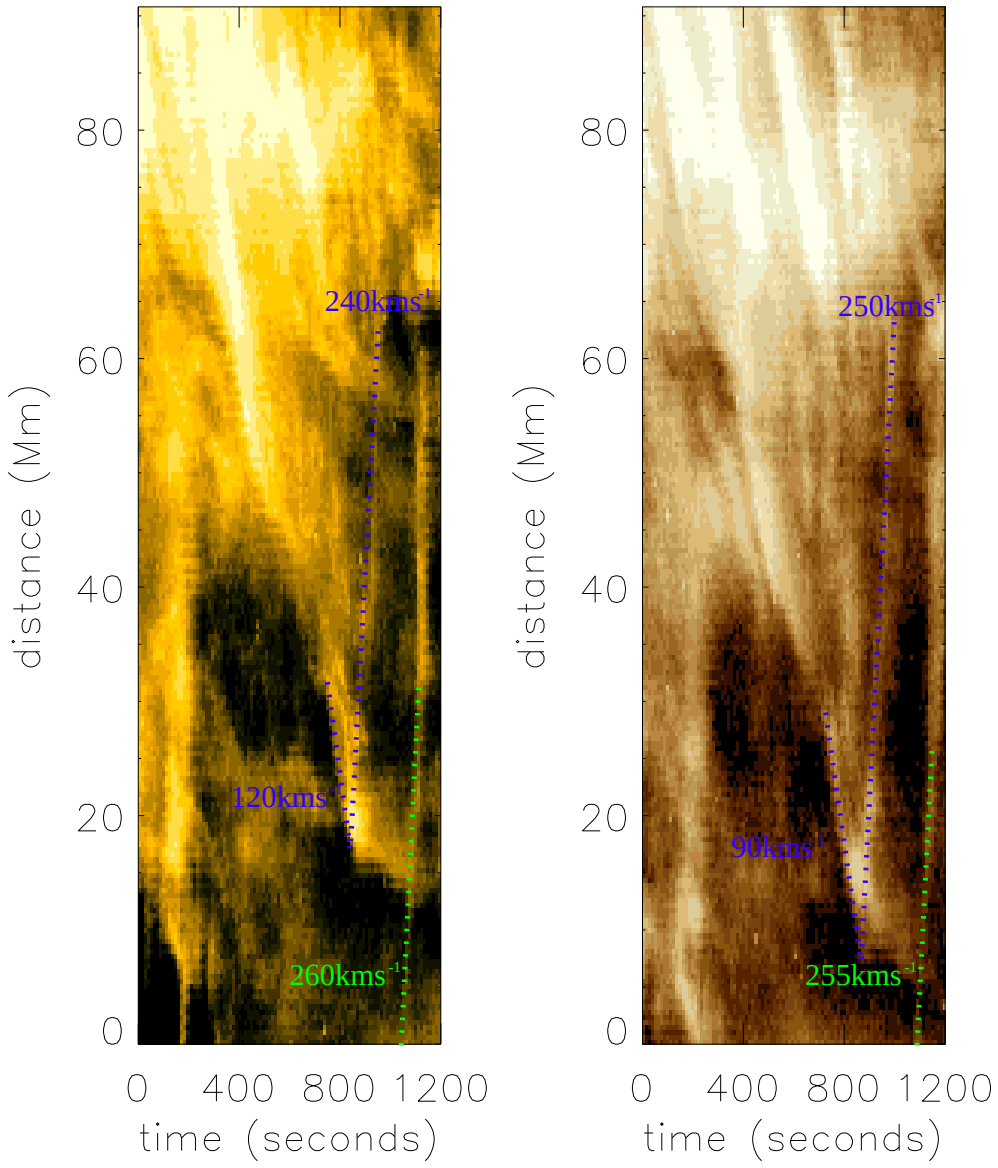

Figure 5.13: (a) line 22 in the 171Å wavelength between 17:20 and 17:40 on the first day of observations. Note the feature traveling in the anti-clockwise direction with a speed of approximately 120km s^{-1} which is subsequently "reflected" upon arriving at an area of strong magnetic flux, and then traveling in the clockwise direction with a speed of approximately 240km s^{-1}. Note also the presence of another feature (denoted by a green dotted line) with a speed of approximately 260km s^{-1}. This feature appears to accelerate but the speed thereafter is unclear (b) line 19 in the 193Å wavelength between 17:20 and 17:40 on the first day of observations. A feature travels anti-clockwise with speed 90km s^{-1} and is then 'reflected' to travel clockwise with speed 250km s^{-1}. Again, the green dotted line denotes another feature with a speed of approximately 255km s^{-1};its speed thereafter is unclear.

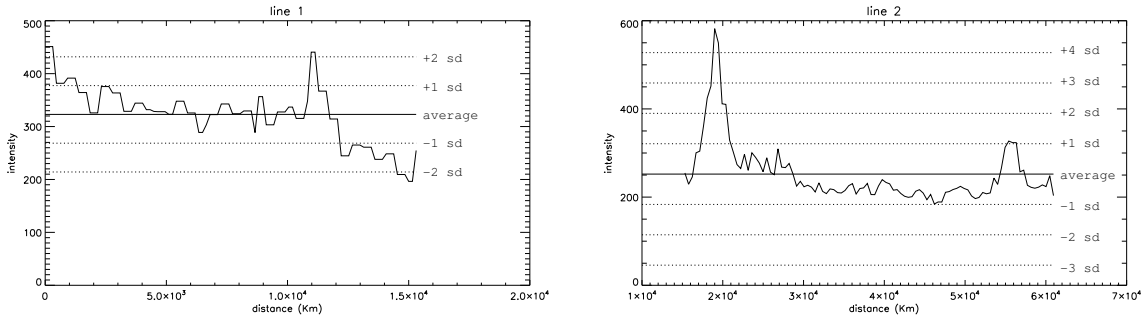

(a) original feature

(b) "reflected" feature

Figure 5.14: Variations in intensity in the 171Å wavelength (a) along the original feature referred to in section 5.8.1 (b) along the "reflected" feature referred to in section 5.8.1. The intensity is fairly consistent (in two distinct sections in (a)), but there are several outliers which may be responsible for the high standard deviation in the data set.

Where S_1 is the standard deviation for the dataset for the original feature and S_2 is the standard deviation for the dataset for the "reflected" feature.

In the 171Å wavelength, with the parameters $\bar{x_1} = 323.0$, $\bar{x_2} = 252.2$, $S_1 = 54.4$, $S_2 = 68.9$, $n_1 = n_2 = 100$, the T-value is 0.806. However, with $n_1 + n_2 - 2 = 198$ degrees of freedom, the T-value for 90% significance would be 1.286; hence the difference between the two averages is not significant to 90% accuracy.

However, figures 5.14a and 5.14b show that the intensities on both paths are constant, though in the original feature in perhaps two sections, but there are a number of outliers which are likely to have contributed to the large standard deviations obtained. In particular, the "reflected" feature contains a point which is 4.79 standard deviations greater than the average. This could be due to noise in an AIA image. When the datasets were refined to remove any values which deviated from the average by more than 2 standard deviations, the following values were obtained: for the original feature, the average intensity was 322.7 with a standard deviation of 40.4; for the "reflected" feature, the average intensity was 238.2 with a standard deviation of 37.9. The average intensities are still close to their original values, exceptionally so for the original feature, but the standard deviations are more sensible. When the T-test was performed again, this time with $n_1 = 90$ and $n_2 = 94$, a T-value of 1.48 was obtained. The 90% significance level, with 182 degrees of freedom, would be 1.286, whilst the 95% significance level would be 1.6526. Hence the difference between the intensities for the original feature and the "reflected" feature, in the 171Å wavelength, is significant to 90%, though not to 95%. Hence the intensity has decreased significantly.

The difference in intensity between the original feature and the "reflected" feature is less obvious in the 193Å wavelength, where $\bar{x_1} = 263.6$, $\bar{x_2} = 246.4$, $S_1 = 25.9$ and $S_2 = 70.1$. The T-value here is 0.230, which is clearly not significant at the 90% level. Applying the same procedure as performed for the 171Å data only

increases the T-value to 0.325, which is not significant at the 90% level.

Another interesting feature that appears on both plots is that seen towards the end of the time interval, with the appearance of a feature apparently originating outside the region. This feature had a speed of 260km s^{-1} in the 171Å wavelength and 255km s^{-1} in the 193Å wavelength, before accelerating to a faster speed which cannot be accurately determined in these instances. This speed appears to be the same as that observed for the "reflected" feature, in both the 171Å and 193Å wavelengths. In the 171Å wavelength, the feature from outside the region had an average intensity of 260.7, with a standard deviation of 45.2. When comparing the intensity of this feature with the "reflected" feature, a t-value of 0.38 was obtained, therefore the intensities of these 2 features are not significantly different; hence both the reflected feature and the feature from outside the region have very similar characteristics. In the 193Å wavelength however, the feature from outside the region has an average intensity of 178.8 and a standard deviation of 9.0. Comparing this with the intensity of the "reflected" feature yields a t-value of 0.96, with 194 degrees of freedom. The threshold for 90% significance would be 1.29. Hence there is no significant difference between the brightness of these two features.

Figure 5.15 provides a graphical representation of where there is and isn't a significant difference between the average intensities of the three features. The diamonds represent the average intensities and the error bars represent how much difference is required between the two for the difference to be significant at the 90% level (solid) and 95% level (dashed). If the diamond without error bars is higher or lower than a set of error bars then there is a significant difference. It is clear that only 1 pair of features in the 171Å wavelength, and in the 193Å wavelength, are significantly different. The original and reflected features in the 171Åwavelength are significantly different at the 90% level, but not at the 95% level. The original and outside features in the 193Å wavelength are also significantly different at the 90% level, but not at the 95% level. No other pairs are significantly different at the 90% level.

There are several possible interpretations of the "reflection" observed.

Firstly, perhaps the bright features analyzed are "jumping" from one flux rope to the other. But I feel this is an unlikely explanation because this phenomenon occurs in several adjacent flux ropes, in several wavelengths, at a similar distance along the line analyzed.

Secondly, the phenomenon can be interpreted as bright features traveling to an area of strong magnetic flux, and following this new bright features, originating elsewhere, are observed to travel in the other direction from the area of strong magnetic flux. This is supported by the presence of a bright feature traveling at a very similar speed to the "reflected" features but originating outside the area under study.

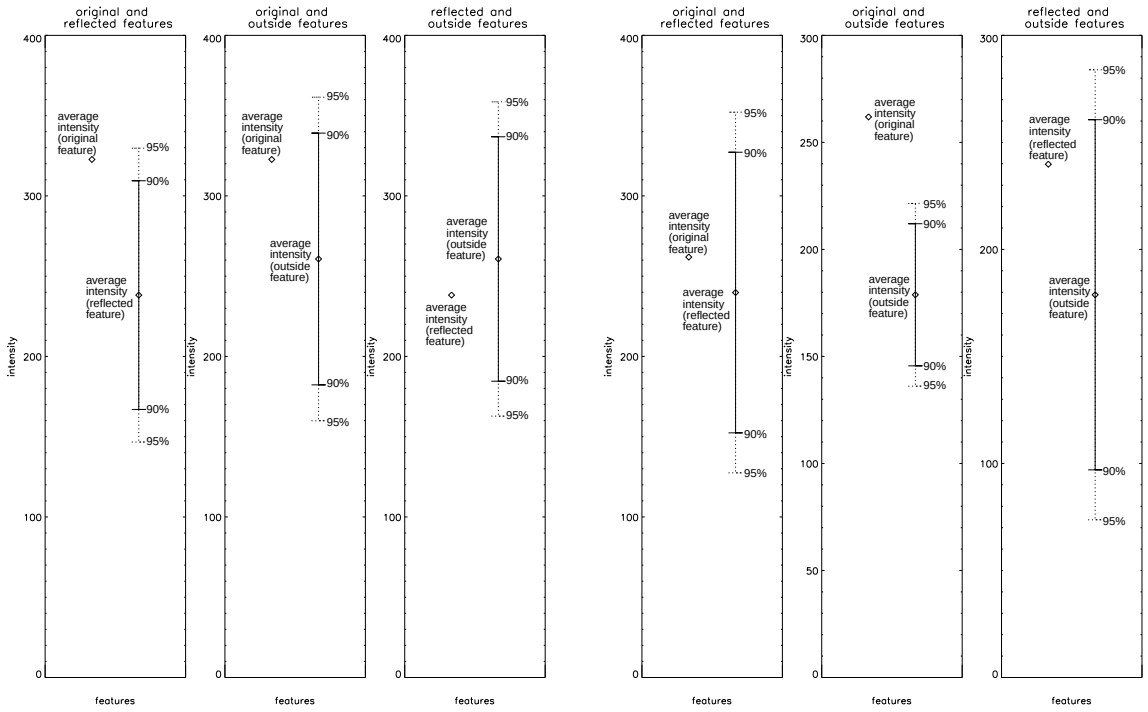

(a) 171Å

(b) 193Å

Figure 5.15: The solid bars denote the the difference in mean intensity values required for the difference to be significant at the 90% level, using the t-test. The dotted bars denote the difference in mean intensity values required for the difference to be significant at the 95% level. The diamonds represent the average intensity for each feature. If a diamond lies outside the error bars for 90%, there is a significant difference. It is clear that the only significant differences in intensity are between the original and reflected features in the 171Å wavelength and between the original and outside features in the 193Å wavelength.

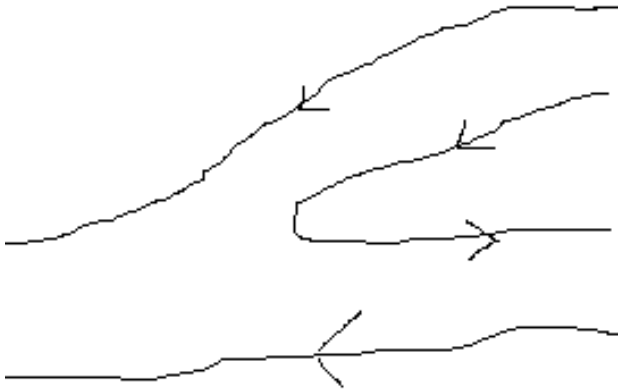

Figure 5.16: A diagram illustrating the possibility of a "u-turn" in a flux tube

Thirdly, it can be interpreted as the motions genuinely being reflected, as suggested by Ahn et al. (2010).

Fourthly, it is possible that the flux rope makes a "u-turn" and changes direction by roughly 180 degrees, viewed in two dimensions. This is explained further by the diagram in Figure 5.16. This would of course entail a change of height, relevant to our 2D view. A compelling observation which supports this view is that, in the 171Å observations for line 21 show that the "reflected" feature had significantly lower intensity than the original feature, and this could of course be due to material at high altitude obscuring our observations of the feature. This would imply that the "reflected" feature may be traveling at a lower altitude, relative to our 2D view, than the original feature, due to our view of it being blocked by overlying plasma, which would be very compatible with the "u-turn" explanation. It is prudent to note at this juncture that the cross-section of the filament appears to be reducing towards this point, approaching an area of strong magnetic field, suggesting either that the flux ropes are becoming closer together together or that some flux ropes are making a "u-turn" at this point (thus reducing the number of flux ropes following the filament channel near the area of strong magnetic field).

5.9 Motions in Both Directions Originating from an Area of Strong Magnetic Flux

Another phenomenon which perhaps sheds light on our understanding of counter-streaming motions is what is seen near an area of strong magnetic flux on the eastern side of the filament. This is denoted by A in Figure 5.7 It is evident from Animation 1 that fast motions are leaving this area and traveling along the filament (or at least along parts of it) in completely opposite directions. Figure 5.17 shows graphically how

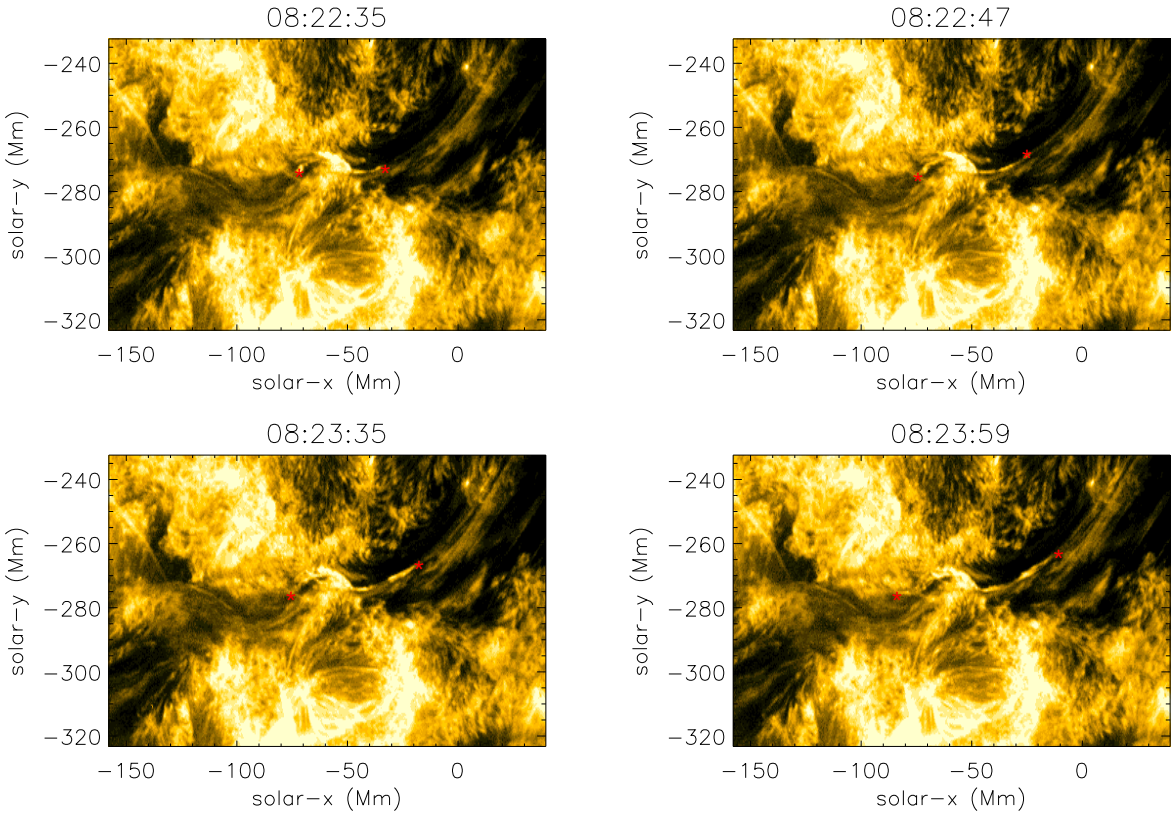

Figure 5.17: It is evident that bright motions are traveling along the filament in both directions, beginning at an area of strong magnetic flux. The green stars denote the extent of the motions at the times given above the images.

the two motions move over time, where the progress of the features are denoted by green stars.

It is clear from Figure 5.17 that bright motions in both directions originate in the area under study at about 08:22. This is a clear indication of the existence of counter-streaming motions in the filament, and suggests that an area of strong magnetic flux could be responsible for this type of phenomenon.

5.9.1 Changes in the Magnetic Flux in an Area of Strong Magnetic Flux

It is evident that the counter-streaming motions described in section 7 originate from an area of strong magnetic flux, over 700G in some places. The HMI observations show large white patches inside the area, which denote a strong, positive magnetic field. In the previous chapter, this area was discussed and significant decreases in the magnetic flux were found to be co-temporal with the production of wave trains. These also appear to be co-temporal with the some of the counter-streaming motions seen to be emanating from this area.

5.10 Discussion

Clearly, counter-streaming motions are widespread in this filament, both spatially and temporally. The natural conclusion to be drawn from this is that they are likely to be ubiquitous. Many of the observed counter-streaming motions are also faster than previously reported in several papers in the past. The motions are much faster than the results of H-α analysis, and this shows that analysis of AIA images aids and expands the study of counter-streaming motions.

It is felt that line-of-sight illusions could not be responsible for this phenomenon, since the observed speeds are so fast and so varied. Also, the filament was quite centrally located on the solar disc, which would reduce chances of line-of-sight illusions.

An interesting feature not yet mentioned is the trend for groups of motions to travel along the flux ropes in the same direction on roughly one half of the filament, and in the other direction on the other, at some times, as can be seen from figure 5.6 for instance. However, this was not always true and furthermore, the spatial pattern was reversed at various times, whilst the main structure of the filament remained largely constant. Hence the observations appear, to some extent, to contradict the conclusions by Gaizauskas (1998) that counter-streaming motions are a function of filament chirality.

The results seen at location C are especially interesting, since they show motions which appear to change

direction in the course of their journey. This leads to several explanations as detailed in section 5.8.2. Amongst these, there is the interpretation that the motions are reaching an area of strong magnetic flux and then another motion travels in the other direction, or that the motions experience reflection and change direction, as suggested by Ahn et al. (2010), or that the flux tubes perfom a "u-turn" upon reaching a point where the magnetic field is very strong. Of course, it is possible that all or any two explanations are true in different situations. Further, the fact that 2D observations are used to observe the counter-streaming motions suggests that the explanation by Ahn et al. (2010) could be a special case of the "u-turn" scenario. The unrelated motions traveling with a similar velocity would suggest that the motions in the clockwise direction after around 08:34 are a wider phenomenon, not exclusive to the areas of flux under location C, therefore the explanations for location C may well be true in general.

The explanations provided are in agreement with the findings by, for instance, Zirker et al. (1998), that counter-streaming follows magnetic field lines. Since the counter-streaming motions are along flux tubes, which are believed to outline the magnetic field, this is eminently plausible. Regarding the direction of the magnetic field and the counter-streaming motions observed, the "u-turn" explanation in particular does not require any of the motions to travel in the opposite direction to $\mathbf{B}$. Thus this explanation is very conducive to explaining the apparent observations in this work of motions being "reflected" along the same flux rope.

The observation of two motions in opposite directions that originated from an area of strong magnetic flux provides clear evidence that the magnetic field plays a role in causing counter-streaming motions. The significant decrease in magnetic flux in the area was co-temporal with the production of counter-streaming motions along the filament channel. It follows that strong magnetic fields in the filament channel can provoke counter-streaming flows. This is entirely plausible from a theoretical viewpoint, since a high magnetic field would engender a low plasma beta; this means that a small change in the magnetic field could produce a large change in plasma pressure, which could cause waves or flows along the filament channel.

The discussion about flows or waves is also very relevant to this part of the research. The reason for my almost ubiquitous use of the term "counter streaming motions" rather than the more widely used term "counter streaming flows" stems from the uncertainty over whether the observed bright features are in fact flows or waves. Many authors have discussed whether to classify motions in solar structures as flows or waves. McIntosh & De Pontieu (2009) observed bright blobs with speeds $100 - 140\text{km s}^{-1}$ and discussed whether these were flows or waves. They eventually interpreted these as upflows. Tian et al. (2011) also explained the movements of bright blobs in solar prominences as upflows, rather than waves, mostly due to the lack of evidence of oscillations in their observations of Doppler shifts. However, Mariska et al. (2008) found from HINODE observations that some features which appeared to be upflows were in fact waves, citing

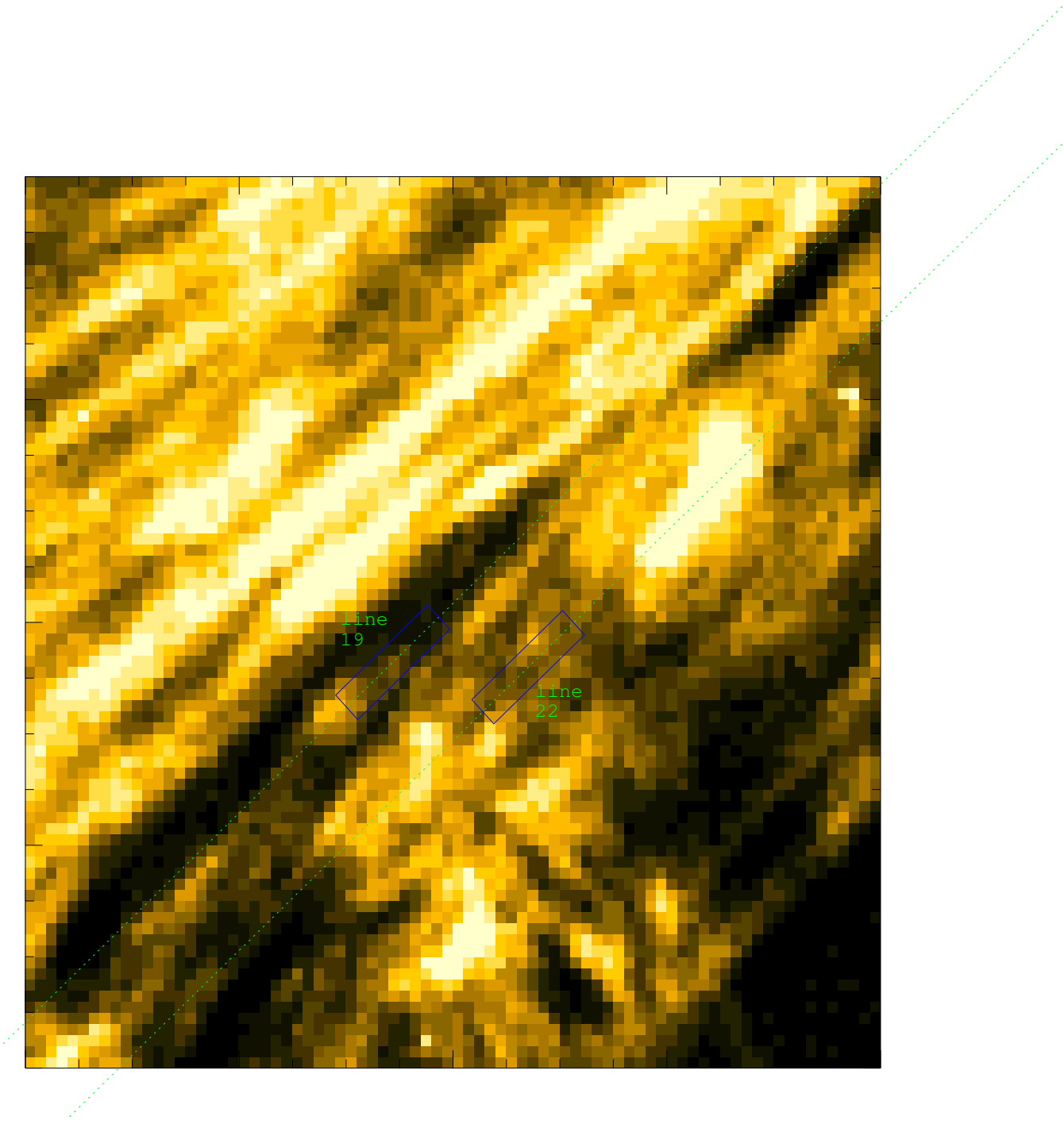

Figure 5.18: The areas considered in intensity comparisons. Lines 19 and 22 in location C are the labeled dotted lines and the area considered in the intensity comparisons on each is denoted by a blue box. Lines 19 and 22 correspond to the distance-time plots in figures 5.13b and 5.13a respectively.

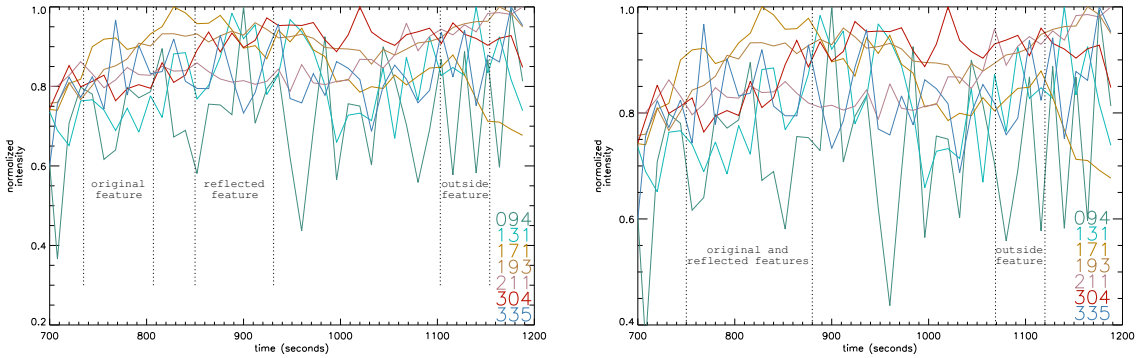

(a) Line 19

(b) Line 22

Figure 5.19: The normalized intensity in 7 AIA wavelengths over a period of 1200 seconds. (a) within the area demarcated in Figure 5.18, line 19. The datasets were normalized so that the maximum of each dataset was 1. The dotted lines denote the time boundaries of when the original, reflected and outside features referred to in Section 5.8.2 appear to pass through the area under study. (b) within the area demarcated in Figure 5.18, line 22. The time intervals for the original and reflected features are combined because there is not a clear boundary between the two on the distance-time plot in Figure 5.13a.

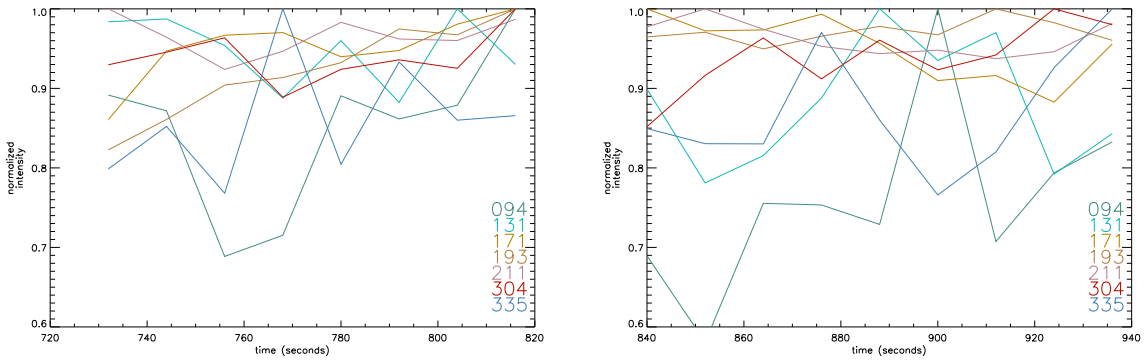

(a) Original Feature

(b) "Reflected" Feature

Figure 5.20: Intensity variations in 7 AIA wavelengths, 94Å, 131Å, 171Å, 193Å, 211Å, 304Å and 335Å along the features denoted in Figure 5.13b, line 19. The datasets have been normalized so that the maximum of each dataset is 1. (a) Intensity variation for the original feature (b) Intensity variation for the "reflected" feature. As can be seen, there is no evidence of co-temporal intensity peaking in all the wavelengths, rather they appear to peak at significantly different times.

the evidence of oscillations with period of approximately 10 minutes in the observed Doppler shifts in the solar corona. Following this, Wang et al. (2009) interpreted rising blobs in solar prominences as waves, on the basis of HINODE observations, and speculated that these may result from waves "leaking" through the chromosphere and into the corona. They also suggested that this may also happen in solar spicules.

Alexander et al. (2013) observed bright features which exhibited counter-streaming, which appeared similar to the features in this research, and concluded that these were mass flows. Their evidence involved a study of the changes in intensity over time of a small area where counter-streaming was observed in several AIA wavelengths and Hi-C; they then produced a graph of the intensity over time in these wavelengths, normalized in such a way that the maximum value for each wavelength was 1. They found that, in their case, the peaks in each wavelength (that is, when each wavelength appears brightest) appeared to be co-temporal, and argued that this led to the conclusion that the observed features were mass flows.

When this analysis was repeated on two areas in region C in my filament, the results were different. The areas studied are shown in Figure 5.18. Both areas took the form of a parallelogram 3 pixels wide. The first area was centered on line 19, and the second area was centered on line 22. The start and end points along each line were decided by the clarity of the features in the relevant distance-time plots.

The results on lines 19 and 22 are shown in figures 5.19a and 5.19b respectively. The different wavelengths are denoted by the widely used and recognized color for each wavelength, and these are shown to the right of the graphs. The vertical dotted lines signify when the various features began and ended their journey through the parallelogram under study. There is one exception to this: in Figure 5.19b there is no clear gap in time between the intensity associated with the original and reflected features. This was caused by the parallelogram being very close to the flux area where "reflection" occurred.

It is clear that there is little evidence of co-temporal peaking, as observed by Alexander et al. (2013). On the contrary, insofar as peaks are observed (and they are significantly less obvious than in Alexander et al, 2013), they appear to be staggered.

Taking two areas individually confirms this. Figure 5.20 shows the intensity variations in the line 19 parallelogram, for the original feature on the left and for the reflected feature on the right. Staggered peaking of the different wavelengths is clearly seen. This suggests that the conclusions of a mass flow in Alexander et al, 2013 are not relevant to the features studied in this work. The intensity variations do not lead to a conclusion of mass flows.

On the contrary, the presence of such numerous bright features and also the speeds observed, frequently in the order of 200-300km s^{-1}, suggest that a wave solution would be eminently compatible with the observations.

It would be difficult to conceive of such a large number of mass flows moving with such speed, however such speeds would not be unusual for sound-waves within flux tubes. Use of global temperature mapping on the area covered by the filament suggested an approximate temperature in the order of 1.5MK in some of the areas covered by the filament, meaning that a sound speed in the order of 300km s^{-1} would be plausible in at least some parts of the filament.

Although the possibility of some or all of the observed features being mass flows cannot be excluded, it appears entirely feasible that many of the observed features are sound-waves. The explanation of sound-waves provides amply for the different speeds observed, since the sound speeds in different flux tubes will necessarily vary according to the temperature and properties of the plasma in each flux tube. The explanation of waves also provides for the large number of features observed, since waves are more likely to be in abundance than mass flows.

Finally, longitudinal oscillations, with flows traveling back and forth in each flux rope, can be discounted as an explanation for the observed counter-streaming, since longitudinal oscillations have not been observed as being fast enough to account for many of the observed features, according to observations by other authors (Arregui et al. (2012), Jing et al. (2003), Jing et al. (2006), Vršnak et al. (2007)).

Given this, I would suggest that many of the observed features are likely to be waves rather than mass-flows. This has interesting implications for the study of filaments and solar structures, insofar as the observed features appear similar to features in other structures interpreted as flows by other authors in previous research. It would therefore be prudent to consider that such features could in fact be waves rather than mass flows when studying structures of this kind. I would further suggest that the "u-turn" scenario posed could be a new and interesting explanation for counter-streaming and is a likely explanation for at least some of the observed counter-streaming motions, although other explanations such as the Ahn reflection model and the idea of adjacent threads having a magnetic field running in opposite directions cannot be discounted and could feasibly be an explanation for some other observed counter-streaming motions.

Bibliography

Ahn, K., Chae, J., Cao, W., & Goode, P. R. 2010, The AstroPhysical Journal, 721, 74

Alexander, C. E., Walsh, R. W., Régnier, S., et al. 2013, The AstroPhysical Journal Letters, 775, L32

Arregui, I., Oliver, R., & Ballester, J. L. 2012, Living Reviews in Solar Physics, 9,

Bommier, V., Landi Degl'Innocenti, E., Leroy, J.-L., & Sahal-Brechot, S. 1994, Solar Physics, 154, 231

Chen, P. F., Innes, D. E., & Solanki, S. K. 2008, Astronomy & AstroPhysics, 484, 487

Deng, Y., Lin, Y., Schmieder, B., & Engvold, O. 2002, Solar Physics, 209, 153

Gaizauskas, V. 1998, IAU Colloq. 167: New Perspectives on Solar Prominences, 150, 257

Isobe, H., & Tripathi, D. 2006, Astronomy & AstroPhysics, 449, L17

Isobe, H., Tripathi, D., Asai, A., & Jain, R. 2007, Solar Physics, 246, 89

Jing, J., Lee, J., Spirock, T. J., et al. 2003, The AstroPhysical Journal Letters, 584, L103

Jing, J., Lee, J., Spirock, T. J., & Wang, H. 2006, Solar Physics, 236, 97

Knizhnik, K., Luna, M., Muglach, K., et al. 2014, Nature of Prominences and their Role in Space Weather, 300, 428

Lin, Y., Engvold, O., & Rouppe van der Voort, L. H. M. 2012, The AstroPhysical Journal, 747, 129

Lin, Y., Engvold, O. R., & Wiik, J. E. 2003, Solar Physics, 216, 109

Lin, Y., Martin, S. F., & Engvold, O. 2008, Subsurface and Atmospheric Influences on Solar Activity, 383, 235

Loughborough University 2004, <http://www.lboro.ac.uk/media/wwwlboroacuk/content/mlsc/downloads/1.2_Unpairedttest.pdf>, accessed March 2016

Mariska, J. T., Warren, H. P., Williams, D. R., & Watanabe, T. 2008, The AstroPhysical Journal Letters, 681, L41

McIntosh, S. W., & De Pontieu, B. 2009, The AstroPhysical Journal Letters, 706, L80

Okamoto, T. J., Tsuneta, S., Berger, T. E., et al. 2007, Science, 318, 1577

Panasenco, O., & Martin, S. F. 2008, Subsurface and Atmospheric Influences on Solar Activity, 383, 243

Schmieder, B., Bommier, V., Kitai, R., et al. 2008, Solar Physics, 247, 321

Schmieder, B., Roudier, T., Mein, N., et al. 2014, Astronomy & Astrophysics, 564, A104

Tian, H., McIntosh, S. W., & De Pontieu, B. 2011, The AstroPhysical Journall, 727, L37

Tripathi, D., Isobe, H., & Mason, H. E. 2006, Astronomy & AstroPhysics, 453, 1111

Vršnak, B., Veronig, A. M., Thalmann, J. K., & Žic, T. 2007, Astronomy & AstroPhysics, 471, 295

Wang, T. J., Ofman, L., & Davila, J. M. 2009, The AstroPhysical Journal, 696, 1448

Zirker, J. B., Engvold, O., & Martin, S. F. 1998, Nature, 396, 440

Chapter 6

Summary Conclusions and Future Possibilities

The work on modeling explored the possibility of modeling solar structures with 45 seconds temporal cadence. This would potentially be an improvement on current models which generally have a temporal cadence of 12 minutes. The potential for models which could observe the behavior of solar structures with such a superior temporal cadence could help our understanding of fast motions significantly. The other aspect was the potential to model solar structures as they would appear in a range of different AIA wavelengths. This would allow superior means of checking theoretical results against actual EUV data from the AIA apparatus, and would also have the advantage of showing the expected spatial distribution of plasmas of different temperatures, which would be particularly useful in the light of recent research highlighting the differential distribution of plasma temperatures in solar structures referred to in the Introduction chapter.

The original hope was to model filaments with 45 seconds temporal cadence; however the technique used was not suitable for filament channels and therefore the technique began by considering coronal loops. The results, whilst not as robust as some more established methods, allowed approximations of the free energy released in an eruption, three-dimensional modeling in different wavelengths, and also approximations of the temperature distribution of plasma within a system of coronal loops.

Although the research presented represents a significant advance in this type of modeling, a lot more development is required before the accuracy and self-consistency of the method comes close to other more established techniques. Future development would therefore require to consider a more complex view of the

observed magnetic field, whilst still applying the useful results of the NLFFF modeling. Another possible way forward for 45 second cadence modeling could involve feeding 3D magnetogram data into this type of modeling. One potential method could involve using 2D data (45 second cadence) as one input into a series of magnetograms, and approximating the two remaining co-ordinates (12 second cadence) every 45 seconds by interpolation; however this could be problematic in the case of sudden events, which are precisely what a 45s model tries to predict.

However, the model developed is a radical step forward in the active and popular field of NLFFF modeling.

Moving to the two observational chapters, the more immediate conclusions of this work involve the observation, analysis and classification of waves and possible explanations for their characteristics and behavior.

The observations of wave trains in a solar filament are, to my knowledge, the first of their kind. It appears that two fast waves with speed of close to 2000km s^{-1} propagate across a series of flux tubes in the filament channel, causing a series of magneto-acoustic waves. These magneto-acoustic waves have similar but differing speeds and properties, probably as a result of the different characteristics of the plasma in the different flux tubes. The wave interpretation of the motions is a result of observed acceleration and de-acceleration of a key feature, where the speed doubled within a short time and then decelerated again.

I suggest that there are two such systems of wave trains, each with one fast wave sparking a different series of magneto-acoustic waves. I also suggest that the wave trains are probably caused by changes in the magnetic flux in the area whence they were seen to originate. A significant decrease in magnetic flux was co-temporal with the production of the very fast waves. Hence this research, as well as discovering a new feature in the dynamics of solar filaments, also suggests that interaction with the magnetic field is very important in this phenomenon and is perhaps the cause of it. It also adds to the conclusions of the counter-streaming chapter that many of the bright fast features commonly observed in solar filaments may well be caused by interaction between the filament plasma and the magnetic field.

I have shown that counter-streaming motions with speeds in the order of 100s of km s^{-1} are common in the filament studied, using EUV data from the SDO, which some previous authors had claimed was not possible. I have classified these as waves rather than flows, thus contributing to the waves vs flows controversy, and suggest that it is possible that some features which may at first glance appear to be flows are in fact waves. This should inform further observational studies of counter-streaming and other motions in solar filaments, particularly in EUV wavelengths.

The counter-streaming work also contributes to the debate on the probable causes of counter-streaming in solar filaments. The fact that an area of strong magnetic flux was seen to cause the propagation of waves

in both directions along a filament channel suggests that counter-streaming motions could be caused by interaction with areas of strong magnetic flux in the filament channel. Furthermore, this is supported by the observations of waves being "reflected" upon their arrival at such an area in several threads simultaneously. Of the several explanations provided for this I would see my idea of flux tubes making a "u-turn" and returning in the opposite 2D direction but at a different altitude as a likely and ground-breaking explanation for at least some counter-streaming. I would further suggest that at least some counter-streaming waves are caused by interaction with regions of strong magnetic flux.

Future work on these topics to confirm the relationship between counter-streaming and magnetic activity in the filament channel, or to observe further wave trains of this sort, could involve a large number of observations of the sort presented in this research. However, filaments of this size with widely dispersed flux ropes, such that detailed AIA observations are possible with present instruments, are unfortunately very rare. Hence such studies would necessarily require both a significant amount of work and a significant amount of luck. Alternatively, it may be possible to use flux tube modeling to prove theoretically the possibility of flux release from areas in the channel causing counter-streaming and/or wave trains, though proving that this is a possible mechanism would still not necessarily prove that it is actually the cause of such occurrences in filaments. Despite this, it remains a valuable contribution to discussions of the nature and causes of counter-streaming waves and wave trains, and of filament dynamics in general.